

U. S. A R M Y
TRANSPORTATION RESEARCH COMMAND
FORT EUSTIS, VIRGINIA

AD 608514

TRECOM TECHNICAL REPORT 64-25

**A STUDY OF THE RADIATIVE
CHARACTERISTICS OF SHIELDED
INFRARED SOURCES**

| | | | | |
|------------|---|----|-----|------|
| COPY | 2 | OF | 3 | type |
| HARD COPY | | | \$. | 3.00 |
| MICROFICHE | | | \$. | 0.75 |

Task 1D121401A14802
Contract DA 44-177-TC-805

May 1964

prepared by:

HAYES INTERNATIONAL CORPORATION
Birmingham, Alabama



ARCHIVE COPY

DISCLAIMER NOTICE

When Government drawings, specifications, or other data are used for any purpose other than in connection with a definitely related Government procurement operation, the United States Government thereby incurs no responsibility nor any obligation whatsoever; and the fact that the Government may have formulated, furnished, or in any way supplied the said drawings, specifications, or other data is not to be regarded by implication or otherwise as in any manner licensing the holder or any other person or corporation, or conveying any rights or permission, to manufacture, use, or sell any patented invention that may in any way be related thereto.

* * *

DDC AVAILABILITY NOTICE

Qualified requesters may obtain copies of this report from

Defense Documentation Center
Cameron Station
Alexandria, Virginia 22314

* * *

This report has been released to the Office of Technical Services, U. S. Department of Commerce, Washington 25, D. C. , for sale to the general public.

* * *

The findings and recommendations contained in this report are those of the contractor and do not necessarily reflect the views of the U. S. Army Mobility Command, the U. S. Army Materiel Command, or the Department of the Army.

HEADQUARTERS
U S ARMY TRANSPORTATION RESEARCH COMMAND
FORT EUSTIS, VIRGINIA 23604


This report has been prepared by the Hayes International Corporation under the terms of Contract DA 44-177-TC-805. Views expressed in this report have not been reviewed or approved by the Department of the Army.

The technical objectives of this contract called for derivation of a theoretical or an empirical analysis which may be used to predict the infrared radiant intensity as a function of azimuthal angle for representative complex radiation sources.

The results of the investigation clearly indicate the feasibility of predicting the radiative characteristics of shielded infrared sources whose geometries can be described by analytical equations; the conclusions resulting from this feasibility study are concurred in by this command.

The information in this report will be utilized in future aircraft design to reduce radiation and thus to improve the passive defense characteristics of aircraft.


JERRY L. REED
Project Engineer


E. V. MERRITT,
Acting Chief
Human Factors & Survivability Group

APPROVED.

FOR THE COMMANDER:


LARRY M. HEWIN
Technical Director

Contract DA 44-177-TC-805
Task 1D121401A14802
TRECOM Technical Report 64-25
May 1964

A STUDY OF THE RADIATIVE
CHARACTERISTICS OF SHIELDED
INFRARED SOURCES

Final Report
Engineering Report Number 649

Prepared by
Hayes International Corporation
Birmingham, Alabama

for

U. S. ARMY TRANSPORTATION RESEARCH COMMAND
FORT EUSTIS, VIRGINIA

Part I

by

Ned D. Gilliam

Part II

by

James L. Reid

PREFACE

The final portion of this investigation was performed under Army Contract DA 44-177-TC-805 by Hayes International Corporation, Birmingham, Alabama, between June 1963 and January 1964. The work concludes the project reported in the interim report, TRECOM Technical Report 63-45, dated October 1963.

The authors wish to express their appreciation to Major Robert K. Floyd and the computer staff of Eglin Air Force Base, Florida, for their cooperation in making available their IBM 7094, and to Mr. Wyndol S. Hamer and the computer staff of Hayes International Corporation for their assistance in preparing and processing the runs on the IBM 1620.

CONTENTS

| | <u>Page</u> |
|--|-------------|
| PREFACE | iii |
| LIST OF ILLUSTRATIONS | vi |
| LIST OF SYMBOLS | ix |
| PART I. COMPOSITE COMPUTER PROGRAMS FOR EMPIRICAL EVALUATION OF INFRARED SHIELD CONFIGURATIONS | 1 |
| SUMMARY. | 1 |
| CONCLUSIONS. | 2 |
| INTRODUCTION | 3 |
| EMPIRICAL, RAY-TRACING PROGRAMS | 4 |
| EVALUATION | 37 |
| PART II. ANALYTICAL FORMULATION FOR EVALUATING INFRARED SHIELD CONFIGURATIONS. | 39 |
| SUMMARY. | 39 |
| INTRODUCTION | 40 |
| THEORETICAL BASIS. | 42 |
| COMPARISON OF DIRECTIONAL INTENSITIES. | 61 |
| BIBLIOGRAPHY. | 73 |
| APPENDIX A. OBSCURATION WITHIN A CONICAL SHIELD WITH SPHERICAL INNERBODY | 75 |
| APPENDIX B. KERNELS FOR CONICAL SHIELD CONFIGURATIONS WITH SPHERICAL INNERBODY | 82 |
| APPENDIX C. APPROXIMATE ANALYTIC FORMULATION FOR DIRECTIONAL RADIANT INTENSITY OF A DIFFUSE CYLINDER | 88 |
| DISTRIBUTION | 93 |

ILLUSTRATIONS

| <u>Figure</u> | | <u>Page</u> |
|---------------|---|-------------|
| 1 | Comparison of Attenuation Functions | 5 |
| 2 | Flow Diagram: Cylindrical and Conical Models. | 7 |
| 3 | Flow Diagram: Double Cone Models. | 8 |
| 4 | Gold Cylinder without Innerbody | 16 |
| 5 | Black Cylinder without Innerbody | 16 |
| 6 | Gold Cylinder with Gold Innerbody | 17 |
| 7 | Gold Large Cone without Innerbody | 17 |
| 8 | Black Large Cone without Innerbody | 18 |
| 9 | Gold Large Cone with Gold Innerbody | 18 |
| 10 | Gold Small Cone without Innerbody | 19 |
| 11 | Gold Small Cone with Gold Innerbody | 19 |
| 12 | Gold Double Cone without Innerbody. | 20 |
| 13 | Gold Double Cone with Gold Innerbody. | 20 |
| 14 | Gold Cylinder with Gold Innerbody | 27 |
| 15 | Gold Large Cone without Innerbody | 27 |
| 16 | Black Large Cone without Innerbody | 28 |
| 17 | Gold Large Cone with Gold Innerbody | 28 |
| 18 | Gold Small Cone with Gold Innerbody | 29 |
| 19 | Gold Double Cone without Innerbody. | 29 |
| 20 | Gold Double Cone with Gold Innerbody | 30 |
| 21 | Revised Attenuation Function | 30 |
| 22 | Gold Large Cone without Innerbody | 31 |

ILLUSTRATIONS (CONT'D.)

| <u>Figure</u> | | <u>Page</u> |
|---------------|---|-------------|
| 23 | Gold Large Cone with Innerbody | 31 |
| 24 | Double Cone with Innerbody, Curve A | 35 |
| 25a | Double Cone with Innerbody, Curves B and C | 35 |
| 25b | Double Cone with Innerbody, Curve D | 36 |
| 26 | Arbitrary Radiating Enclosure | 42 |
| 27 | Arbitrary Plane Elements | 49 |
| 28 | Interior Surface Elements of Conical Enclosure with Spherical Innerbody. | 57 |
| 29 | Geometry of Specular Cylinder. | 59 |
| 30 | Directional Intensity of Diffuse Cylinders | 62 |
| 31 | Directional Intensity of Diffuse Cylinders | 62 |
| 32 | Directional Intensity of Diffuse Cylinders | 63 |
| 33 | Directional Intensity of Diffuse Small Cones. | 63 |
| 34 | Directional Intensity of Diffuse Small Cones. | 65 |
| 35 | Directional Intensity of Diffuse Small Cones. | 65 |
| 36 | Directional Intensity of Diffuse Large Cones. | 67 |
| 37 | Directional Intensity of Diffuse Large Cones. | 67 |
| 38 | Directional Intensity of Diffuse Large Cones. | 68 |
| 39 | Directional Intensity of Diffuse Large Cones. | 68 |

ILLUSTRATIONS (CONT'D.)

| <u>Figure</u> | | <u>Page</u> |
|---------------|---|-------------|
| 40 | Directional Intensity of Diffuse Large Cones | 69 |
| 41 | Directional Intensity of Diffuse Cylinder with Innerbody | 69 |
| 42 | Directional Intensity of Diffuse Double Cone | 71 |
| 43 | Comparison of Approximate Analytic and Numerical Prediction for Diffuse Cylinder | 71 |
| 44 | Conical Shield with Spherical Innerbody | 76 |
| 45 | Obscuration of Conical Ring | 77 |
| 46 | Obscuration of Spherical Innerbody | 79 |
| 47 | Geometry of Double Cone | 85 |
| 48 | Projection Plane Coordinates | 88 |

SYMBOLS

| | |
|----------|--|
| α | Half-cone angle, cylindrical or conical models |
| ALFA 1 | Half-cone angle for Cone 1 of double cone model |
| ALFA 2 | Half-cone angle for Cone 2 of double cone model |
| CB | Distance along axis of model from base plane to center of innerbody |
| CLEN | Length of cylinder or cone |
| CONE 1 | That portion of the double cone model between the base plane and the midplane |
| CONE 2 | That portion of the double cone model between the midplane and the exit aperture |
| m | Direction cosine of ray relative to axis of model |
| RB | Radius of innerbody |
| RC | Radius of cylinder or cone at the exit aperture |
| REFB | Reflectivity of innerbody |
| REFC 1 | Reflectivity of Cone 1 of double cone model |
| REFC 2 | Reflectivity of Cone 2 of double cone model |
| RIO | Initial normal radiant intensity at base plane |
| PM | Radius of double cone model at the midplane |
| RP | Radius of cylinder or cone at the base plane |
| z | Distance along axis of model |
| z_m | Distance along axis of model to midplane |

PART I

COMPOSITE COMPUTER PROGRAMS FOR EMPIRICAL EVALUATION OF INFRARED SHIELD CONFIGURATIONS

SUMMARY

Two ray-tracing programs for digital computers have been written to predict the angular distribution of radiant intensity from an infrared source when shielded by a variety of cold shields. The laboratory measurements and initial prediction efforts were reported in full in the interim report, dated October 1963, of this contract.

Studies were conducted on two computers, an IBM 1620 and an IBM 7094. The results of 16 runs on the 1620 and 7 runs on the 7094 are presented in tabular and graphical form and are compared with the laboratory measurements, with the exception of the last four experimental runs, which did not have laboratory counterparts. These studies pointed out the power of this technique as a design tool and indicated the areas that still need concentrated work.

CONCLUSIONS

The present programs did not solve all the problems associated with the ray-tracing technique of determining angular radiation distribution patterns; but improvements were made, experience was gained, and the areas needing further development were more clearly delineated. The power of the technique as a design tool was demonstrated in part in the last four runs.

Further study is needed to develop a suitable correlation factor for relating the simple techniques of ray tracing to the more complex physical processes of emission and reflection. This need is more prominent at large angles.

A new area of needed study was revealed, namely, the detailed dependence of reflection on surface characteristics and how partially diffuse reflections can be handled most efficiently in a ray-tracing program. This study may require laboratory investigations to establish standards for the empirical or theoretical treatment.

INTRODUCTION

This is the final report on a study of the measurement and prediction of infrared radiation patterns from shielded infrared sources, conducted by Hayes International Corporation. The laboratory measurements program and the initial efforts at pattern prediction by a digital computer are comprehensively discussed in the interim report* and will not be repeated in this report. Reference should be made to the interim report.

That portion of the whole program which is covered by this report arose from certain conclusions drawn in the interim report. At that time, computer programs had been written which would predict radiation patterns for a particular set of shields of simple geometry. The degree of agreement with laboratory data was encouraging, but sufficient discrepancies existed for some of the configurations to justify (1) further investigation along the line of empirical, ray-tracing computer programs, and (2) development of an analytical formulation using integral equations. Accordingly, this report will be divided into two parts, the first dealing with the ray-tracing program and the second with the integral equation formulation.

* "A Study of the Radiative Characteristics of Shielded Infrared Sources", TRECOM TR 63-45, prepared by Hayes International Corp. for the U. S. Army Transportation Research Command, Fort Eustis, Virginia, October 1963.

EMPIRICAL, RAY-TRACING PROGRAMS

PROGRAM LOGIC

The original ray-tracing programs, discussed in the interim report, provided for ray selection in the aperture of the model and geometrical tracing back to the source plate. All rays were selected so as to lie in horizontal planes. When the new computer programs were written, this original approach was altered so that the program would more closely parallel the physical processes.

The origins of all rays were selected at random points in the plane of the model base, corresponding to the source plate of the laboratory apparatus. To each ray there was imparted a random direction. The distribution of random directions was weighted to produce a cosine distribution about the axis of the model. The rays were not restricted to horizontal planes. As before, all reflections were treated as specular. Generally, a ray was traced until it was reflected back to the base or out through the aperture. When a ray passed through the aperture plane, it was circularly projected onto the horizontal plane by converting the direction cosine relative to the axis into an angle relative to the axis.

Laboratory measurements had indicated that the radiating source plate approximated a Lambert surface within an average 6.2% when sampled at 10° intervals from 0° to 60° and at 65° . Inspection showed that the surface emission could be better approximated by a quartic expression than by the Lambertian cosine function. An expression of the form $a\theta^4 + b\theta^2 + c$, where θ is the angle between the ray and the axis, was solved for suitable values of the constants, a , b , and c . A plot of the attenuating function,

$$f(\theta) = .0701\theta^4 - .5786\theta^2 + 1, \quad (1)$$

compared with the laboratory measurements and the cosine curve is shown in Figure 1. The radiant intensity of each ray was attenuated at the base plane by this expression according to its angle of emission.

Eight different model configurations were studied; namely, a cylinder, a cylinder with a spherical innerbody, a truncated cone with the aperture at the larger end (referred to as the large cone), the large cone with a spherical innerbody, a truncated cone with the aperture at the smaller end (referred to as the small cone), the small cone with a spherical innerbody, a model composed of two opposed truncated cones having their large diameters in common (referred to as the double cone), and the double cone with a spherical innerbody. Two programs were written: one for the cylindrical

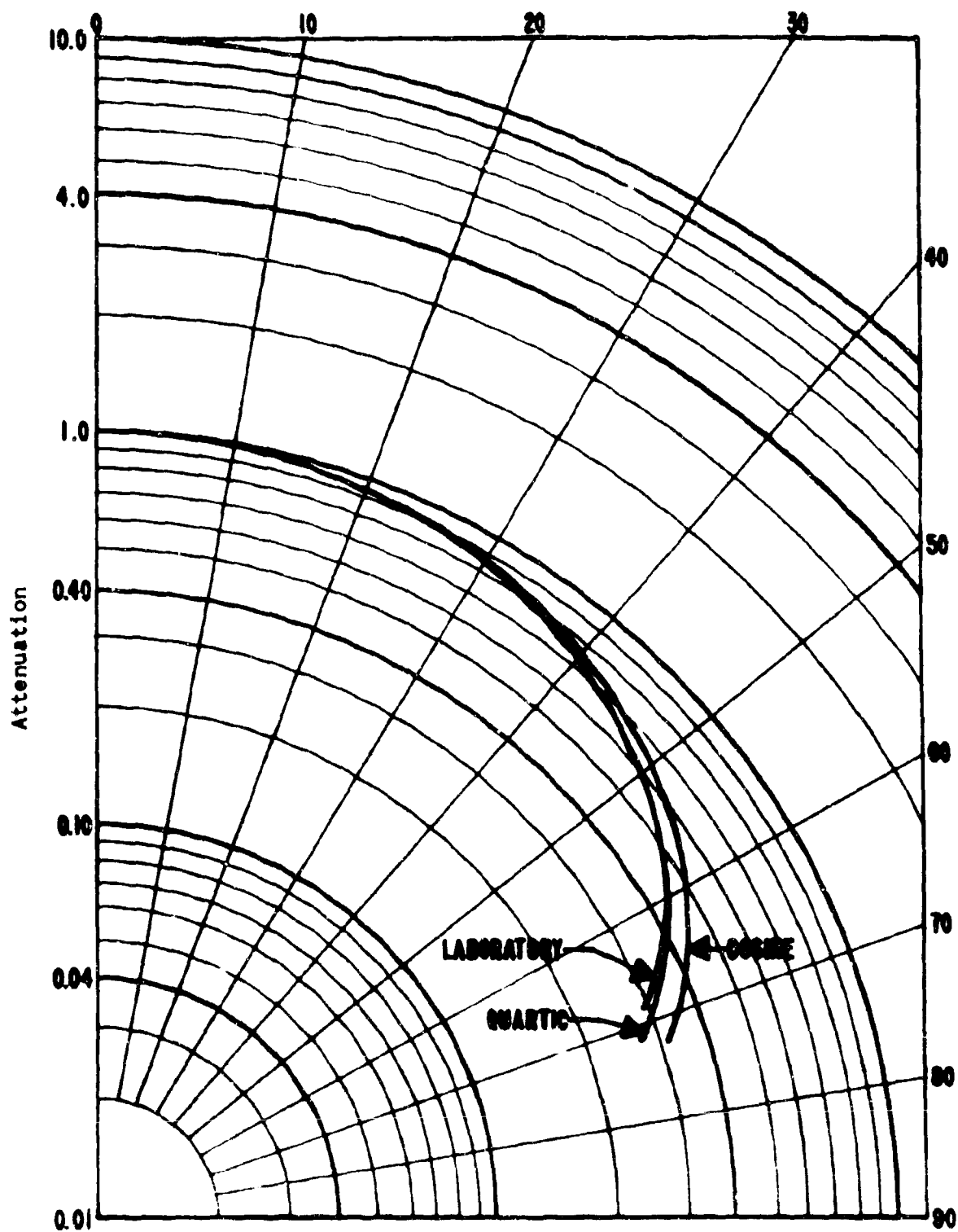


Figure 1. Comparison of Attenuation Functions.

and simple conical models with and without innerbodies, and one for the double cone with and without innerbody. Both programs were written with provisions for changing the dimensions, angles, innerbody size and position, and reflectivities of the various surfaces so that a variety of configurations could be examined. Block flow diagrams of the two programs are shown in Figures 2 and 3.

The combined model program, written for the cylinder and cones, starts at the double-boxed rectangle in the upper left corner. A random point is located in the base plane and a random direction is imparted to an emitted ray. The normal radiant intensity is attenuated according to the angle of emission. For the case of the cylinder, path control digits L_1 and L_2 are set to unity. If the ray intersects the innerbody (ball), the direction cosines of the reflected ray are determined, and the radiant intensity is attenuated according to the reflectivity of the surface. If the direction cosine relative to the axis (m) is negative and the model is the cylinder or small cone, a new direction at the base plane is assigned and the process repeated. If m is positive and the ray does not pass through the exit aperture, it must intersect the model. In the case of the cylinder, a test is made to determine how fast the ray is progressing down the model. This test is made only after the second intersection with the cylinder. If the model is the cylinder or if the m -direction cosine is positive, a test for intersection with the innerbody is made. If the ray does not intersect the innerbody but does pass through the aperture, the emergent ray is sorted into one of 19 directions according to its angle of emergence. When a predetermined number of rays have been traced, the accumulated data is output. A sample output data sheet is shown in Table 1. PHI is the angle of emergence. Rays emerging at a nominal angle $\pm 2.5^\circ$ are listed under the nominal angle. For example, a ray emerging at 26.7° would be included in the rays at 25° , while a ray at 27.7° would be included in the rays at 30° . The rays at 0° and 90° have only a 2.5° spread instead of the usual 5° . ARI stands for average radiant intensity and is determined by dividing TRI (total radiant intensity) by NO. RAYS. The line at the bottom of the print-out gives the specifications for the particular configuration being run. The abbreviation RIO stands for the initial radiant intensity (at the base plane); RB, for radius of innerbody (ball); RC, for radius of cone or cylinder at the aperture; RP, for radius of cone or cylinder at the source plate; CB, for distance along z-axis from the origin to the center of the innerbody; CLEN, for length of cone or cylinder; REFB, for reflectivity of cone or cylinder; RAYS, for total number of rays traced through the aperture; and ALFA, for the half-cone angle in radians.

The double cone program is quite similar to the combined model program, except tests must also be made for intersection with the midplane (the apex of the double cone), located at a distance z_m along the axis of the model from the base plane. Cone 1 is the portion of the model between the source and the midplane, and Cone 2 is the portion between the midplane and the exit aperture.

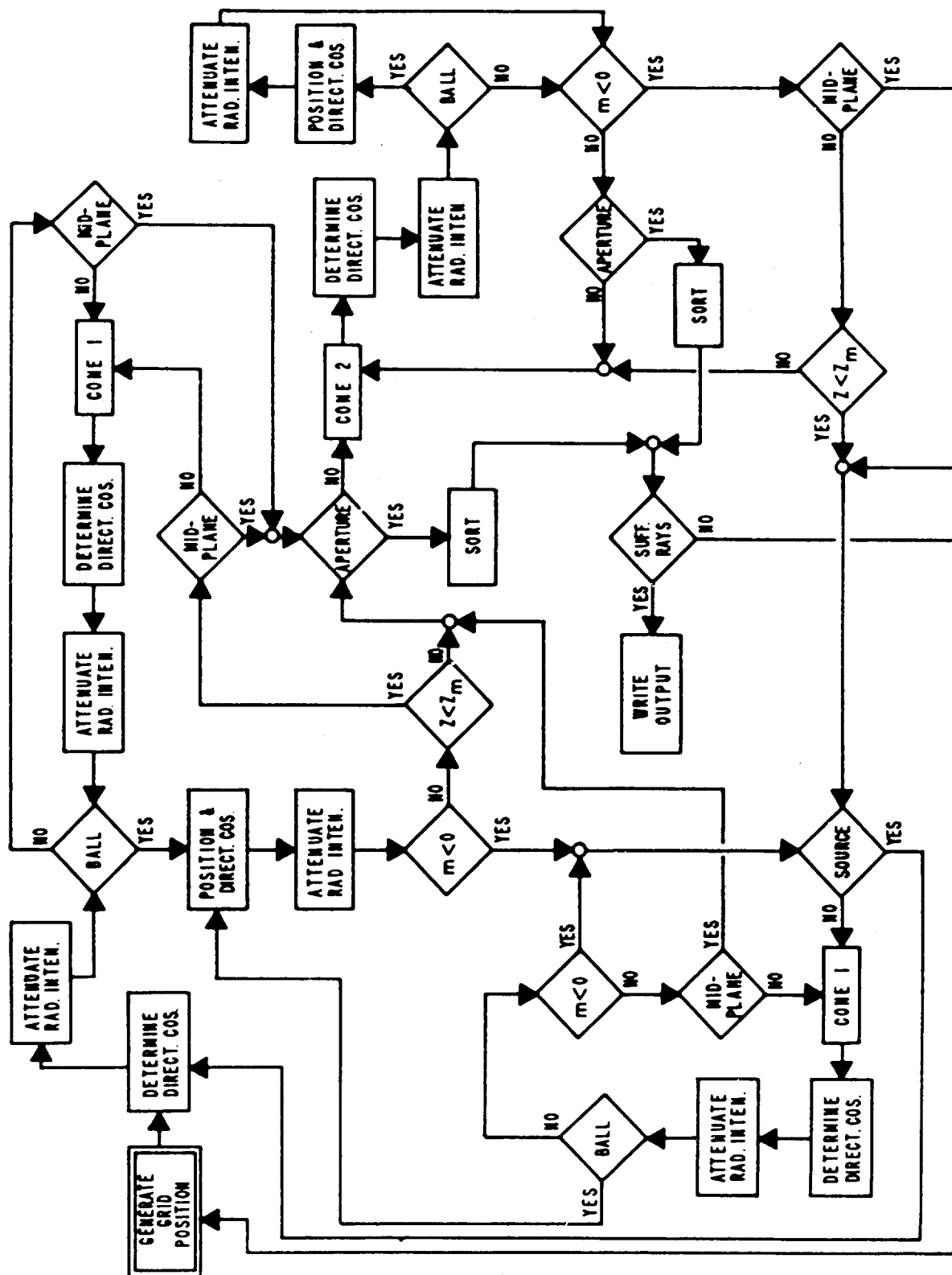


Figure 3. Flow Diagram: Double Cone Models.

TABLE 1

SAMPLE DATA PAGE

| Radiation Distribution Program - Cy. nder | | | | | | | |
|---|-------------|--------|-------------|--------|-------------|-------|-------|
| PHI (DEG) | ARI | | NO. OF RAYS | | TRI | | |
| 0 | .381630E+02 | | 220 | | .839587E+04 | | |
| 5 | .345476E+02 | | 734 | | .253579E+05 | | |
| 10 | .320656E+02 | | 1084 | | .347491E+05 | | |
| 15 | .311343E+02 | | 1058 | | .329400E+05 | | |
| 20 | .296948E+02 | | 1247 | | .370295E+05 | | |
| 25 | .260420E+02 | | 873 | | .227346E+05 | | |
| 30 | .235387E+02 | | 1084 | | .255160E+05 | | |
| 35 | .223240E+02 | | 817 | | .182387E+05 | | |
| 40 | .202803E+02 | | 677 | | .137297E+05 | | |
| 45 | .203205E+02 | | 763 | | .155045E+05 | | |
| 50 | .153449E+02 | | 324 | | .497174E+04 | | |
| 55 | .132982E+02 | | 547 | | .727412E+04 | | |
| 60 | .106233E+02 | | 273 | | .290017E+04 | | |
| 65 | .732909E+01 | | 136 | | .996757E+03 | | |
| 70 | .456081E+01 | | 136 | | .612055E+03 | | |
| 75 | .134207E+01 | | 27 | | .362360E+02 | | |
| 80 | - | | 0 | | - | | |
| 85 | - | | 0 | | - | | |
| 90 | - | | 0 | | - | | |
| RIO | RB | RC | RP | CB | CLEN | REFB | REFC |
| .381819E-02 | 1.500 | 2.000 | 2.000 | 6.3125 | 7.8125 | 0.900 | 0.900 |
| RAYS | | ALFA | | | | | |
| 10000 | | 0.0000 | | | | | |

RESULTS

The two programs were originally written for and were debugged on Hayes' IBM 1620 digital computer. Through the end of November 1963, all production runs were also run on the 1620. By that time, the difficulty of correlating some of the computer predictions with the laboratory data suggested the need for a faster computer in order to trace a larger number of rays. Consequently, during December seven runs were made on the IBM 7094 at Eglin Air Force Base, Florida. At the end of December, five more runs were made on the 1620.

The results of production runs made through November are shown in tabular form in Table 2. The corresponding graphs are shown in Figures 4 through 13, in which the laboratory curves were taken from the interim report. The number of rays per angle interval is shown as an indication of the reliability of the data. Data averaged over 20 to 30 rays would be expected to exhibit less scatter than data averaged over 3 or 4 rays. There are a few exceptions, but this is the general rule. The notation E+XX in the data fields is a computer convention for powers of tens; thus .152662E-01 stands for $.152662 \times 10^{-1}$.

Figure 4 shows excellent agreement between the computer prediction and the laboratory measurement, even for the relatively small number of rays traced.

The agreement in Figure 5 is better than it appears, because the discrepancy along the 0°-line is somewhat arbitrary. The quantity R10 in the computer program represents the initial radiant intensity along the axis of the cylinder and is input data to the programs. The actual value used in most cases was obtained by averaging a large number of laboratory measurements. The value for a particular laboratory run usually varied somewhat from this average.

When normalized to the laboratory measurement, the prediction of Figure 6 agrees around to 40°, diverging thereafter to a difference at 70° by a factor of five. Part of this discrepancy may be attributable to inaccuracy in details of the quartic attenuation function at large angles, since these details had to be determined by extrapolation for angles greater than 60°. Furthermore, at all angles over 50°, no more than two rays were traced. The results of so few tracings can hardly be expected to give more than a rough estimate. This latter problem was largely overcome by going to the 7094 computer. Finally, the presence of an innerbody tends to attenuate the radiation more than simple ray-tracing predicts.

The configuration represented by Figure 7 has been the subject of concentrated efforts, partly because it is the fastest program and partly because of the sharp cut-off characteristic near 40°. One of the big

TABLE 2
RADIATION DISTRIBUTION DATA
(IBM 1620 RUNS)

| Configuration and Specifications | ϕ (degrees) | Average Radiant Intensity (watts/ster.) | No. of Rays |
|--|---------------------|---|-------------|
| Gold Cylinder | 0 | .381657E+02 | 4 |
| RIO .381819E-02 | 5 | .380185E+02 | 17 |
| RB 0 | 10 | .373501E+02 | 13 |
| RC 2.0 | 15 | .361472E+02 | 12 |
| RP 2.0 | 20 | .344524E+02 | 8 |
| CB 0 | 25 | .331676E+02 | 4 |
| CLEN 7.8125 | 30 | .314157E+02 | 15 |
| REFB 0 | 35 | .288938E+02 | 10 |
| REFC .969 | 40 | .267623E+02 | 20 |
| RAYS 200 | 45 | .238183E+02 | 9 |
| ALFA 0 | 50 | .217516E+02 | 12 |
| | 55 | .183599E+02 | 5 |
| | 60 | .158407E+02 | 6 |
| | 65 | .126643E+02 | 12 |
| | 70 | .951432E+02 | 10 |
| | 75 | .659243E+02 | 16 |
| | 80 | .353736E+02 | 10 |
| | 85 | .145087E+01 | 11 |
| | 90 | .239796E+00 | 6 |
| Black Cylinder | 0 | .381656E+02 | 15 |
| RIO .381819E-02 | 5 | .276907E+02 | 33 |
| RB 0 | 10 | .279422E+02 | 31 |
| RC 2.0 | 15 | .176851E+02 | 23 |
| RP 2.0 | 20 | .492566E+01 | 30 |
| CB 0 | 25 | .171084E+00 | 19 |
| CLEN 7.8125 | 30 | .126899E+00 | 37 |
| REFB 0 | 35 | .987140E-01 | 23 |
| REFC .005 | 40 | .571691E-01 | 40 |
| RAYS 300 | 45 | .641878E-03 | 29 |
| ALFA 0 | 50 | .576748E-03 | 20 |

TABLE 2 (CONT'D.)
RADIATION DISTRIBUTION DATA
(IBM 1620 RUNS)

| Configuration and Specifications | θ (degrees) | Average Radiant Intensity (watts/ster.) | No. of Rays |
|--|-----------------------|---|-------------|
| Gold Cylinder and Gold Innerbody | 0 | .360304E+02 | 4 |
| | 5 | .353488E+02 | 3 |
| RIO .381819E-02 | 10 | .338507E+02 | 12 |
| RB 1.5 | 15 | .319862E+02 | 17 |
| RC 2.0 | 20 | .315814E+02 | 19 |
| RP 2.0 | 25 | .270390E+02 | 6 |
| CB 6.3125 | 30 | .269472E+02 | 9 |
| CLEN 7.8125 | 35 | .248724E+02 | 8 |
| REFB .950 | 40 | .188747E+02 | 5 |
| REFC .950 | 45 | .226567E+02 | 5 |
| RAYS 100 | 50 | .163547E+02 | 2 |
| ALFA 0 | 55 | .253561E+02 | 2 |
| | 60 | .115586E+02 | 1 |
| | 65 | .926428E+01 | 2 |
| | 70 | .713797E+01 | 1 |
| | 75 | .366703E+01 | 2 |
| | 80 | .223205E+01 | 2 |
| Gold Large Cone | 0 | .588903E+02 | 14 |
| RIO .381819E-02 | 5 | .562916E+02 | 45 |
| RB 0 | 10 | .546149E+02 | 51 |
| RC 2.5 | 15 | .465935E+02 | 72 |
| RP 1.375 | 20 | .387182E+02 | 69 |
| CB 0 | 25 | .250352E+02 | 90 |
| CLEN 8.0 | 30 | .180986E+02 | 101 |
| REFB 0 | 35 | .148748E+02 | 42 |
| REFC .95 | 40 | .438172E+01 | 16 |
| RAYS 500 | | | |
| ALFA .1396 | | | |

TABLE 2 (CONT'D.)
RADIATION DISTRIBUTION DATA
(IBM 1620 RUNS)

| Configuration and Specifications | ϕ (degrees) | Average Radiant Intensity (watts/ster.) | No. of Rays |
|--|---------------------|---|-------------|
| Black Large Cone | 0 | .434506E+02 | 22 |
| RIO .381819E-02 | 5 | .269288E+02 | 71 |
| RB 0 | 10 | .303066E+02 | 66 |
| RC 2.5 | 15 | .136240E+02 | 85 |
| RP 1.375 | 20 | .342977E+01 | 101 |
| CB 0 | 25 | .124669E+00 | 85 |
| CLEN 8.0 | 30 | .637961E-01 | 57 |
| REFB 0 | 35 | .125760E+00 | 13 |
| REFC .005 | | | |
| RAYS 500 | | | |
| ALFA .1396 | | | |
| Gold Large Cone and Gold Innerbody | 0 | .407030E+02 | 3 |
| | 5 | .495897E+02 | 26 |
| RIO .350E-02 | 10 | .449230E+02 | 32 |
| RB 1.75 | 15 | .427347E+02 | 29 |
| RC 2.5 | 20 | .308968E+02 | 29 |
| RP 1.375 | 25 | .275685E+02 | 32 |
| CB 6.25 | 30 | .217220E+02 | 28 |
| CLEN 8.0 | 35 | .205582E+02 | 8 |
| REFB .95 | 40 | .258950E+02 | 9 |
| REFC .95 | 45 | .256665E+02 | 4 |
| RAYS 200 | | | |
| ALFA .1396 | | | |
| Gold Small Cone | 0 | .180428E+02 | 22 |
| RIO .381819E-02 | 5 | .179811E+02 | 31 |
| RB 0 | 10 | .177624E+02 | 31 |
| RC 1.375 | 15 | .171838E+02 | 32 |
| RP 2.5 | 20 | .169863E+02 | 31 |
| CB 0 | 25 | .167545E+02 | 32 |
| CLEN 8.0 | 30 | .165136E+02 | 41 |
| REFB 0 | 35 | .160063E+02 | 33 |
| REFC .95 | 40 | .152817E+02 | 24 |
| RAYS 400 | 45 | .152970E+02 | 10 |
| ALFA -.1396 | 50 | .148706E+02 | 17 |

TABLE 2 (CONT'D.)
RADIATION DISTRIBUTION DATA
(IBM 1620 RUNS)

| Configuration and Specifications | ϕ (degrees) | Average Radiant Intensity (watts/ster.) | No. of Rays |
|--|---------------------|---|-------------|
| Gold Small Cone | 55 | .147235E+02 | 14 |
| (Cont'd.) | 60 | .134366E+02 | 34 |
| | 65 | .132366E+02 | 23 |
| | 70 | .128122E+02 | 19 |
| | 75 | - | 0 |
| | 80 | .117826E+02 | 6 |
| Gold Small Cone and | 0 | .180433E+02 | 11 |
| Gold Innerbody | 5 | .177131E+02 | 20 |
| RIO .381819E-02 | 10 | .173296E+02 | 16 |
| RB 1.0 | 15 | .161585E+02 | 33 |
| RC 1.375 | 20 | .162184E+02 | 42 |
| RP 2.500 | 25 | .159515E+02 | 30 |
| CB 7.0 | 30 | .156533E+02 | 47 |
| CLEN 8.0 | 35 | .147551E+02 | 28 |
| REFB .95 | 40 | .149051E+02 | 19 |
| REFC .95 | 45 | .148379E+02 | 28 |
| RAYS 400 | 50 | .139076E+02 | 33 |
| ALFA -.1396 | 55 | .137101E+02 | 22 |
| | 60 | .133707E+02 | 30 |
| | 65 | .131336E+02 | 11 |
| | 70 | .121432E+02 | 6 |
| | 75 | .113070E+02 | 12 |
| | 80 | .109579E+02 | 9 |
| | 85 | .845597E+01 | 3 |
| Gold Double Cone | 0 | .313432E+02 | 10 |
| RIO .381819E-02 | 5 | .304695E+02 | 46 |
| RC 1.8125 | 10 | .290311E+02 | 23 |
| RM 2.3437 | 15 | .280014E+02 | 17 |
| RP 1.5625 | 20 | .225717E+02 | 30 |
| RB 0 | 25 | .198778E+02 | 28 |
| CB 0 | 30 | .177679E+02 | 35 |
| CLEN 5.5 | 35 | .248925E+02 | 26 |
| ZM 2.9375 | 40 | .217852E+02 | 29 |
| REFC 1 .95 | 45 | .247496E+02 | 29 |
| REFC 2 .95 | 50 | .202480E+02 | 40 |
| REFB 0 | 55 | .206132E+02 | 41 |

TABLE 2 (CONT'D.)
RADIATION DISTRIBUTION DATA
(IBM 1620 RUNS)

| Configuration and Specifications | ϕ (degrees) | Average Radiant Intensity (watts/ster.) | No. of Rays |
|--|---------------------|---|-------------|
| Gold Double Cone | 60 | .168658E+02 | 16 |
| (Cont'd.) | 65 | .107599E+02 | 11 |
| RAYS 400 | 70 | .122692E+02 | 4 |
| ALFA 1 .2598 | 75 | .139540E+02 | 3 |
| ALFA 2 -.2042 | 80 | .110883E+02 | 8 |
| | 85 | .174685E+02 | 3 |
| Gold Double Cone and | 0 | - | 0 |
| Gold Innerbody | 5 | .187669E+02 | 13 |
| RIO .381819E-02 | 10 | .207801E+02 | 22 |
| RC 1.8125 | 15 | .190052E+02 | 14 |
| RM 2.3437 | 20 | .198098E+02 | 27 |
| RP 1.5625 | 25 | .216940E+02 | 38 |
| RB 1.75 | 30 | .207317E+02 | 53 |
| CB 2.9375 | 35 | .190096E+02 | 49 |
| CLEN 5.5 | 40 | .219302E+02 | 41 |
| ZM 2.9375 | 45 | .201971E+02 | 35 |
| REFC 1 .95 | 50 | .182820E+02 | 41 |
| REFC 2 .95 | 55 | .150247E+02 | 35 |
| REFB .95 | 60 | .144817E+02 | 13 |
| RAYS 400 | 65 | .117407E+02 | 12 |
| ALFA 1 .2598 | 70 | .300514E+01 | 4 |
| ALFA 2 -.2042 | 75 | .148839E+02 | 1 |
| | 80 | - | 0 |
| | 85 | .123987E+02 | 2 |

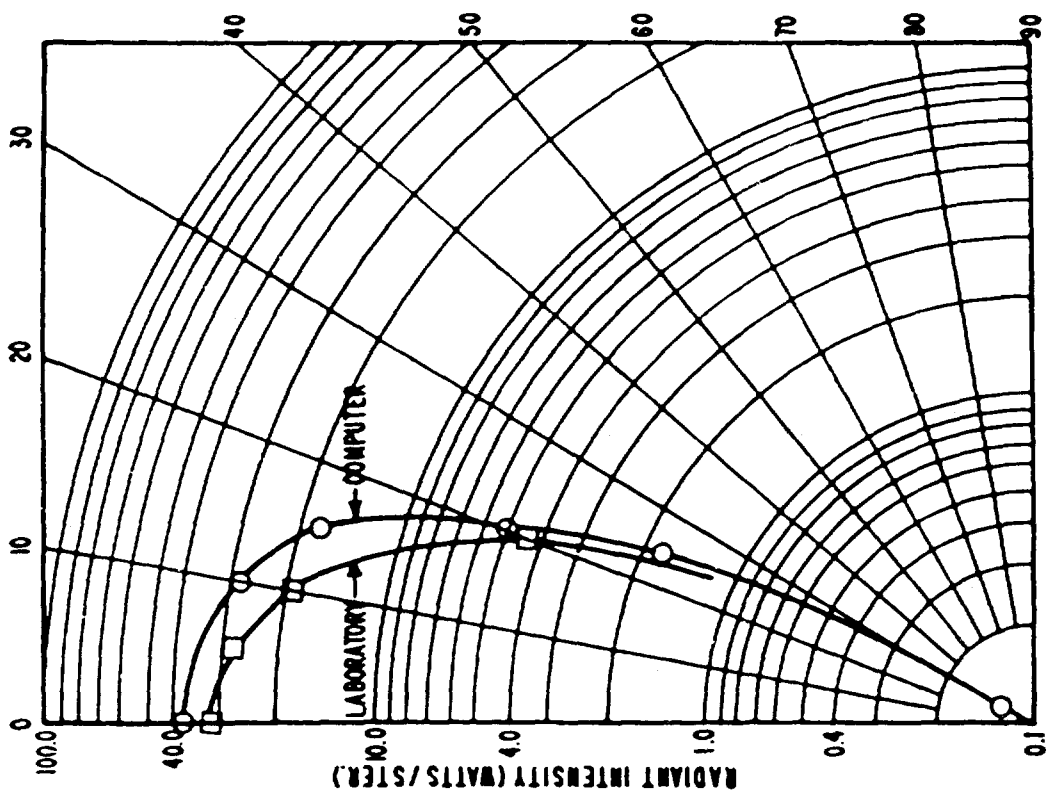


Figure 5. Black Cylinder without Innerbody.

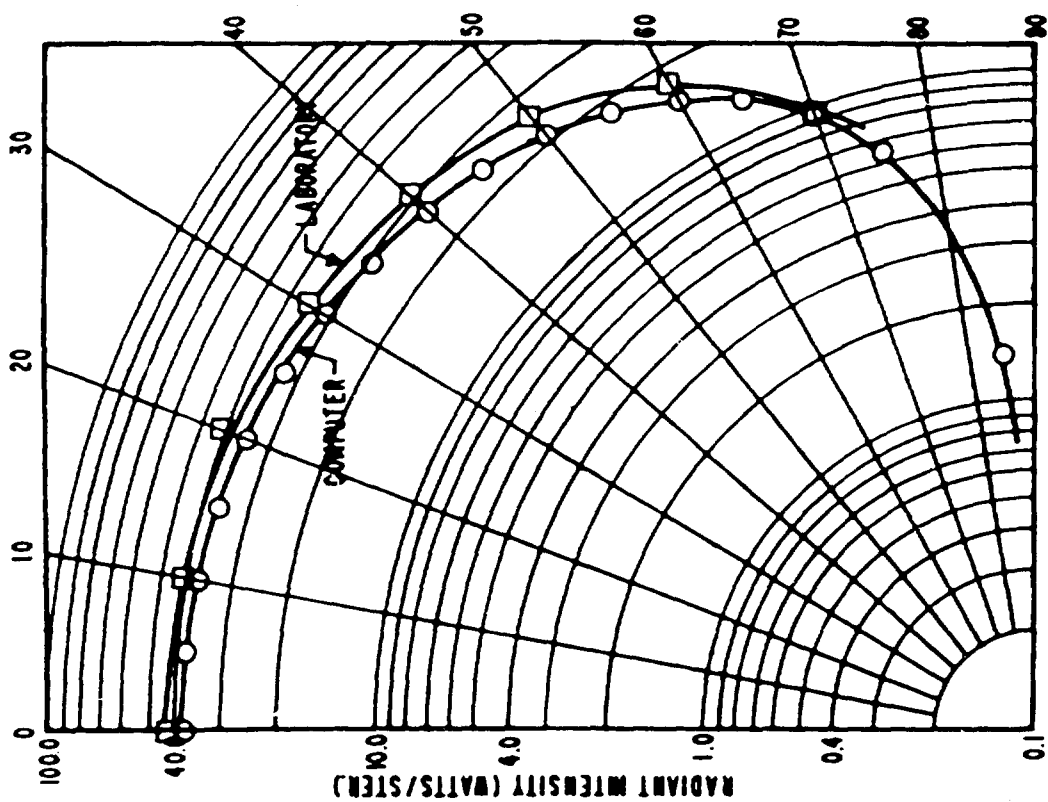


Figure 4. Gold Cylinder without Innerbody.

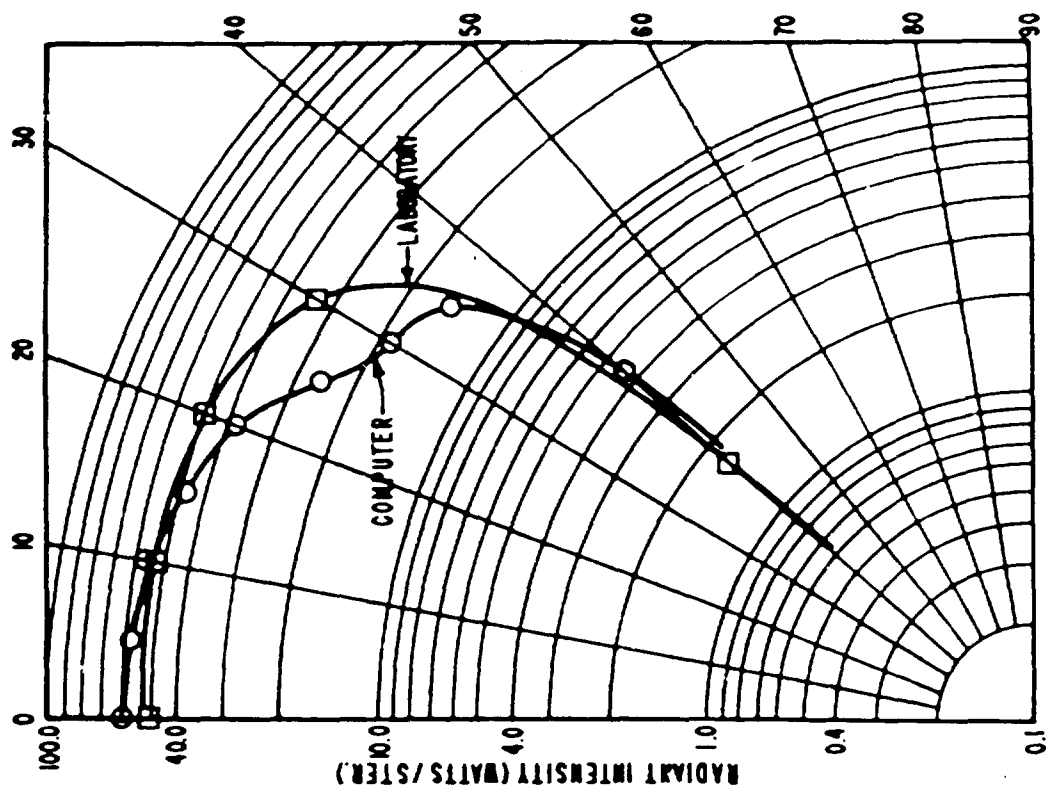


Figure 6. Gold Cylinder with Gold Innerbody.

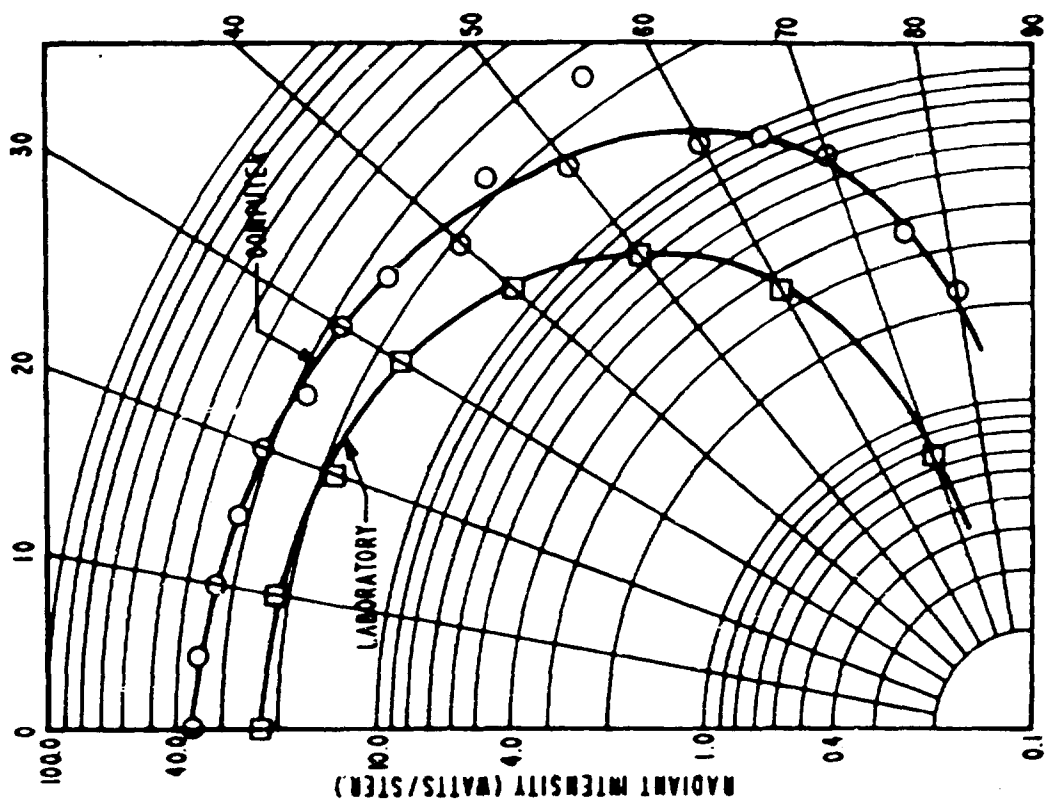


Figure 7. Gold Large Cone without Innerbody.

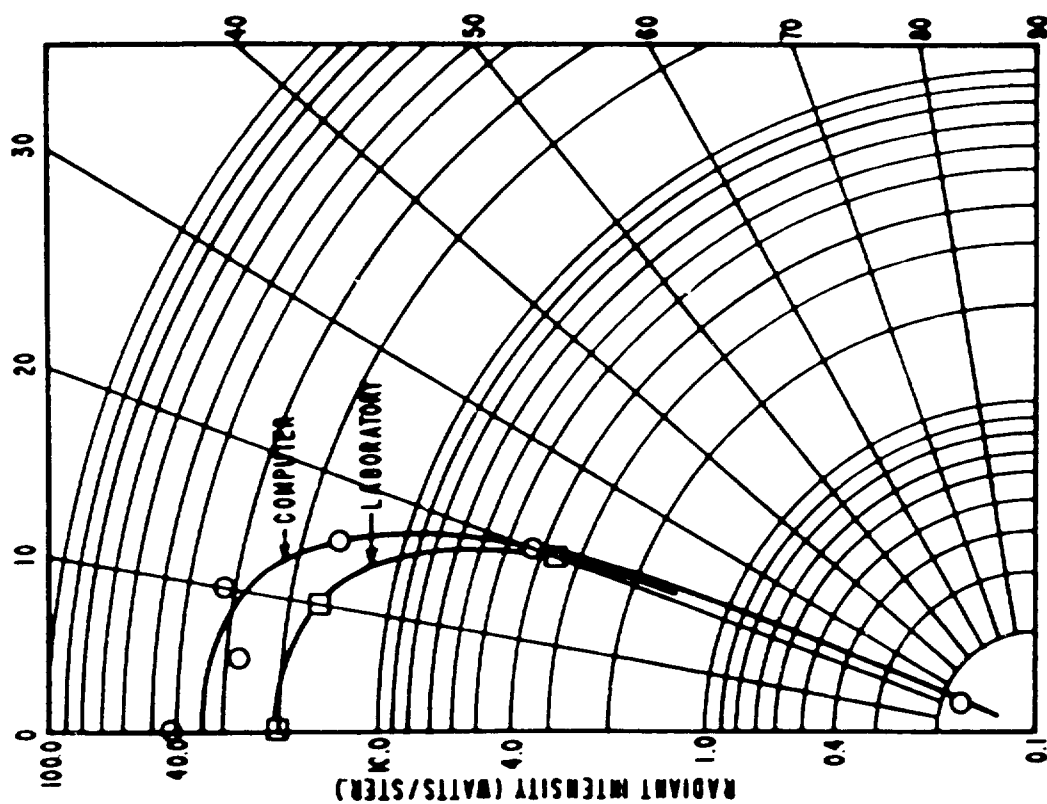


Figure 8. Black Large Cone without Innerbody.

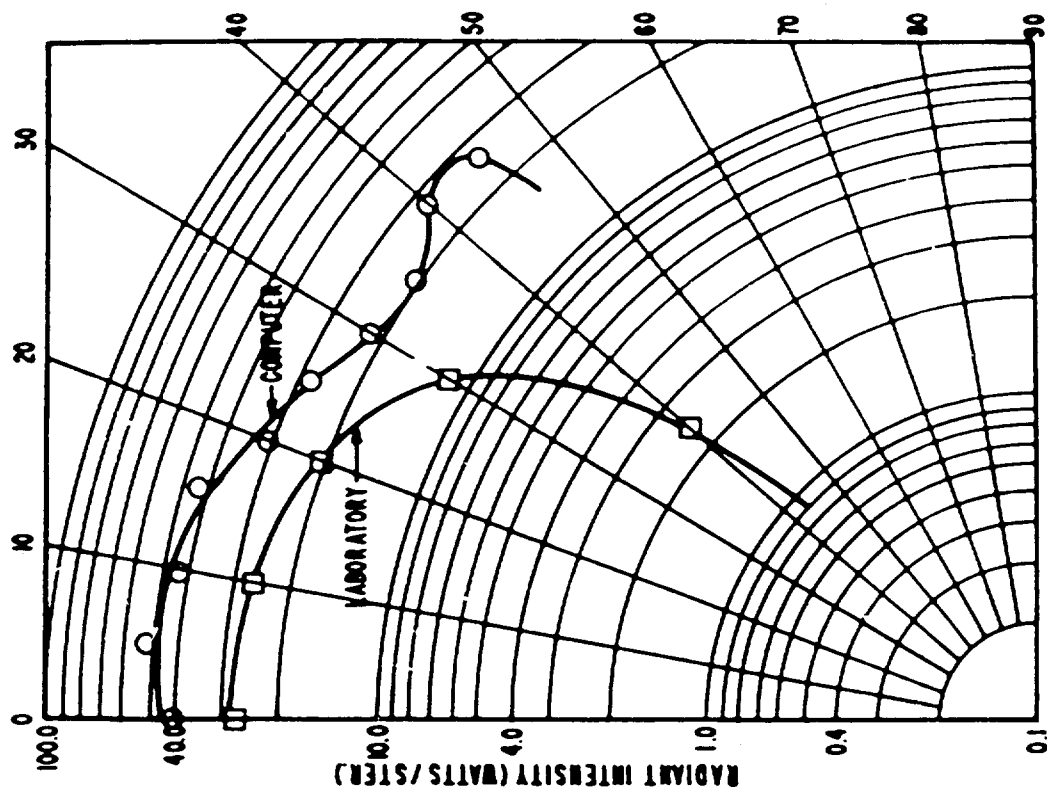


Figure 9. Gold Large Cone with Gold Innerbody.

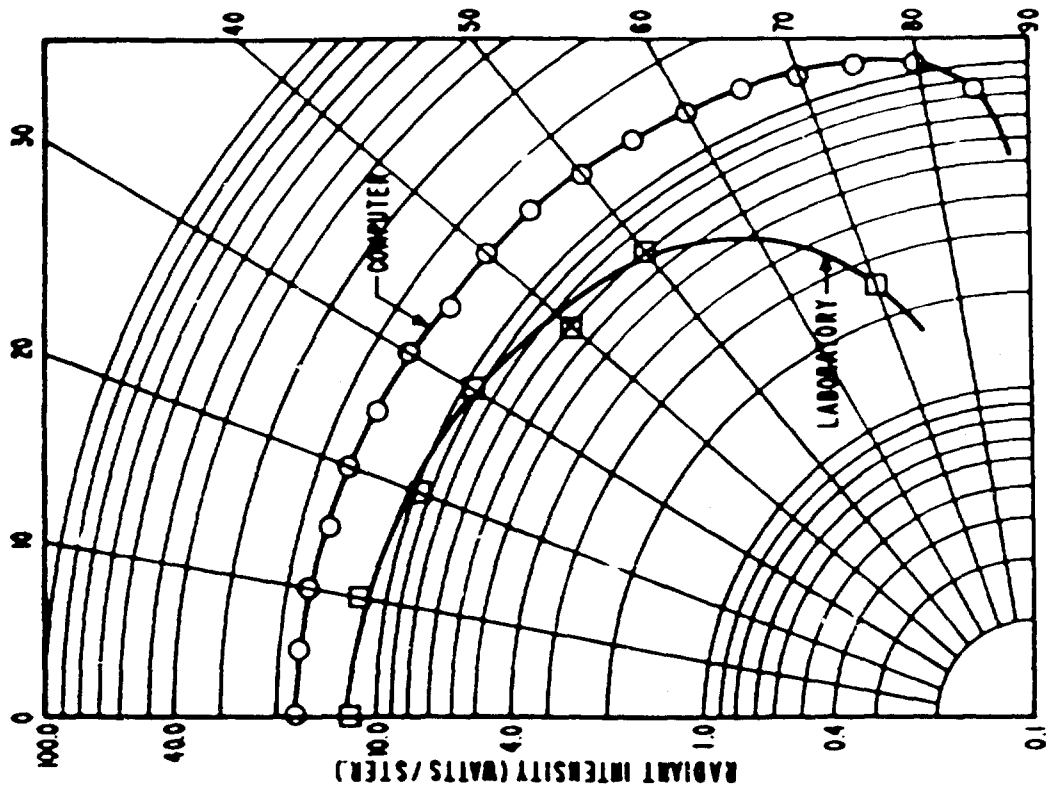


Figure 10. Gold Small Cone without Innerbody.

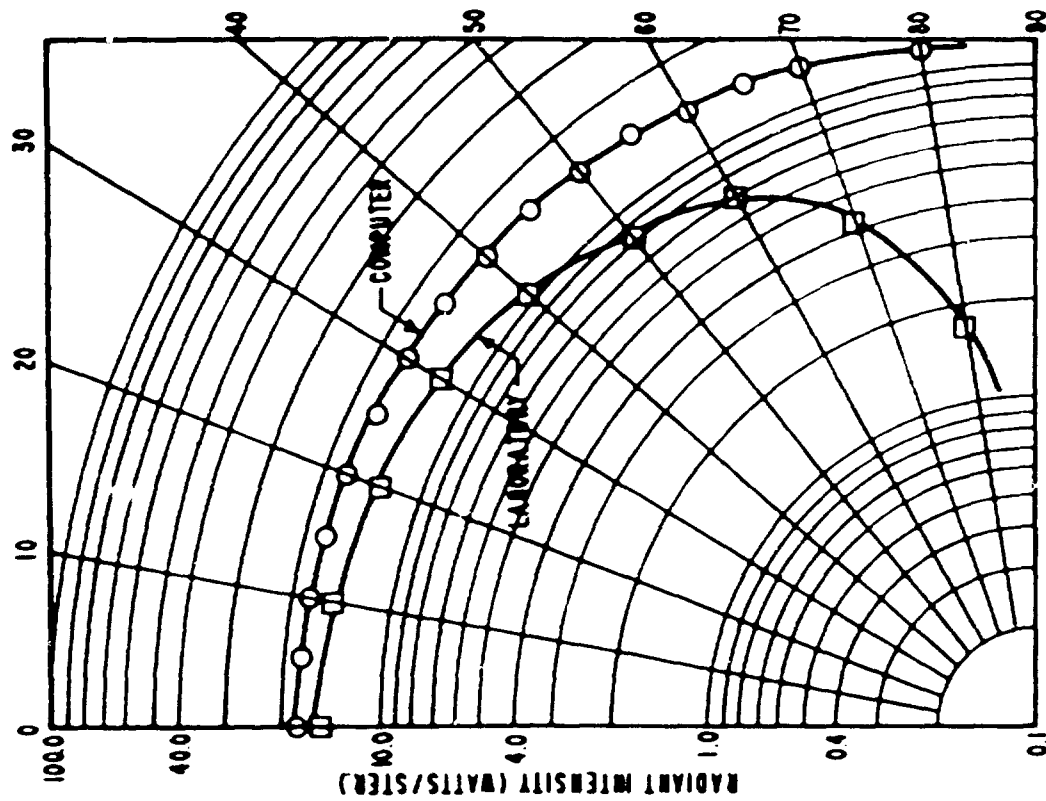


Figure 11. Gold Small Cone with Gold Innerbody.

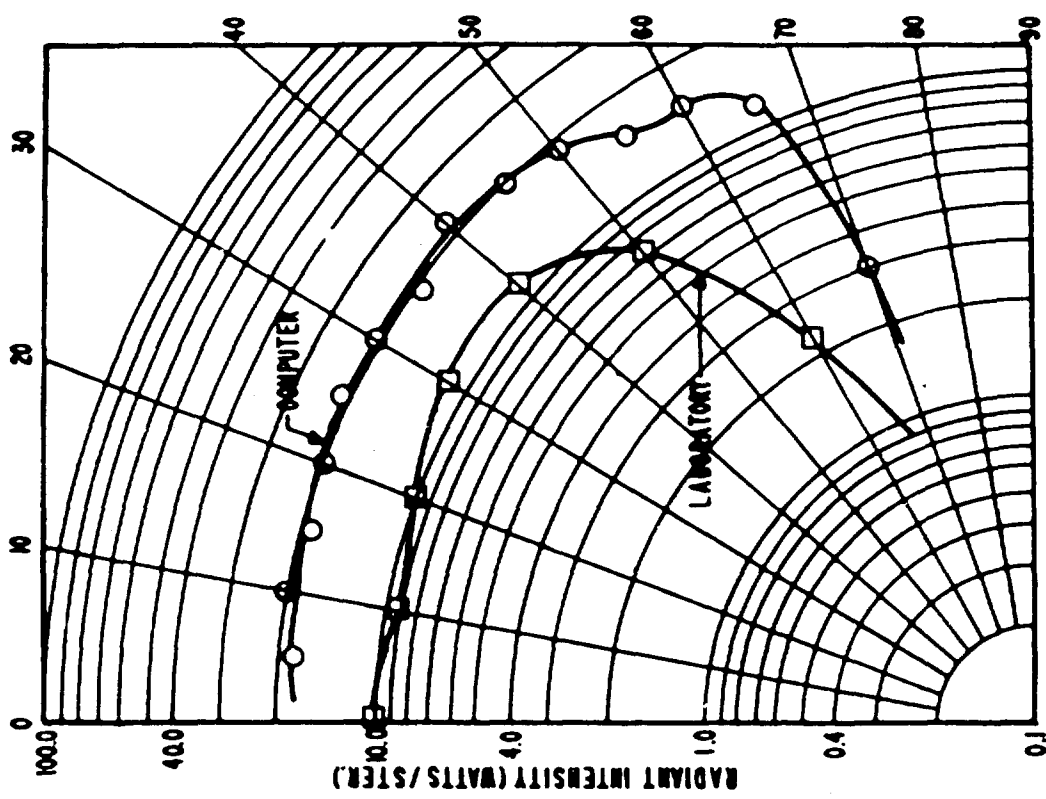


Figure 12. Gold Double Cone without Innerbody.

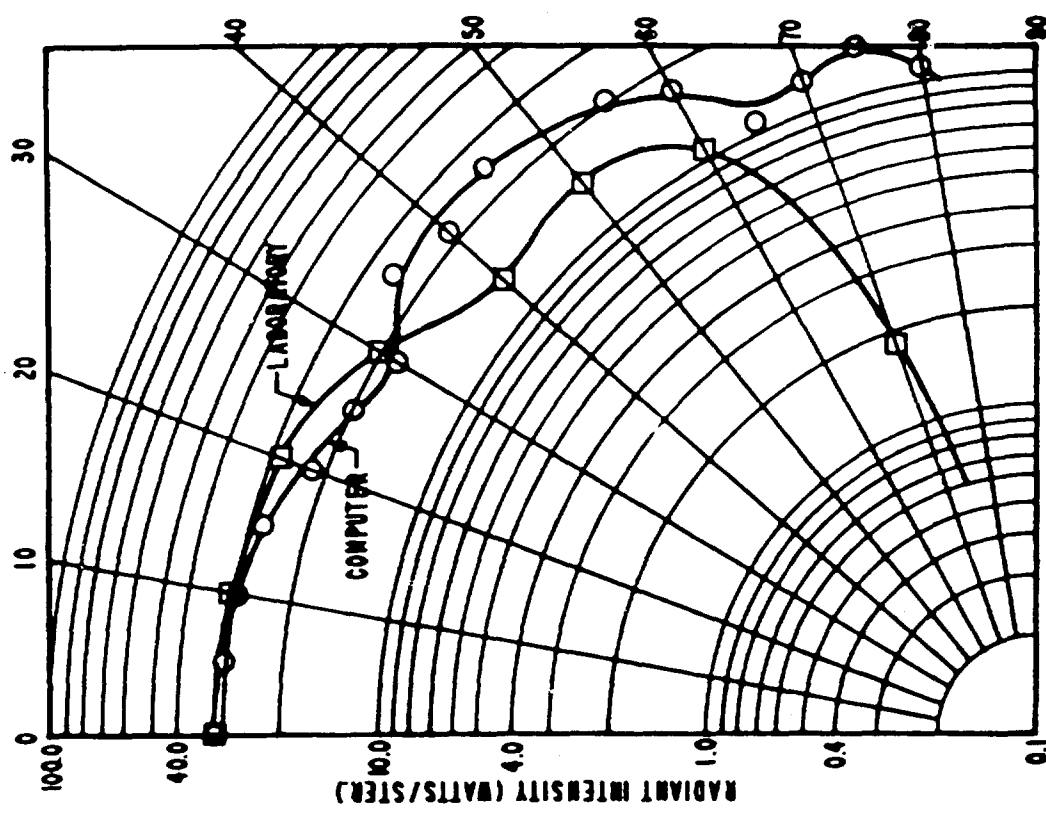


Figure 13. Gold Double Cone with Gold Innerbody.

problems has been the slight bulge between 30° and 35°, which becomes quite pronounced when the innerbody is added. A slight change in the program, to be described presently, reduced this problem somewhat.

Figure 8 shows the effect of a low-reflectivity surface material. Except for the on-axis discrepancy, the two curves probably could be brought into good agreement by varying the value of the surface reflectivity.

Figure 9 represents the large cone with innerbody. As mentioned above, the hump at 40° to 45° is the biggest problem. No completely satisfactory solution to this problem has been devised.

Figures 7 and 10 played a prominent part in the formulation of an early empirical correction factor, designed to correct the diverging discrepancy at large angles. The correction factor was of the form

$$f(\phi, \frac{RC}{RP}) = [\cos \phi]^{1.5} \left[1 - \left(\frac{RC}{RP} \right)^2 \right]$$

in which the quantities ϕ , RC, and RP have the same significance as in the tabulated data. This multiplicative factor had the effect of boosting, with increasing ϕ , the radiant intensity for the large cone and of attenuating that of the small cone, while leaving the cylinder unchanged. The factor, however, was not applicable when innerbodies were present or for double cone configurations. Extensive efforts were made to develop an empirical expression which would correlate predictions with laboratory measurement for all configurations simply by substituting the appropriate values of certain geometrical parameters. These attempts were unsuccessful.

The characteristic feature of the laboratory curve for the double cone (Figure 12) is the depression at 40°. This configuration has been run several times, and the depression always occurs somewhere between 25° and 30°. It is felt that the points beyond 65° are not reliable, because the number of rays traced dropped sharply in this region.

When normalized to the laboratory on-axis value, the prediction shown in Figure 13 agrees well with the experimental curve around to about 50°. Again, the points beyond 65° are susceptible to suspicion because of the paucity of rays traced.

The problem of correlating prediction curves with laboratory curves led to repeated efforts to develop a suitable correlation factor. It did not seem unreasonable that such a factor might be needed, for a simple macroscopic averaging technique was being used to simulate a complex quantum process. It was thought that perhaps the distribution of rays might provide a statistical correction factor, but to explore this possibility, it was necessary to trace many times the number of rays that could be traced on the 1620 computer. It has been noted, also,

that the small number of rays traced might be responsible for the large degree of scatter, particularly at large angles. In order to trace the large number of rays needed in economically feasible times, it was necessary to go to a faster computer. For this task, the IBM 7094 at Eglin Air Force Base, Florida, was chosen. Seven configurations were run, each for 10,000 rays. It turned out that one run, which would have required 250 hours on the 1620, was completed on the 7094 in less than 7 minutes. Another run, requiring 60 hours on the 1620, ran to completion in 2.1 minutes on the 7094. The tabulated data from these runs is shown in Table 3. The corresponding graphs are shown in Figures 14 through 20.

Figure 14 bears a close resemblance to Figure 4, except the scatter is reduced and the tail of the prediction curve is about 65% closer to the laboratory curve. This points up the magnitude of change that is possible when a relatively large number of rays are traced.

In Figure 15 the agreement is improved at 30°, but worsened at 40°.

Figure 16 shows an improvement over the corresponding earlier graph, Figure 8. When normalized to the on-axis laboratory value, the two curves of Figure 14 nearly coincide.

Figures 17 and 18 are essentially the same as the earlier predictions. The main difference in Figure 19 is in the region of 65° to 70°. The points beyond 70° were inexplicably high. Finally, Figure 20 was essentially unchanged.

After the completion of these runs, a change was made in the base plane attenuation function (Eq. 1). Figure 21 shows the quartic attenuation function of Eq. 1 and the estimated laboratory curve. Since a number of the predictions were unexpectedly high at large angles (greater than 70°), it was felt that altering the attenuation function to better fit the laboratory curve might improve the prediction curves. Two terms were added, giving the attenuation function the form

$$f(\phi) = -.01463 \phi^6 + .0701 \phi^4 - .5786 \phi^2 - .22 \sin^{10} \phi + 1. \quad (2)$$

The revised function is also shown in Figure 21. Two short runs were made on the large cone configurations (Figures 22 and 23). The configuration without innerbody showed a slight improvement at 40°, but the configuration with innerbody (158 rays traced) showed so much scatter that a conclusive curve could not be drawn. Notably, however, the range was extended to 50°.

At the conclusion of these studies, four additional runs were made on the double cone program, simulating configurations for which there were

TABLE 3
RADIATION DISTRIBUTION DATA
(IBM 7094 RUNS)

| Configuration and Specifications | ϕ (degrees) | Average Radiant Intensity (watts/ster.) | No. of Rays |
|--|---------------------|---|-------------|
| Gold Cylinder and | 0 | .381630E+02 | 220 |
| Gold Innerbody | 5 | .345476E+02 | 734 |
| RIO .381819E-02 | 10 | .320656E+02 | 1084 |
| RB 1.5 | 15 | .311343E+02 | 1058 |
| RC 2.0 | 20 | .296948E+02 | 1247 |
| RP 2.0 | 25 | .260420E+02 | 873 |
| CB 6.3125 | 30 | .235387E+02 | 1084 |
| CLEN 7.8125 | 35 | .223240E+02 | 817 |
| REFB .90 | 40 | .202803E+02 | 677 |
| REFC .90 | 45 | .203205E+02 | 763 |
| RAYS 10000 | 50 | .153449E+02 | 324 |
| ALFA 0 | 55 | .132982E+02 | 547 |
| | 60 | .106233E+02 | 273 |
| | 65 | .732909E+01 | 136 |
| | 70 | .450041E+01 | 136 |
| | 75 | .134207E+01 | 27 |
| Gold Large Cone | 0 | .580217E+02 | 352 |
| RIO .381819E-02 | 5 | .563407E+02 | 1564 |
| RB 0 | 10 | .536843E+02 | 1732 |
| RC 2.5 | 15 | .461120E+02 | 1647 |
| RP 1.375 | 20 | .403341E+02 | 1500 |
| CB 0 | 25 | .310808E+02 | 1489 |
| CLEN 8.0 | 30 | .225956E+02 | 1026 |
| REFB 0 | 35 | .144971E+02 | 606 |
| REFC .90 | 40 | .965673E+01 | 84 |
| RAYS 10000 | | | |
| ALFA .1396 | | | |

TABLE 3 (CONT'D.)
RADIATION DISTRIBUTION DATA
(IBM 7094 RJNS)

| Configuration and Specifications | ϕ (degrees) | Average Radiant Intensity (watts/ster.) | No. of Rays |
|--|---------------------|---|-------------|
| Black Large Cone | 0 | .436898E+02 | 402 |
| RIO .381819E-02 | 5 | .324186E+02 | 1469 |
| RB 0 | 10 | .303687E+02 | 1921 |
| RC 2.5 | 15 | .189675E+02 | 1939 |
| RP 1.375 | 20 | .739769E+01 | 1973 |
| CB 0 | 25 | .227655E+01 | 1401 |
| CLEN 8.0 | 30 | .772978E+01 | 713 |
| REFB 0 | 35 | .731115E+01 | 182 |
| REFC .50 | | | |
| RAYS 10000 | | | |
| ALFA .1396 | | | |
| Gold Large Cond and Gold Innerbody | 0 | .409017E+02 | 95 |
| | 5 | .490714E+02 | 1235 |
| RIO .381819E-02 | 10 | .451746E+02 | 1666 |
| RB 1.75 | 15 | .382927E+02 | 1632 |
| RC 2.50 | 20 | .313438E+02 | 1527 |
| RP 1.375 | 25 | .252095E+02 | 1426 |
| CB 6.25 | 30 | .185244E+02 | 1290 |
| CLEN 8.0 | 35 | .157011E+02 | 447 |
| REFB .90 | 40 | .167201E+02 | 517 |
| REFC .90 | 45 | .178990E+02 | 165 |
| RAYS 10000 | | | |
| ALFA .1396 | | | |
| Gold Small Cone and Gold Innerbody | 0 | .180414E+02 | 286 |
| | 5 | .177788E+02 | 323 |
| RIO .381819E-02 | 10 | .171025E+02 | 467 |
| RB 1.0 | 15 | .165894E+02 | 935 |
| RC 1.375 | 20 | .163068E+02 | 1222 |
| RP 2.5 | 25 | .161458E+02 | 648 |
| CB 7.0 | 30 | .155478E+02 | 1050 |
| CLEN 8.0 | 35 | .152107E+02 | 969 |
| REFB .95 | 40 | .150018E+02 | 496 |
| REFC .95 | 45 | .147765E+02 | 791 |
| RAYS 10000 | 50 | .139760E+02 | 611 |
| ALFA -.1396 | 55 | .138936E+02 | 728 |

TABLE 3 (CONT'D.)
RADIATION DISTRIBUTION DATA
(IBM 7094 RUNS)

| Configuration and Specifications | ϕ (degrees) | Average Radiant Intensity (watts/ster.) | No. of Rays |
|--|---------------------|---|-------------|
| Gold Small Cone and | 60 | .133401E+02 | 504 |
| Gold Innerbody (Cont'd.) | 65 | .128702E+02 | 395 |
| | 70 | .116750E+02 | 108 |
| | 75 | .112730E+02 | 180 |
| | 80 | .108286E+02 | 215 |
| | 85 | .908789E+01 | 72 |
| Gold Double Cone | 0 | .313486E+02 | 357 |
| RIO .381819E-02 | 5 | .303865E+02 | 920 |
| RC 1.8125 | 10 | .304420E+02 | 732 |
| RM 2.3437 | 15 | .262457E+02 | 578 |
| RP 1.5625 | 20 | .239363E+02 | 682 |
| RB 0 | 25 | .193568E+02 | 850 |
| CB 0 | 30 | .189916E+02 | 919 |
| CLEN 5.5 | 35 | .225223E+02 | 749 |
| ZM 2.9397 | 40 | .223933E+02 | 787 |
| REFC 1 .95 | 45 | .242015E+02 | 629 |
| REFC 2 .95 | 50 | .225313E+02 | 834 |
| REFB 0 | 55 | .209491E+02 | 650 |
| RAYS 10000 | 60 | .175506E+02 | 460 |
| ALFA 1 .2598 | 65 | .126358E+02 | 324 |
| ALFA 2 -.2042 | 70 | .904595E+01 | 119 |
| | 75 | .405550E+01 | 120 |
| | 80 | .117768E+02 | 137 |
| | 85 | .196587E+02 | 119 |
| | 90 | .139184E+02 | 34 |
| Gold Double Cone and | 0 | .246849E+02 | 76 |
| Gold Ball | 5 | .214027E+02 | 257 |
| RIO .381819E-02 | 10 | .205852E+02 | 439 |
| RC 1.8125 | 15 | .197043E+02 | 567 |
| RM 2.3437 | 20 | .206064E+02 | 849 |
| RP 1.5625 | 25 | .223031E+02 | 772 |
| RB 1.75 | 30 | .204937E+02 | 1005 |
| CB 2.9397 | 35 | .202852E+02 | 902 |
| CLEN 5.5 | 40 | .215292E+02 | 1333 |
| ZM 2.9397 | 45 | .197642E+02 | 1173 |

TABLE 3 (CONT'D.)
RADIATION DISTRIBUTION DATA
(IBM 7094 RUNS)

| Configuration and Specifications | ϕ (degrees) | Average Radiant Intensity (watts/ster.) | No. of Rays |
|--|---------------------|---|-------------|
| Gold Double Cone and | 50 | .193257E+02 | 1080 |
| Gold Ball (Cont'd.) | 55 | .145337E+02 | 645 |
| REFC 1 .95 | 60 | .143116E+02 | 438 |
| REFC 2 .95 | 65 | .118780E+02 | 310 |
| REFB .95 | 70 | .503135E+01 | 77 |
| RAVS 10000 | 75 | .148840E+02 | 26 |
| ALFA 1 .2598 | 80 | - | 7 |
| ALFA 2 -.2042 | 85 | .123988E+02 | 26 |
| | 90 | .138592E+02 | 25 |

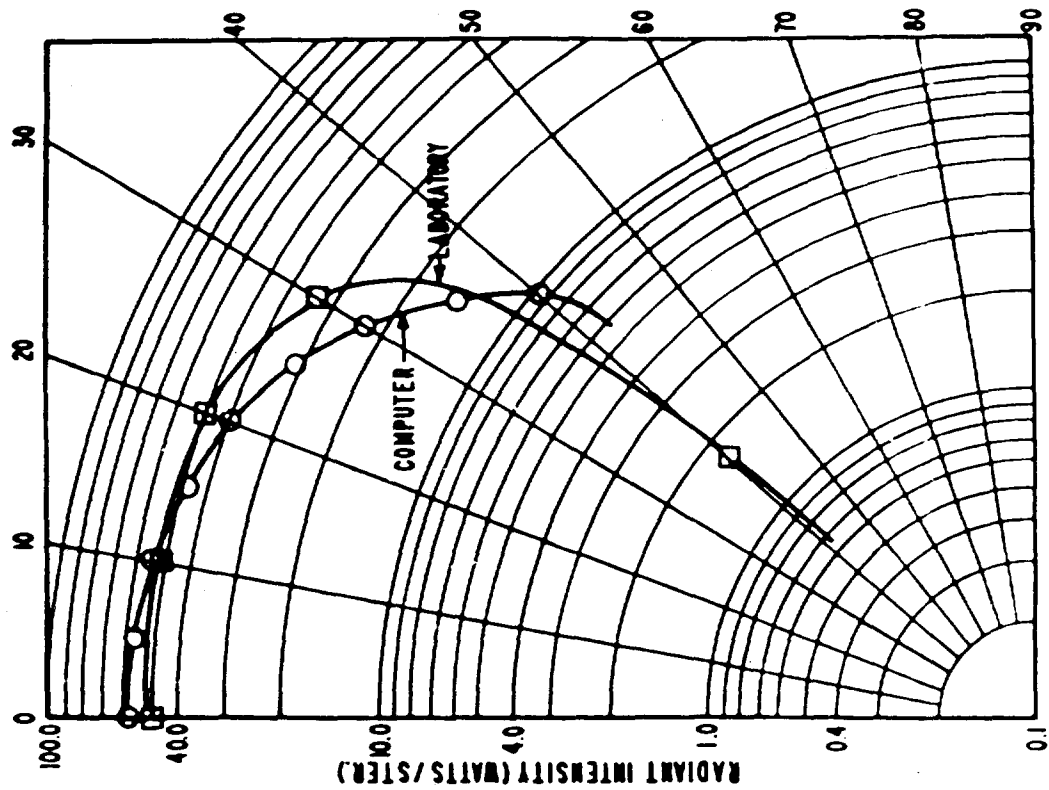


Figure 16. Gel: Large Cone without Innerbody.

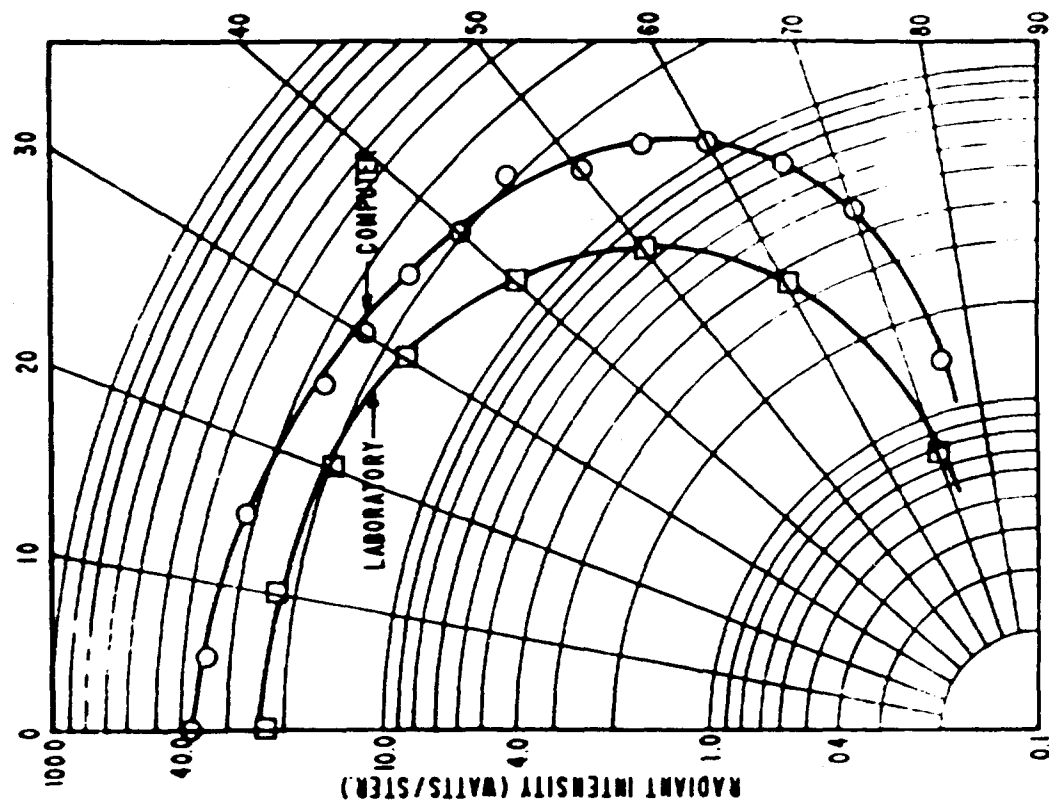


Figure 17. Gel: Cylinder with Gel Innerbody.

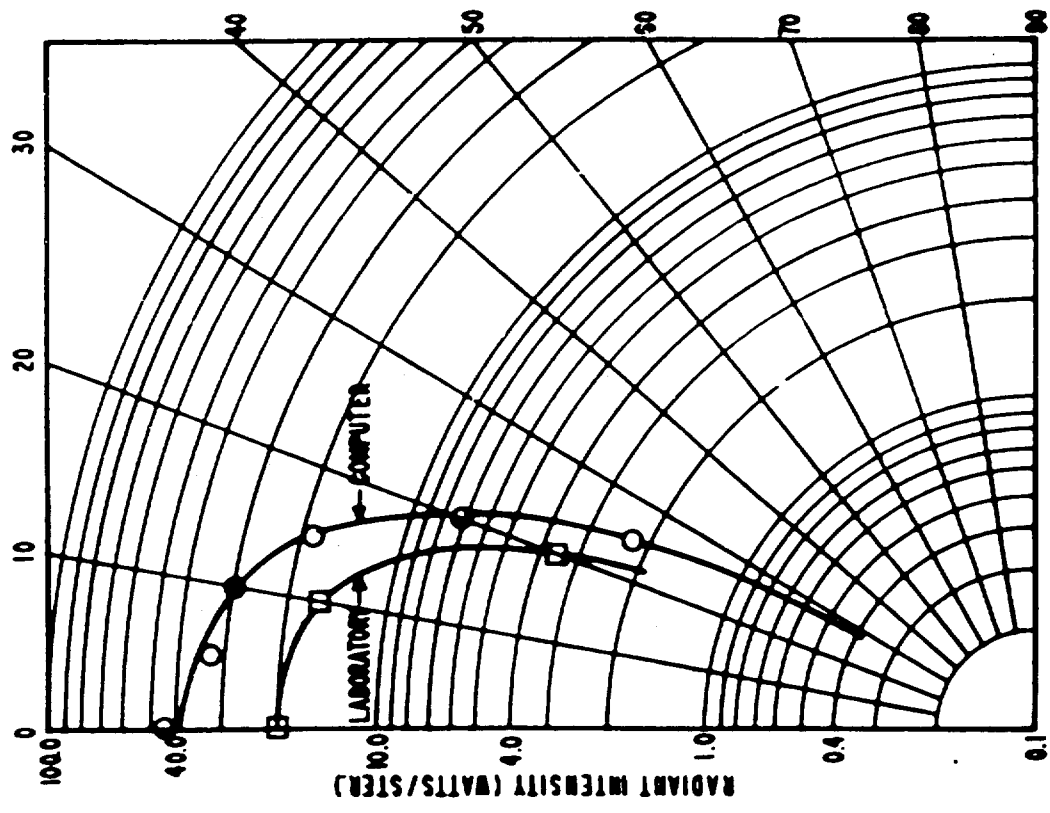


Figure 16. Black Large Cone without Innerbody.

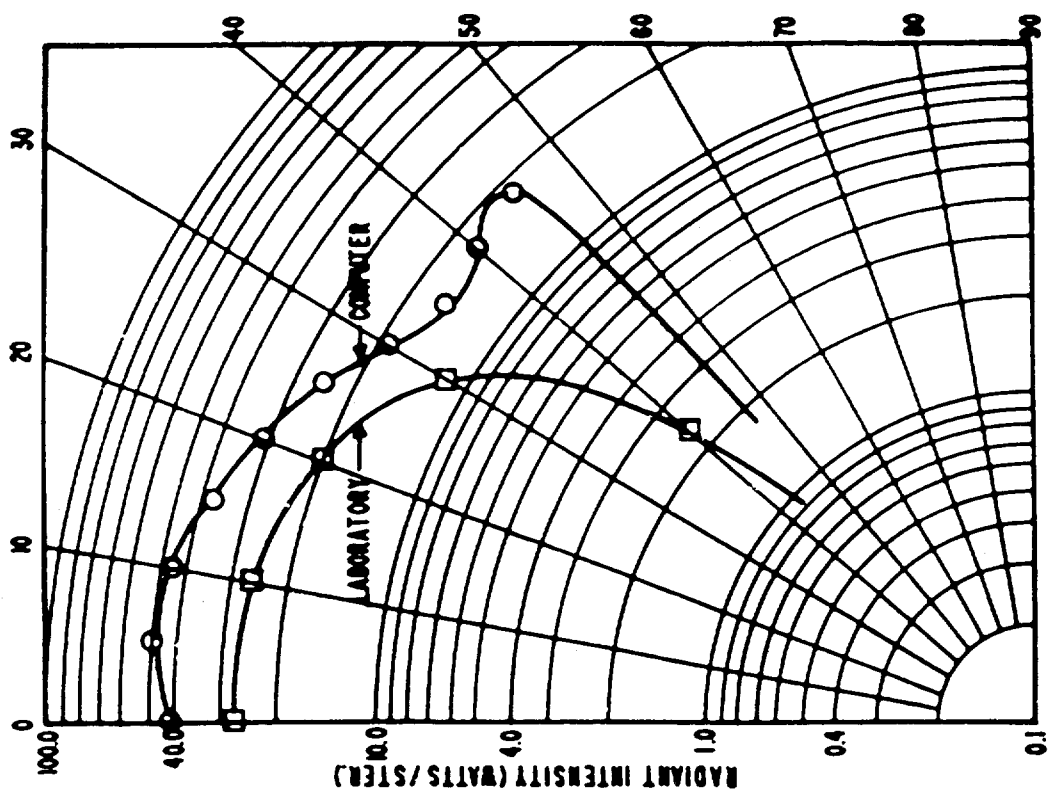


Figure 17. Gold Large Cone with Gold Innerbody.

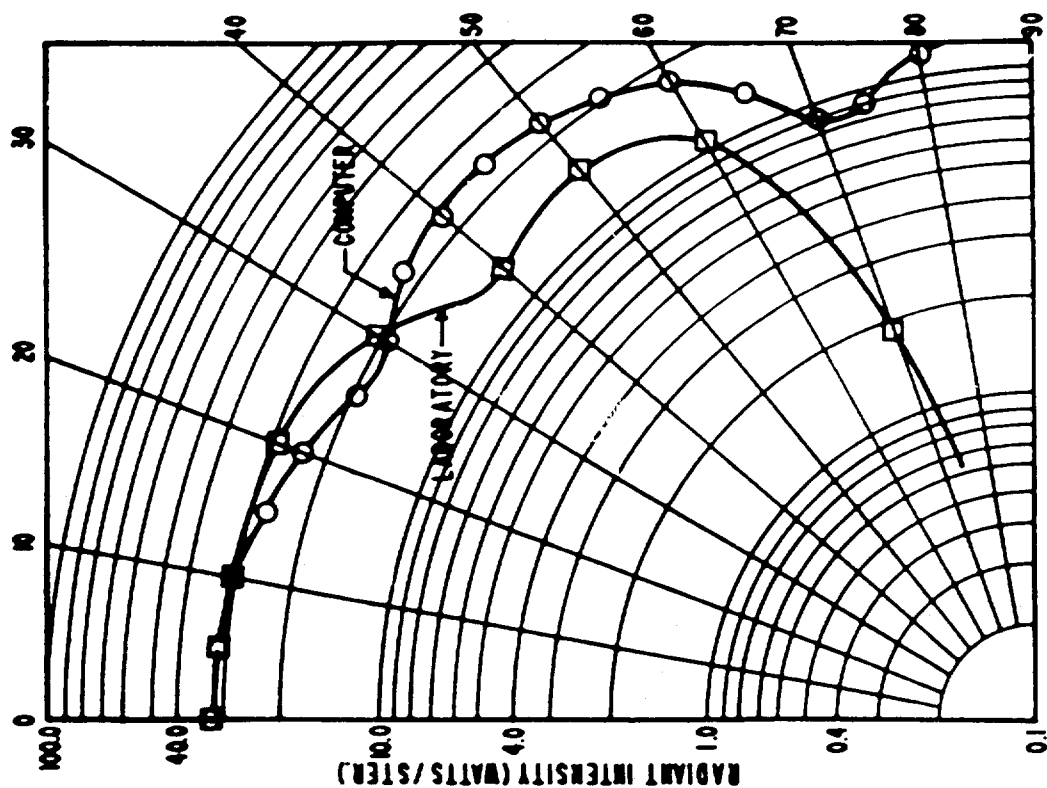


Figure 18. Gold Small Cone with Gold Innerbody

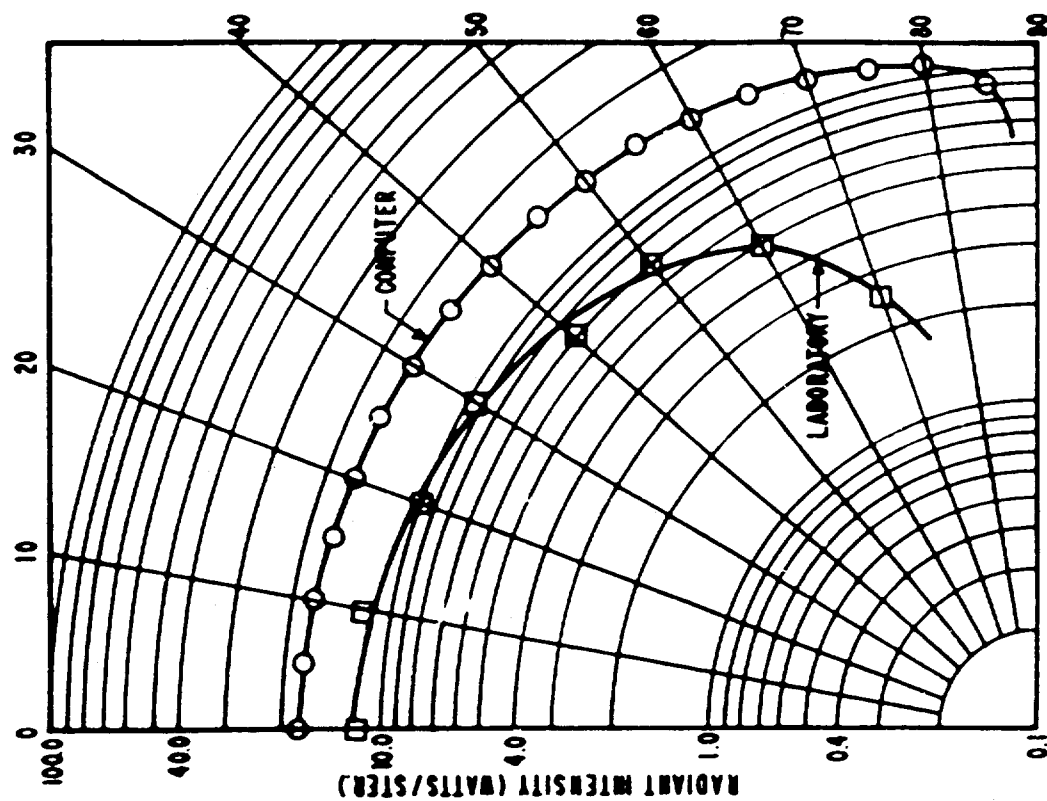


Figure 19. Gold Double Cone without Innerbody.

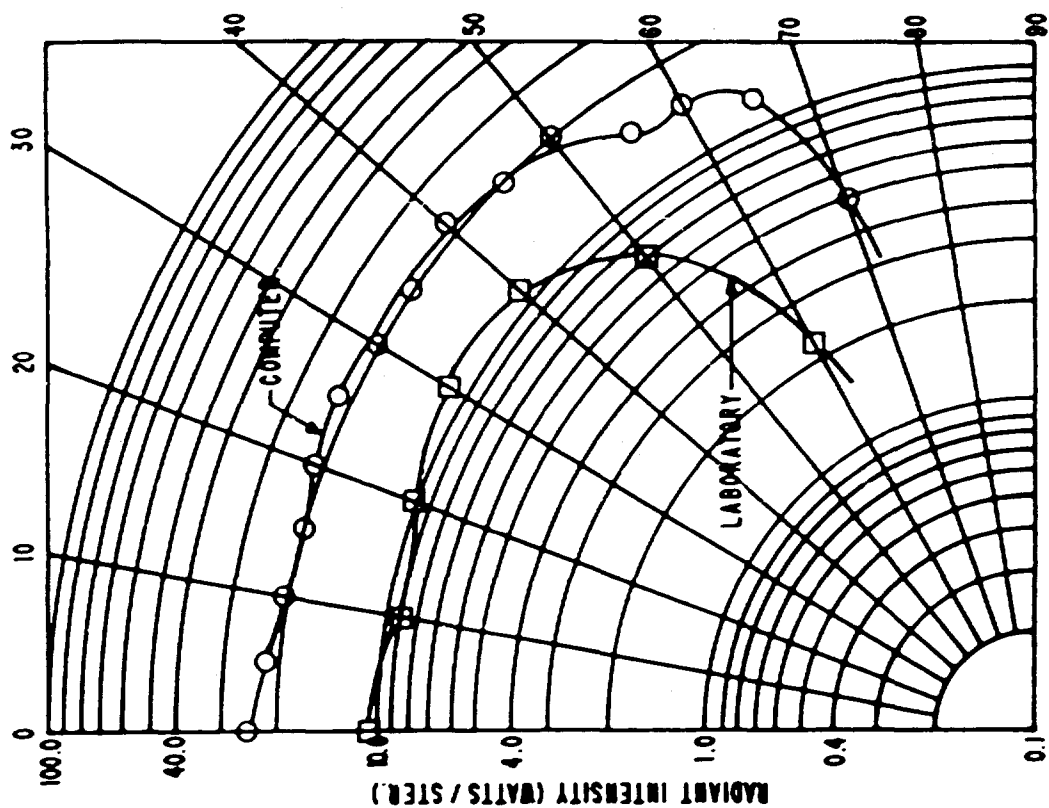


Figure 20. Gold Double Layer with Gold Innerbody.

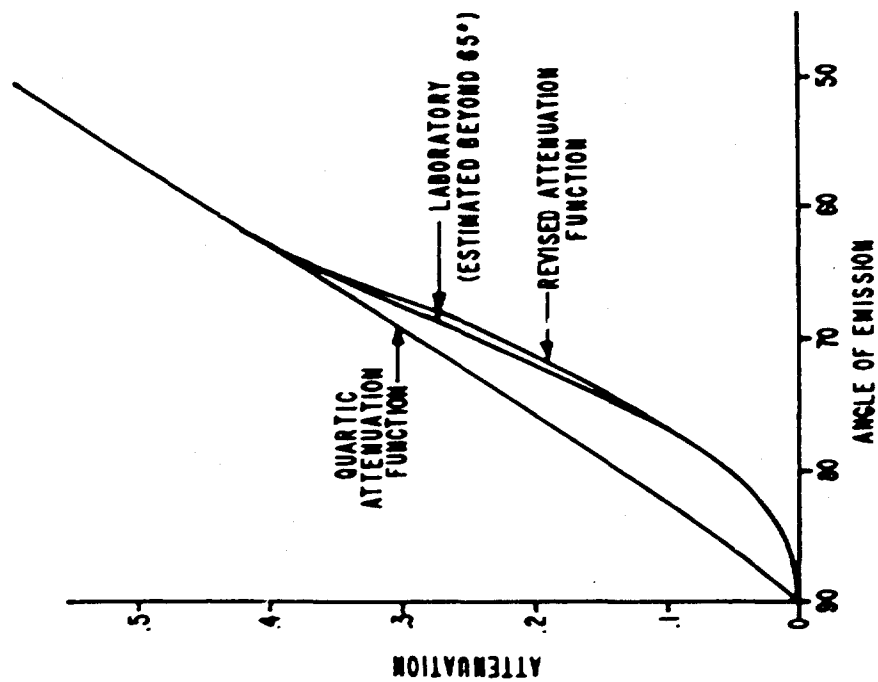


Figure 21. Revised Attenuation Function.

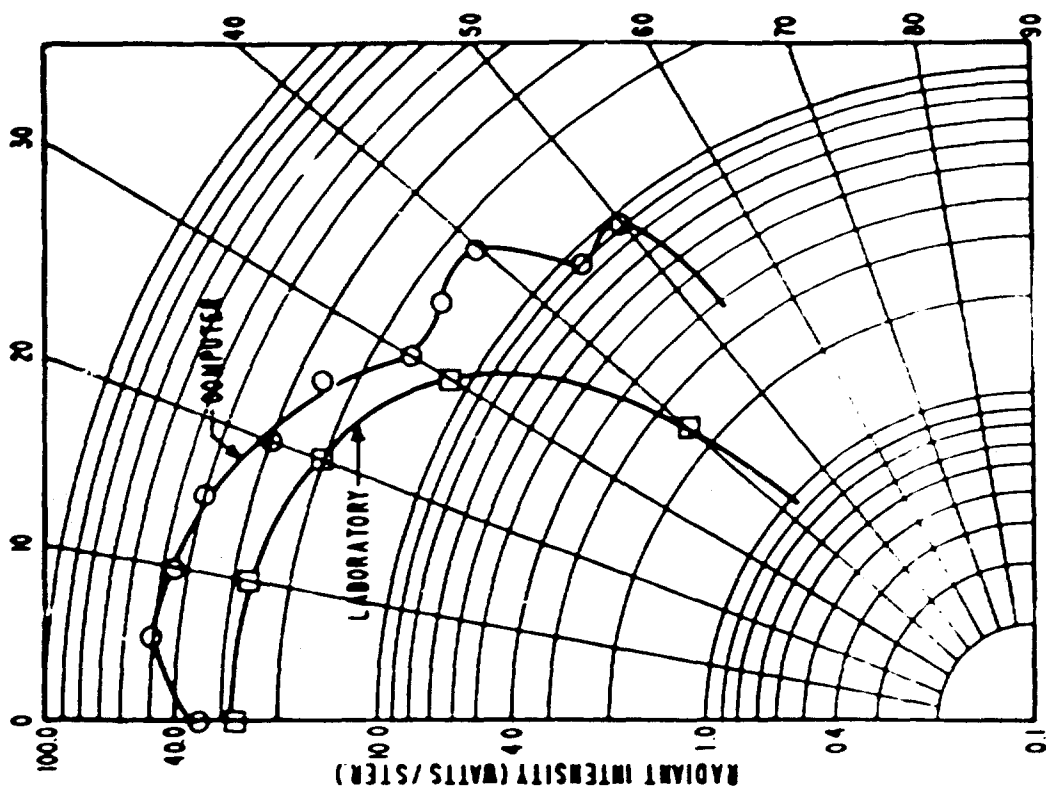


Figure 23. Gold Large Cone with Innerbody.

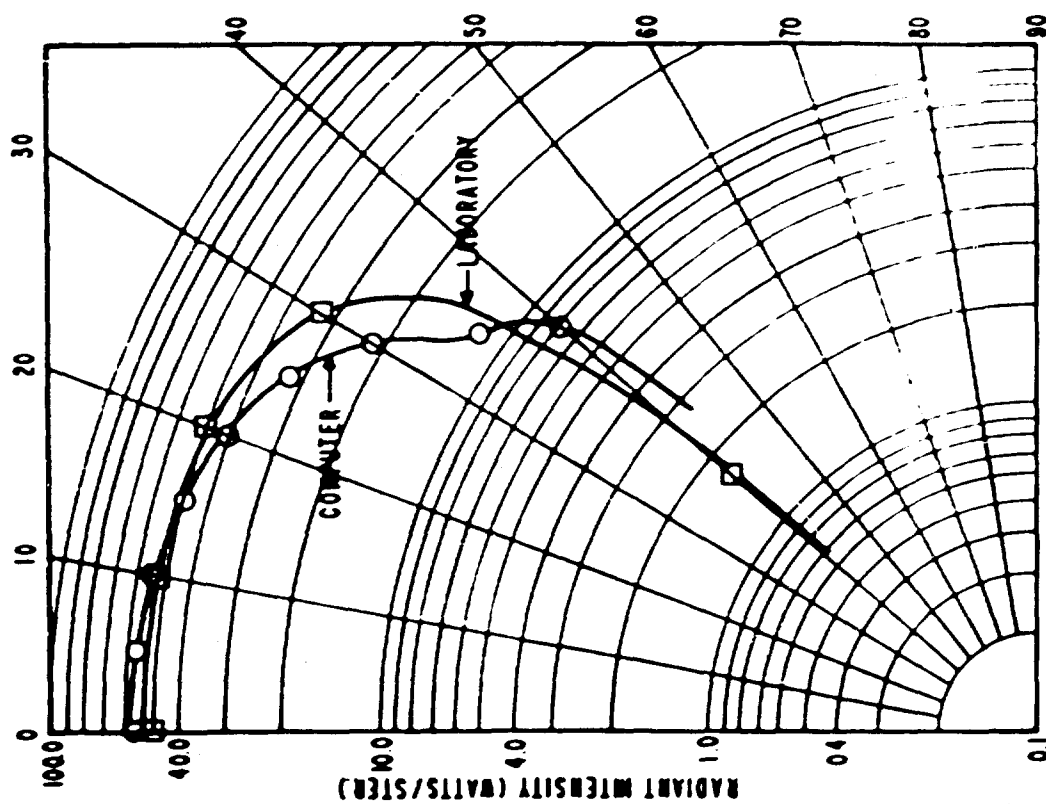


Figure 22. Gold Large Cone without Innerbody.

no laboratory counterparts. These configurations were the possible combinations of models and innerbodies having reflectivities of 0.1 and 0.4.

Figure 24 represents the configuration with both model and innerbody having reflectivities of 0.1. The solid curve connects all points, while the broken curve suggests an alternative plot which seeks to average out rapid fluctuations.

Curve B in Figure 25a represents the configuration in which the conical sections have a reflectivity of 0.1 and the innerbody has a reflectivity of 0.4. The broken line bears a strong resemblance to the broken line of Figure 24, suggesting that the reflectivity of the innerbody does not seriously affect the over-all radiation pattern. For curve C the reflectivities of model and innerbody were interchanged, and the curve shows a corresponding upward displacement. Finally, for Figure 25b all reflectivities are 0.4. Around to 50° this curve closely resembles curve C. The points around 70° are suspicious because only single rays traced. For all these four configurations, the total number of rays traced was small, and the curves reflect the expectedly wide scatter. The tabulated data of these runs is presented for reference in Table 4.

TABLE 4
RADIATION DISTRIBUTION DATA
ADDITIONAL DOUBLE CONE CONFIGURATIONS

| Configuration and Specifications | ϕ (degrees) | Average Radiant Intensity (watts/ster.) | No. of Rays |
|--|---------------------|---|-------------|
| Double Cone and Innerbody, "A" | 0 | .299860E-03 | 1 |
| | 5 | .126905E+01 | 4 |
| RIO .381819E-02 | 10 | .987272E+00 | 10 |
| PC 1.8125 | 15 | .149825E+01 | 18 |
| RM 2.3437 | 20 | .103791E+01 | 18 |
| RP 1.5625 | 25 | .453564E+00 | 34 |
| RB 1.75 | 30 | .267939E+00 | 27 |
| CB 2.9397 | 35 | .349939E+00 | 25 |
| CLEN 5.5 | 40 | .162114E+01 | 28 |
| ZM 2.9347 | 45 | .118030E+01 | 26 |
| REFC 1 .10 | 50 | .840194E+01 | 23 |
| REFC 2 .10 | 55 | .136106E-02 | 8 |
| REFB .10 | 60 | .157073E-01 | 4 |
| RAYS 232 | 65 | .106748E-01 | 2 |
| ALFA 1 .2598 | 70 | .207747E-01 | 1 |
| ALFA 2 -.2042 | 75 | .110112E-01 | 3 |
| Double Cone and Innerbody, "B" | 0 | .258076E+00 | 2 |
| | 5 | .149914E+01 | 5 |
| REFC 1 .10 | 10 | .133406E+01 | 8 |
| REFC 2 .10 | 15 | .151143E+01 | 17 |
| REFB .40 | 20 | .912819E+00 | 22 |
| | 25 | .774297E+00 | 13 |
| | 30 | .502498E+00 | 19 |
| | 35 | .504815E+00 | 16 |
| | 40 | .150352E+01 | 27 |
| | 45 | .930338E+00 | 27 |
| | 50 | .863313E+00 | 23 |
| | 55 | .381679E-01 | 12 |
| | 60 | .197174E-01 | 8 |
| | 65 | .330530E-01 | 3 |

TABLE 4 (CONT'D.)

RADIATION DISTRIBUTION DATA

ADDITIONAL DOUBLE CONE CONFIGURATIONS

| Configuration and Specifications | ϕ (degrees) | Average Radiant Intensity (watts/ster.) | No. of Rays |
|--|---------------------|---|-------------|
| Double Cone and Innerbody, "C" | 0 | .501221E-02 | 1 |
| | 5 | .601125E+01 | 5 |
| REFC 1 .40 | 10 | .278228E+01 | 9 |
| REFC 2 .40 | 15 | .542002E+01 | 17 |
| REFB .10 | 20 | .319370E+01 | 23 |
| | 25 | .296846E+01 | 20 |
| | 30 | .325373E+01 | 22 |
| | 35 | .274256E+01 | 27 |
| | 40 | .517727E+01 | 30 |
| | 45 | .337503E+01 | 23 |
| | 50 | .394718E+01 | 28 |
| | 55 | .414241E+00 | 15 |
| | 60 | .969764E-01 | 8 |
| | 65 | .163193E+00 | 5 |
| Double Cone and Innerbody, "D" | 0 | .320781E+00 | 1 |
| | 5 | .695572E+01 | 6 |
| REFC 1 .40 | 10 | .283313E+01 | 11 |
| REFC 2 .40 | 15 | .509215E+01 | 18 |
| REFB .40 | 20 | .414264E+01 | 22 |
| | 25 | .435535E+01 | 18 |
| | 30 | .372848E+01 | 25 |
| | 35 | .304150E+01 | 24 |
| | 40 | .492055E+01 | 24 |
| | 45 | .400914E+01 | 21 |
| | 50 | .407132E+01 | 26 |
| | 55 | .516437E+00 | 14 |
| | 60 | .353947E+00 | 11 |
| | 65 | .547787E+00 | 7 |
| | 70 | - | 0 |
| | 75 | .111103E+01 | 1 |
| | 80 | - | 0 |
| | 85 | .690870E-01 | 1 |
| | 90 | .106347E-01 | 1 |

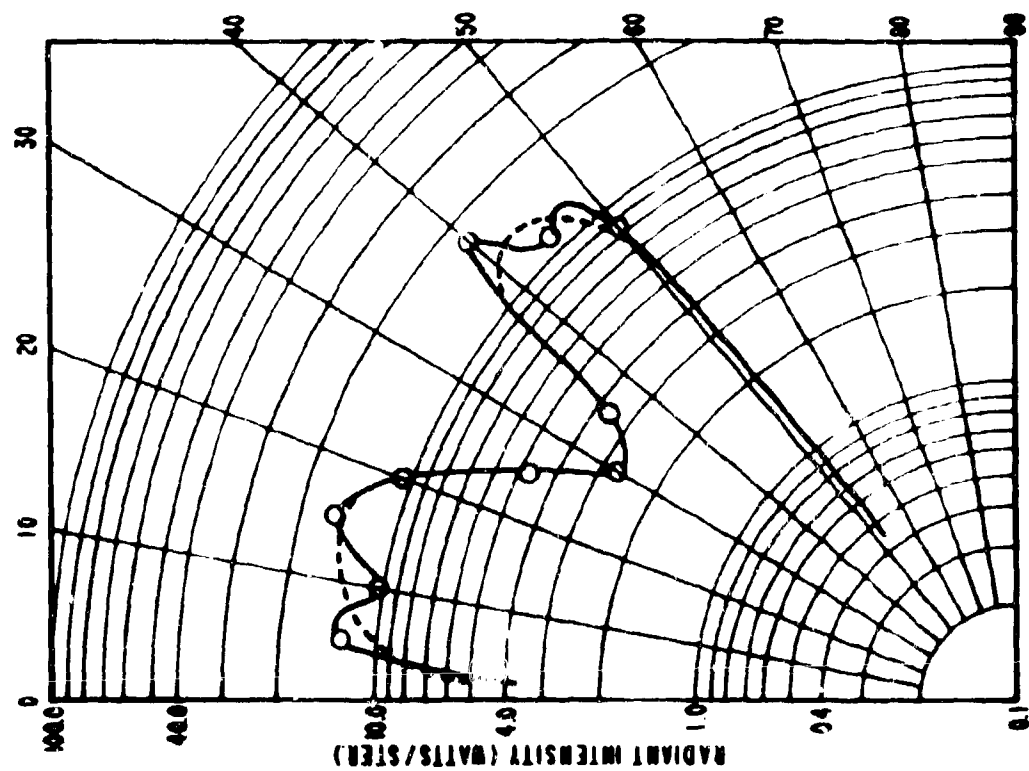


Figure 24. Double Cone with Innerbody, Curve A.

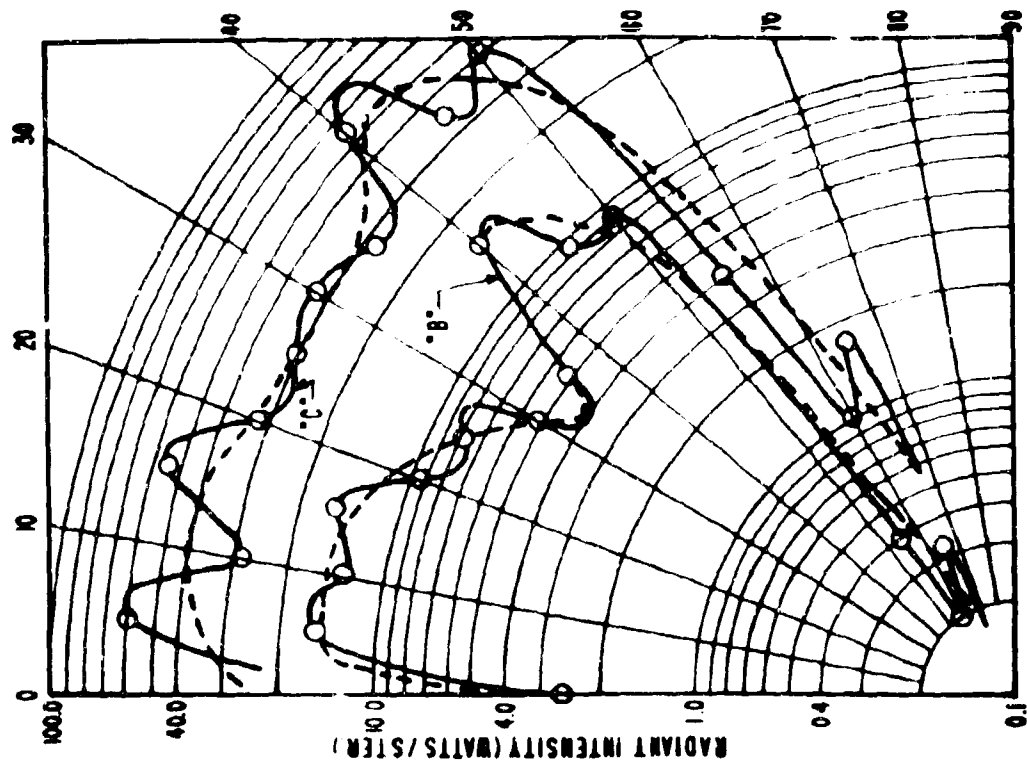


Figure 25a. Double Cone with Innerbody, Curves B and C.

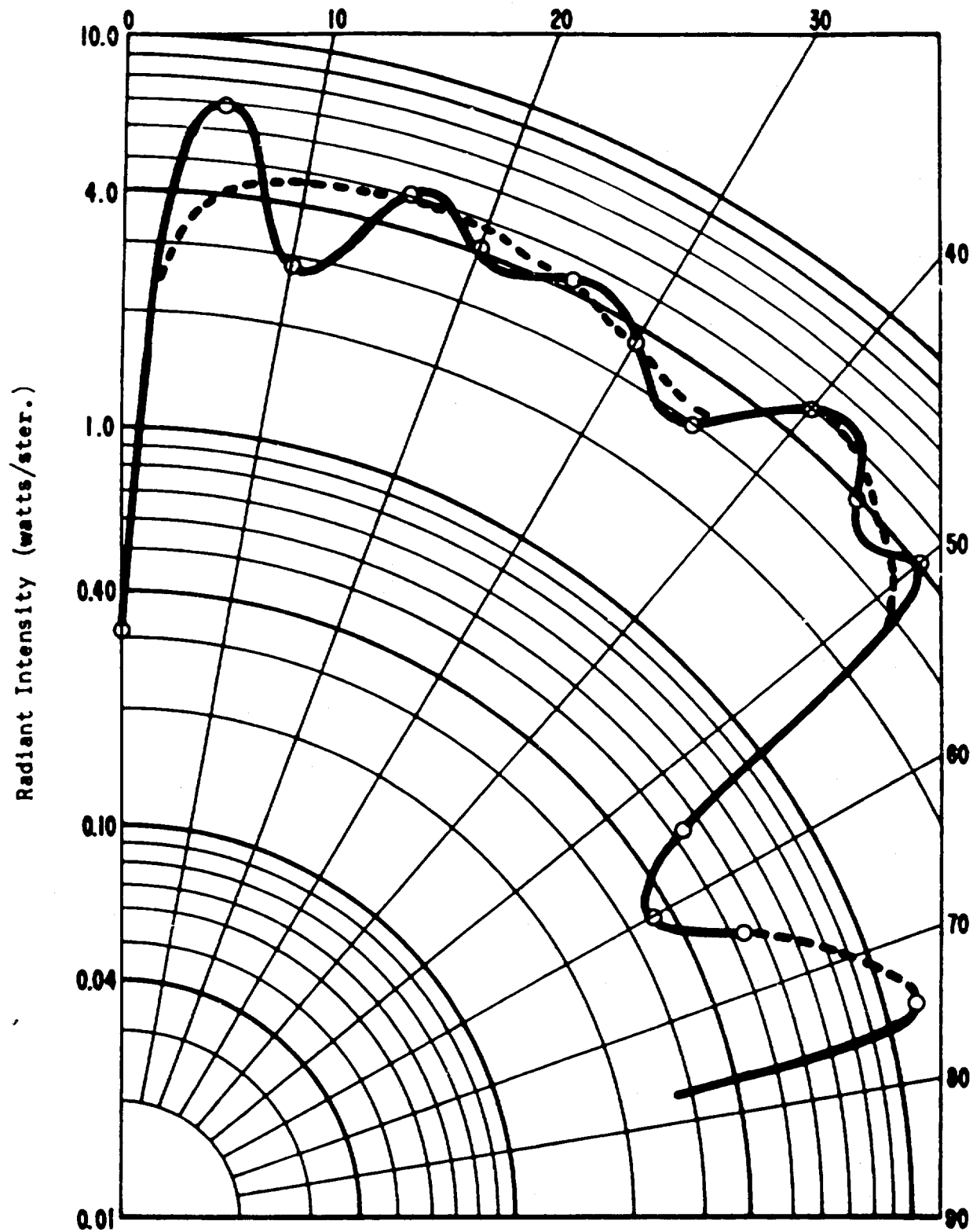


Figure 25b. Double Cone with Innerbody,
Curve D.

EVALUATION

This study was undertaken in an attempt to improve the prediction programs over their earlier counterparts. The programs were made as flexible as possible without sacrificing unduly their operating efficiency. The ray tracing was made to proceed from the base plane outward, since this paralleled the physical process. The random numbers used to locate origins of rays and to determine directions were taken from a table of uniformly random numbers, but only 2400 different numbers were used. The list was used repeatedly until the required number of rays were traced. A more advantageous arrangement would have employed a random number generator. This problem did not become significant until the runs were made on the 7094, at which time a suitable generator was not readily available.

Examination of the plots revealed that the programs yielded accurate predictions for some configurations, but failed to give completely satisfactory results for others. Most of the runs, however, fell somewhere in the broad region between these two extremes. In every case, there was at least a measure of qualitative agreement.

From the experience gained during the course of this study a number of areas of improvement have become apparent. The most urgent need is for a computer faster than the 1620. In many cases the discrepancies might be resolved by trying various combinations of parameters, such as the initial radiant intensity and the reflectivities. Another area deserving study is the treatment of reflections from surfaces which are neither purely diffuse nor purely specular. This may be a difficult problem and might require some experimental laboratory work to provide standards against which the empirical or theoretical models could be judged. There is still considerable work to be done on the development of a suitable correlation factor needed to compensate for fundamental differences between the physical processes and the simplified techniques of the computer programs.

In spite of the discrepancies still present in this development, there is strong evidence that this approach to the determination of radiant intensity patterns can be developed into a valuable design tool. The work accomplished so far has revealed the areas requiring more study, but more important, it has given a glimpse of the power of the tool. Design changes can be made and investigated in minutes or hours instead of the days or weeks that might be required to alter laboratory apparatus and reduce measurements data. The program is worth pursuing.

PART II

ANALYTICAL FORMULATION FOR EVALUATING INFRARED SHIELD CONFIGURATIONS

SUMMARY

An analytical approach has been developed for predicting directional radiant intensity from shielded infrared sources. In this approach, the geometrical and radiative characteristics of the shield and source are embodied in terms of the integral equations for radiative transfer. The solutions of these integral equations served as the basis for developing a prediction formula for diffuse and for specular surfaces.

The prediction formula was applied to diffuse configurations, both with and without a spherical innerbody, and the results were compared with laboratory measurements of a similar set of configurations. Qualitative agreement was found to exist for those configurations that were directly comparable.

INTRODUCTION

This part of the report is concerned with the development of an analytical foundation for prediction of radiant intensity patterns from shielded infrared sources. The analytical approach must be necessarily founded upon considerations of source and shield geometry and of the radiative properties of the surfaces. It is the object of this report to incorporate these basic considerations into a comprehensive theoretical framework from which the shielding effect of particular configurations and radiative characteristics can be derived.

It is pertinent to mention the generality with which the infrared shielding problem may be formulated. From the geometry aspect, it is desirable to have a theoretical formulation which will handle a wide range of source and shield configurations. On the other hand, among the radiative properties of the source and shield, the general formulation should account for the followings:

- (1) Surface distribution of radiant emittance or, equivalently, the surface temperature distribution.
- (2) Directional distribution of radiant emission; i.e., the relation, for an elementary unit area, of the radiant intensity in any direction to that in the normal direction.
- (3) Directional distribution of reflected radiant energy from an elementary unit area, accounting for the specular and diffuse components of the reflected energy.
- (4) Spectral distribution of emitted and reflected energy.
- (5) Emissivity and reflectivity of the source and shield materials.

The general formulation must also account for any enclosed attenuating media, which, while they are not properties of the enclosing surfaces, may have very pronounced effects on the energy transfer. Furthermore, the general framework should handle the interreflection of radiation within the source-shield configuration, and it should account for the presence of innerbodies. This ideal generalization is of more than academic value, for it serves as a standard against which any formulation must be compared. It will be shown that the foregoing generalizations of the problem can be achieved through use of an integral equation for radiant energy transfer. This implies that complicated radiant intensity prediction problems can be formulated and solved, in principle at least, in terms of and through the use of integral equations.

But there arises the logical question of to what extent can the different aspects of the problem be treated simultaneously in general terms. This is a question of great practical consequence because, for a given source-shield configuration, simplifying conditions or assumptions are usually required. For example, the condition, or assumption, of no atmospheric attenuation is usually taken for granted. Another frequently imposed condition is that of gray, diffusely emitting surfaces, i.e., surfaces whose emissivities are independent of wavelength and whose directional distribution of emitted energy is diffuse. It is possible to meet both these conditions to a fair extent over spectral bands within atmospheric windows, and both conditions are assumed in this report.

The next section presents the theoretical considerations used in formulating the shielding problem. The integral equation for radiant energy transfer is derived first in the most general terms and then is particularized to apply to configurations and boundary conditions imposed by the experimental work. Three basic shield configurations are considered; namely, (1) the cylinder, with and without a spherical innerbody, and (3) the concave, truncated double cone. Only perfectly diffuse and specular surfaces are considered. In the third section are presented graphical comparisons between the predicted and experimental radiant intensity patterns for diffuse shields. The effects of individual shield parameters are discussed, and suggestions for optimizing shield design are made.

THEORETICAL BASIS

DERIVATION OF INTEGRAL EQUATION

Arbitrary Enclosure

Integral equations have long been used in the analysis of radiant energy transfer in at least two different contexts, that of illuminating engineering and that of thermal radiant transfer. Though the use of integral equations in these fields is not new, their usage has not been very extensive. A derivation of the integral equation for radiant energy transfer is given here to illustrate the principle and to emphasize the inherent generality. The derivation follows along that given by Reference 1.

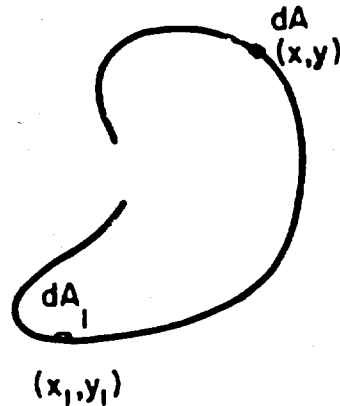


Figure 26. Arbitrary Radiating Enclosure.

Consider an arbitrary enclosure, as shown in Figure 26, and designate small area elements at two arbitrary points by dA_1 and dA . The positions of the two area elements are specified in terms of a coordinate system superimposed on the surface of the enclosure. Suppose that element dA_1 is held fixed at coordinates (x_1, y_1) and allow element dA to be located at the variable point (x, y) . Attention is now directed to the fixed point (x_1, y_1) and the area element dA_1 , at which a radiant energy balance will be set up. The total radiant energy leaving dA_1 has two components. The first is the directly emitted energy, which in the absence of interreflected radiation is called the emittance $w_0(x_1, y_1)$ at dA_1 . The second component is the reflected portion of the irradiation $H(x_1, y_1)$ of dA_1 , which is given by $\rho(x_1, y_1) H(x_1, y_1)$, where $\rho(x_1, y_1)$ is the reflectivity of the enclosure surface at (x_1, y_1) . Hence, the radiant energy balance at dA_1 may be expressed by

$$W(x_1, y_1) = w_0(x_1, y_1) + \rho(x_1, y_1) H(x_1, y_1), \quad (3)$$

where $W(x_1, y_1)$, the apparent emittance at dA_1 , and $H(x_1, y_1)$ are both unknowns. The term $H(x_1, y_1)$ can be formally eliminated by considering the source of irradiation of dA_1 . Thus, consider now the element dA at any other point (x, y) . If the total radiant energy leaving dA is $W(x, y)$, then the amount reaching dA_1 is equal to

$$dH(x_1, y_1) = W(x, y) K(x, y; x_1, y_1) dA, \quad (4)$$

where $K(x, y; x_1, y_1)$ is equal to the irradiation at dA_1 caused by unit (apparent) emittance from unit area at point (x, y) . The total irradiation of dA_1 is obtained by integrating the contributions from all the surface elements which are visible from dA_1 . Thus it follows that Eq. (3) can be restated in terms of a single unknown function as follows:

$$W(x_1, y_1) = W_0(x_1, y_1) + \rho(x_1, y_1) \int_{A, \text{visible}} W(x, y) K(x, y; x_1, y_1) dA. \quad (5)$$

Since the unknown function W appears also under the integral sign, Eq. (5) is an integral equation.

Equation (5), which may be called the integral equation for radiant energy transfer, applies to an arbitrary enclosure shape and to arbitrary surface radiative properties. That this is true is seen from the meaning of Eq. (4), for it contains no assumptions at all on the geometry nor on the nature of the radiating surface element dA . It merely relates the total energy $W(x, y)$ leaving dA in all directions to that fraction of $W(x, y)$ which impinges upon dA_1 , all other circumstances of the transfer being contained in the function K . Concisely, the function K contains the effects of geometry, of the directional, and spectral, distributions of the emitted and reflected radiation, and of any attenuating media. Thus in the present formulation a major problem revolves around the specification of the function K , which is called the kernel of the integral equation. A more thorough description of the kernel is given in a later section.

Cone With Spherical Innerbody

However, before considering the explicit nature of the kernel, it is necessary to adapt the generalized integral equation to a particular geometry. For this purpose, an example will be made of a conical tube with a spherical innerbody located on the longitudinal axis, as shown in Figure 44 (Appendix A). Imagine the cone and sphere to be divided into infinitesimal rings, or bands, transverse to the longitudinal axis of symmetry.

Now consider the radiant energy balance at any point (x, β_1) on the conical band element specified by the position variable x . The variable x is measured along the axis of the cone-sphere system, and azimuthal angles β are measured from the upper x - z plane. The elementary area at point (x, β_1) is termed a "point" element, which is given by

$$dA_1 = r(x) d\beta_1 dx \sec \theta,$$

where $r(x)$ is the radius of the cone at x , β_1 is the azimuthal angle of dA_1 , and θ is the cone angle. The energy balance at dA_1 will obviously involve radiation from the visible portion of the sphere as well as from the remaining unobscured portion of the cone itself. At the same time, the energy balance at point element dA_3 on any spherical ring will involve radiation from the unobscured portion of the cone as seen from dA_3 . The point element dA_3 , on a spherical ring specified by polar angle γ , is given by

$$dA_3 = R^2 \sin \gamma d\gamma d\beta_3,$$

where R is the radius of the sphere and β_3 is the azimuthal angle of dA_3 . Therefore, the total energy leaving a point element such as dA_1 is composed of two parts, the first being the intrinsic thermal emittance $W_{01}(x, \beta_1)$ at the point. The second part is the reflected portion of the energy received from elementary ring elements of the cone and sphere as seen from dA_1 . Analogous statements can be made for the spherical point element.

Before it is possible to put the energy balance equation into useful mathematical form, it is necessary to specify the obscuration caused by the innerbody. For axial symmetry, the obscuration caused by a spherical innerbody within a truncated cone, closed at one end, is analyzed in Appendix A. The main feature of this analysis is that the obscuration effect is accounted for on each infinitesimal ring element.

Because of the axial symmetry, it is possible to express, for example, the radiant flux from a partially obscured conical ring to a conical point element as a fraction of the flux from the complete ring. The fraction varies from ring to ring and of course changes for any given ring when the observation point is translated. As shown in Appendix A, these facts are embodied in a function $\tau(x, \xi)$, where x is a position of the observation point and ξ is a position variable also along the axis of the cone. The function $\tau(x, \xi)$ is bounded by zero and unity, the zero value corresponding to total obscuration and the unity value to none. On the other hand, the azimuthal angular limits of obscuration for each spherical ring must

be determined for each and every observation point dA_1 on the cone. Similar limits must be found for the conical rings when the viewing point is taken on the sphere. Appendix A also treats the obscuration of the end disk, which is introduced later below.

With the obscuration specified according to Appendix A, attention is turned again to the energy balance equations. It is important first to point out that sets of simultaneous integral equations can be derived on the basis of the energy balance for the ring to point element interchange. This consideration is necessary when axial symmetry does not exist or when the emittance is not uniform around the ring element, i.e., when it is a function of the azimuthal angle θ . For the cone-sphere system under consideration, the ring emittance is assumed to be independent of θ . Hence, the energy balance equation at point element dA_1 with a conical band at ξ and a spherical ring at γ' can be written as

$$W_1(x) = W_{01}(x) + \rho_1 W_1(\xi) \tau(x, \xi) k_{11}(x, \xi) da_1 + \rho_1 W_3(\gamma') k_{31, v}(x, \gamma') da_3 \quad (6a)$$

where $da_1 = 2\pi\xi d\xi$ is the area of the conical band at point ξ and $da_3 = 2\pi R^2 \sin\gamma' d\gamma'$ is the area of the spherical ring at γ' . The analogous equation applying at the spherical point element dA_3 is given by

$$W_3(\gamma) = W_{03}(\gamma) + \rho_3 W_1(\xi) k_{13, v}(\gamma, \xi) da_1, \quad (6b)$$

where in both equations the symbol v on the kernel indicates that only the visible portion of the ring is considered. The total energy $W_1'(x)$ at dA_1 follows from Eq. (6a) by integrating ξ over the length of the cone and γ' over the visible segment of the sphere, while the total energy $W_3'(\gamma)$ at dA_3 follows from integrating ξ over the visible portion of the cone. Thus the following equations for ring-to-point interchange result:

$$W_1'(x) = W_{01}(x) + \rho_1 \left[\int_0^R W_1'(\xi) \tau(x, \xi) k_{11} da_1 + \int_{\gamma_1(x)}^{\gamma_2(x)} W_3'(\gamma') k_{31, v} da_3 \right] \quad (7a)$$

$$W_3'(\gamma) = W_{03}(\gamma) + \rho_3 \int_{\xi_1(\gamma)}^{\xi_2(\gamma)} W_1'(\xi) k_{13, v} da_1,$$

where the functional notation has been momentarily suppressed in the k functions. (Subscript 1 denotes the cone while subscript 3 denotes the sphere).

Up to this point, attention has been concentrated on the energy balance at only point elements. With the symmetry and conditions described above, it is really more convenient to consider the receiving area element to be a ring. The energy balance equations will not be changed in form, since the energy received by a uniform ring element is just a constant multiple of that received by one of its constituent point elements. Therefore, on the basis of ring-to-ring interchange, Eq. (7a) takes the following form:

$$\begin{aligned}
 W_1(x) = W_{01}(x) + \rho_1 \left[\int_0^2 W_1(\xi) \tau(x, \xi) K_{11}(x, \xi) d\xi \right. \\
 \left. + \int_{\alpha_1(x)}^{\alpha_2(x)} W_3(\gamma') K_{31,v}(x, \gamma') d\gamma' \right] \quad (7b) \\
 W_3(\gamma) = W_{03}(\gamma) + \rho_3 \int_{\xi_1(\gamma)}^{\xi_2(\gamma)} W_1(\xi) K_{13,v}(\gamma, \xi) d\xi,
 \end{aligned}$$

where, for convenience, the parameters of the differential ring elements, except the differential, have been combined into the related k function. This new set of kernels is denoted by the symbol K . Equation (7b) is the desired adaptation of the generalized form, Eq. (5), with two integral equations being necessary to describe the conical tube-sphere configuration.

This special case has been considered for both concreteness and simplicity in order to illustrate the underlying principles. The same principles and approach are applicable to all configuration, the end result being that an integral equation is required for each separate surface of the enclosure. As yet, the only assumption is that each ring element must have uniform apparent emittance around its periphery, but nothing has been assumed about the directional distribution of the energy leaving the ring element. For reference in this context, and for completeness, the system of integral equations which obtain when a radiating disk source (denoted by subscript 2) is used to close one end of the cone is presented here:

$$w_1(x) = w_{01}(x) + \rho_1 \left[\int_0^a w_1(\xi) \tau(x, \xi) K_{11}(x, \xi) d\xi + \int_0^a w_2(\rho) \tau(x, \rho) K_{21}(x, \rho) d\rho + \int_{\alpha_1(x)}^{\alpha_2(x)} w_3(\gamma') K_{31,v}(x, \gamma') d\gamma' \right] \quad (8a)$$

$$w_2(r') = w_{02}(r') + \rho_2 \left[\int_0^1 w_1(\xi) \tau(r', \xi) K_{12}(r', \xi) d\xi + \int_{\alpha_1(r')}^{\alpha_2(r')} w_3(\gamma') K_{32,v}(r', \gamma') d\gamma' \right] \quad (8b)$$

$$w_3(\gamma) = w_{03}(\gamma) + \rho_3 \left[\int_0^1 w_1(\xi) K_{13,v}(\gamma, \xi) d\xi + \int_0^a w_2(\rho) K_{23,v}(\gamma, \rho) d\rho \right] \quad (8c)$$

where ρ and r' are radii of elementary plane annuli on the disk and a is the radius of the disk. The functions $\tau(r', \xi)$ and $\tau(x, \rho)$ relating to obscuration of the end disk and the angular limits, α_1 and α_2 , of obscuration pertaining to the sphere itself are given in Appendix A.

INTERPRETATION OF THE KERNEL

The physical content of the kernel K was mentioned briefly, earlier. Attention is now directed to the inherent significance of the kernels and to establishing a more thorough physical interpretation of them. A limited discussion of the mathematical nature of the kernel and its relation to the solution of the integral equation is also included in this section.

Physical Interpretation

It has been pointed out that the kernel* of the integral equation represents a major portion of the physical effects of the radiating enclosure.

* It should also be pointed out that the kernel as used here has been called variously the angle factor, the configuration factor, or the shape factor. However, these names often relate only to the geometrical nature of the problem.

Though it is not difficult in concept to include atmospheric attenuation in a physical interpretation of the kernel, the mathematical details become exceedingly complex. The inclusion of an absorbing medium has been treated for a few simple geometries (Reference 2) but for the remainder of this report the effects of attenuating media will not be considered. Therefore, the formulation will be limited to "in vacuo" conditions, leaving for consideration the effects of the radiative surface properties and geometry.

A quite significant characteristic of a radiating surface element is the distribution in space of the energy leaving the element. The directional distribution must be considered in specifying the kernel for radiant interchange between different surface elements. For an elementary plane area, the distribution function may be expressed as the ratio (Reference 3) of radiance $N(\alpha)$ in the direction making an angle α with the normal direction to the radiance N_0 in the normal direction, or as the ratio (Reference 4) of directional emissivity to hemispherical emissivity. The first ratio is just

$$D(\alpha) = N(\alpha)/N_0.$$

The radiance N_0 is considered to be a mean value given by $N_0 = W/\pi$, where W is the radiant emittance of the surface element. The distribution function may range in form from Lambert's cosine law for perfectly diffuse surfaces to that for highly directional emission. Lambert's Law, namely,

$$N(\alpha) = N_0 \cos \alpha,$$

is frequently assumed for the emitted radiation.

For a cavity surface element, the directional distribution may be extended to include the energy reflected from the surface element, since the component of reflected energy combines with that directly emitted in a given direction to form an effective total intensity in that direction. The reflective properties of the surface element determine in part the directional distribution of the energy leaving the surface element. For example, a diffusely emitting surface may be a specular reflector; or it can be a diffuse reflector, requiring in the first case a highly polished surface and in the second a dull, matte finish. In the second case, the resultant distribution would remain Lambertian, whereas any other combination would, strictly speaking, result in a non-Lambertian distribution.

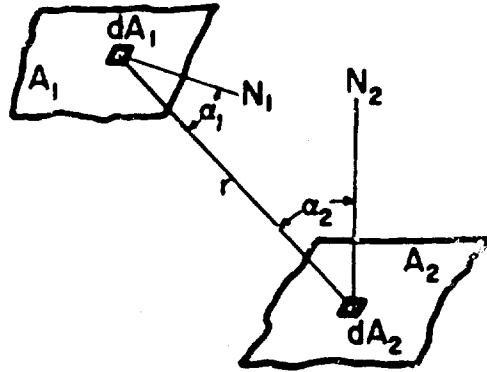


Figure 27. Arbitrary Plane Elements.

Following the lines of Reference 3, the explicit geometrical character of the kernel will be demonstrated. For this purpose consider Figure 27, which shows the geometrical relation between two elementary areas dA_1 and dA_2 separated by a distance r . Let α_1 be the angle formed by the normal direction to dA_1 and the connecting line r between dA_1 and dA_2 , and let dw_1 be the solid angle subtended by dA_2 . Then, that energy from dA_1 which impinges on dA_2 is

$$dE_{12} = N(\alpha_1) dw_1 dA_1 \quad (9a)$$

whereas the total energy from dA_1 into the entire hemisphere is

$$dE = w_1 dA_1 = \pi N_0 dA_1. \quad (9b)$$

Hence, by definition, the kernel K_{12} is given by

$$K_{12} = \frac{dE_{12}}{dE} = \frac{N(\alpha_1) dw_1}{N_0}. \quad (10a)$$

Since the solid angle dw_1 is given by

$$dw_1 = \frac{dA_2 \cos \alpha_2}{r^2},$$

Equation (10a) can be expressed as

$$K_{12} = \frac{N(\alpha_1) dA_2 \cos \alpha_2}{\pi N_0 r^2} . \quad (10b)$$

Equation (10b) represents the kernel for an unspecified distribution function $N(\alpha)/N_0$.

Equation (10b) can be put into the following form:

$$dA_1 K_{12} = \frac{D_1(\alpha_1) \cos \alpha_1 \cos \alpha_2 dA_1 dA_2}{\pi r^2} . \quad (11a)$$

When the roles of dA_1 and dA_2 are reversed in the foregoing derivation, i.e., by considering dA_2 to be the emitting surface instead of the receiver, an equation analogous to Eq. (11a) is obtained, i.e.,

$$dA_2 K_{21} = \frac{D_2(\alpha_2) \cos \alpha_1 \cos \alpha_2 dA_1 dA_2}{\pi r^2} . \quad (11b)$$

Equations (11a) and (11b), holding for any directional distribution of the corresponding point source elements, also clearly demonstrate the geometrical dependence of kernels K_{12} and K_{21} .

It is clear that if the distribution functions $D_1(\alpha_1)$ and $D_2(\alpha_2)$ are equal, then equality obtains between Eqs. (11a) and (11b), i.e.,

$$dA_1 K_{12} = dA_2 K_{21} . \quad (12)$$

The relation expressed by Eq. (12) is called the reciprocity theorem. Reciprocity of the radiant interchange between two area elements thus requires identical directional distribution at each element. The equality of $D(\alpha_1)$ and $D(\alpha_2)$ is assured when the two elements are Lambertian, for then $D(\alpha)$ becomes equal to unity and, hence, independent of α . The assumption of the reciprocity theorem leads to a very useful simplification, since it effectively reduces by one-half the number of required kernels and subsequent computational efforts.

The kernel for radiant interchange between two surface elements can be derived analytically by two methods. The first (References 3 and 5), and

fundamental, technique is integration of Eqs. (11a) or (11b) over the appropriate area elements; the second (References 3, 5, 6, 7, 8) makes use of algebraic operations and the reciprocity relation to derive required kernels from those already existing.* These techniques have been applied to the diffuse shield configuration considered in this report; the results are compiled in Appendix B.

Mathematical Classification

Each of the kernels presented in Appendix B is a function of the positions of two differential area elements, each of which is specified by a single coordinate. Always one point is fixed while the other varies over an open interval. The functional behavior of the kernel $K(x,y)$ is of major importance in the formal theory of integral equations. Without pretense of more than just cursory mention, some of the mathematical characteristics of the kernel are listed here. The kernel $K(x,y)$ is required to be real but not identically zero on the interval of interest. Theory permits that both $K(x,y)$ and the yet unknown function $W(x)$ may be discontinuous functions, provided they are of integrable square. Two important classifications exist which depend on the functional form of the kernel. First, the kernel is of the separable type when $K(x,y)=h(x)g(y)$, or a sum of such products, and the second type is the symmetric kernel, i.e., when $K(x,y)=K(y,x)$. Their consequence in relation to the solution of the integral equation is pointed out in the next section. For the symmetric kernel, a rather complete description of mathematical theorems and details and their relation to interreflecting enclosures has been presented in Reference 9.

SOLUTION OF THE INTEGRAL-EQUATION SYSTEM

The approach for solving the integral-equation system is determined by the nature of the kernel involved. In turn, the kernel is directly dependent on the symmetry of the shield configuration. An approximate analytical solution is possible for the cylindrical shield, under certain conditions, while a direct numerical solution must be obtained for the other configurations considered in this report. The conditions under which (approximate) analytical solutions obtain are presented below, followed by a description of the numerical method of solution.

* The references cited here on this subject are intended to be representative rather than exhaustive. Reference 6 gives a review of definitions and methods for deriving kernels (or angle factors).

Analytical and Approximate Analytical Methods

If the shield itself is sufficiently symmetrical, then the corresponding kernel is symmetric. For a surface of revolution, at least three axes of symmetry are required to assure a symmetric kernel. The Hilbert-Schmidt method (see Reference 10, for example) applies to the case of a symmetric kernel, allowing in principle closed-form solutions. But even symmetric kernels lead to integrals which are not readily integrated. Such cases are the rule, and it becomes necessary to replace the true kernel with a simpler analytic approximation. The usual stipulation on the form of the approximate kernel is that it be separable. The condition of separability results in simpler integrals which can then be integrated to give an approximate solution.

It has been found (Reference 11) that rather simple approximate kernels give satisfactory results for a cylindrical enclosure. The approximate kernels are in the form of a two- or three-term exponential function. Even a one-term exponential has been found by Moon (Reference 12) to be satisfactory for illumination calculations. Moon's solution is based on the assumption that the initial and final emittances are uniform over the end disk. His solution was applied to the cylinder in the present case, and the result is compared with a numerical solution in the next section.

The foregoing discussion points to the fact that even approximate analytic solutions seem possible for only highly symmetrical shield configurations. Such analytic solutions, however, possess the inherent advantage and generality of closed form, in which the effects of the separate parameters of the shield can be examined with ease; but the results are approximate because the true kernel has been replaced by an approximation. For a wider class of less symmetrical shields, the approach must be along the lines of numerical solutions.

Numerical Solution

Direct numerical solutions have one distinct disadvantage in that they have no generality of form and must be worked out again for each combination of parameters. In effect, however, this disadvantage can be made almost negligible through the use of high-speed electronic computers. In addition, numerical solutions can be achieved for a precise and complete formulation of the physical processes within the shield without resort to approximate kernels. This fact is especially important when a system of integral equations, such as Eq. (8), is required, for then approximate analytical solutions would be difficult, if possible at all. This state of affairs may be summarized as follows: Approximate numerical solutions are more readily obtained for a complete, analytical formulation of the shield problem than are analytical solutions for an approximate formulation.

The numerical solution technique that was used in the present work is now described. Similar and other methods of solution have been described in the literature in relation to other problems involving diffuse (References 7 and 8) and specular (References 13 and 14) enclosures. The method of solution used herein is an iteration technique, which applies to either diffuse or specular shields. Then, considering Eq. (8), the solution procedure is outlined as follows: First, the physical problem was specified, for any given geometrical configuration, by assigning appropriate values to the radiative parameters, i.e., to the reflectivities and the initial emittances. Next, initial trial solutions -- designated by $W_1(\xi;1)$ and $W_3(\gamma;1)$ -- were guessed for the unknown functions $W_1(\xi)$ and $W_3(\gamma')$, respectively, in Eq. (8b). Ultimately, each initial trial function took the form of a finite sequence of numbers dependent on the corresponding position variable ξ or γ' ; and each was introduced as such into the corresponding integral of Eq. (8b). A trial distribution was then obtained for $W_2(r')$ by numerically evaluating the right-hand side of Eq. (8b) for each value of r' , the end disk being divided into a finite number of evenly spaced radial increments. Let $W_2(r';1)$ be the solution thus obtained. Then the new function $W_2(r';1)$ and initial guessed function $W_1(\xi;1)$ were applied in Eq. (8c), and in a similar fashion a new distribution $W_3(\gamma;2)$ was generated for the sphere. Both $W_3(\gamma;2)$ and $W_2(r';1)$ were then substituted in Eq. (8a), and the right-hand side was numerically evaluated for each value of x , giving a second trial distribution $W_1(x;2)$ applying to the conical walls.

Starting again with $W_1(\xi;2)$ and $W_3(\gamma';2)$ in Eq. (8b), the entire process was repeated.

The foregoing procedure was iterated until convergence was achieved on all three functions. The convergence criterion was set as a specified difference between the values of the function on the n th and $(n-1)$ st iteration. In this fashion, any desired degree of accuracy may be acquired.

Obviously, when the innerbody is absent, obscuration effects are absent, and the computational effort is considerably reduced. When consideration of the innerbody is eliminated, Eq. (8) reduces to two integral equations, which are also solved by the iteration method.

PREDICTION OF DIRECTIONAL RADIANT INTENSITY PATTERNS

Up to this point, attention has been concentrated on the physical occurrences within the radiating enclosure. This has been necessary to provide a general framework within which the prediction of radiant intensity directional patterns in space can be formulated for a wide range of conditions. It is possible to develop simpler prediction schemes without the complications of integral equations if, for example, interreflected radiation is assumed to be unimportant; or if the distribution of emittance over

all surfaces of the enclosure remains uniform in the presence of diffuse reflection (Reference 15). A simpler formulation is desirable if the actual physical problem permits it. However, for many practical cases, such simplifying assumptions are not justified, requiring a more thorough, though more complicated, description.

Attention is now turned to the role played by the solutions of the integral equation system in formulating the prediction problem. As will be shown, the approach to the prediction formulation depends heavily on the nature of the shield surface; and three distinctions are readily made according to whether the surface is diffuse, specular, or intermediately non-Lambertian between these two extremes.

Role of Integral-Equation System Solution

The solutions of the integral-equation system pertaining to a shielded source are not themselves solutions to the directional intensity prediction problem. They are necessary intermediate steps in a general treatment, however. It will be iterated that, physically, the solutions of the integral-equation system represent the distribution of apparent emittance over the surfaces of the shield-source enclosure. The emittance distribution function thus obtained contains the increase caused by interreflected energy above the intrinsic emittance of a surface element at the existing temperature. Also, the apparent emittance distribution can contain the effects of temperature gradients. For shields which are surfaces of revolution, the integral equation approach readily handles temperature gradients along the longitudinal axis of symmetry, i.e., the temperature varying from ring to ring but remaining constant around the circumference of each ring element. An asymmetrical temperature distribution could be handled, but with more difficulty.

The apparent emittance distribution is therefore quite important, for it specifies the total amount of radiant energy leaving each surface element of the shield-source enclosure. The apparent emittance of an elementary unit area gives the total energy transferred therefrom into a hemisphere and thus does not regard the directional distribution of the energy. However, it should be noted again that if the total energy leaving the unit area remains diffuse, then its directional distribution will be given by Lambert's cosine law. Such is not the case for specular and other non-Lambertian surfaces. Whatever the case, the apparent emittance distribution serves as the starting point for the prediction formulations, which are now considered.

Formulations for the Diffuse Shield-Source Enclosure

Strictly speaking, the geometry and solid angle of the detector optical system relative to the shield aperture are important factors to be

considered in deriving an intensity prediction theory. This is especially pertinent for detector-source separation distances such that the field of view of the detector optical system is less than the aperture of the shield (Reference 16). The following formulation assumes that the shield aperture is less than the field of view of the detector and that the collection optics receives an essentially non-divergent beam of radiation.

It is well known that the radiant intensity J_0 in the direction normal to a uniform diffuse source is simply related to the emittance by

$$J_0 = (1/\pi) WA,$$

where A is the area of the source. If the emittance W were a function of position on the source, then an integration of W over the source would be required for the radiant intensity, i.e.,

$$J_0 = \frac{1}{\pi} \int_A W(x,y) dA.$$

The directional distribution of radiant intensity $J(\phi)$ for this source would follow by integrating the non-uniform emittance over the projected area of the source as seen from an aspect angle ϕ , treating the projected area as a non-uniform plane source. An application of this idea was made on the diffuse cylinder without an innerbody under the assumption that the apparent emittance over the source disk remained uniform. However, this method was difficult to apply to other shield configurations; its application to the cylinder will be described later. But first a formulation applicable to all the shield geometries will be described.

Consider a diffuse conical shield with diffuse spherical innerbody and a diffuse circular source which forms the closed end of the shield-source enclosure. The distribution of apparent emittance over each of the three surfaces is given by solving Eq. (8). Generally, the apparent emittance distribution on each surface will be non-uniform. The confronting problem is to integrate these three non-uniform distributions over the visible portions of the corresponding surfaces as seen from different aspect angles. (See Figure 28.)

An integration in closed form is impossible, if for no other reason than the fact that the apparent emittance distribution functions are not in closed form. Hence, a finite summation process must be used. To facilitate the summation, the projected area defined by the shield aperture at

the desired aspect angle ϕ is considered to be a non-uniform plane source. This plane source consists of the projections of the visible portion of the interior shield wall, the innerbody, and the source disk. As shown in Figure 28, each visible surface is divided into a number of small area elements which are bounded by elliptical arcs. This latter condition arises from the fact that on each surface the apparent emittance is calculated at the centers of a finite number of circular ring elements; these then appear as elliptical elements, or fractions thereof, in the projection. Each elliptical area element thus can be weighted by the apparent emittance calculated for the center of the parent circular element. The weighted area elements are then summed for all the surfaces visible at the given aspect angle ϕ to give the radiant intensity $J(\phi)$ in that direction.

A mathematical statement of the foregoing procedure takes the following form:

$$J(\phi) = \sum_{j=1}^n A_{1j}(\phi, x_j) W(x_j) + \sum_{k=1}^m A_{2k}(\phi, r_k) W_2(r_k) + \sum_{l=1}^p A_{3l}(\phi, \gamma_l) W_3(\gamma_l) \quad (13)$$

In Eq. (13), the ΔA terms represent the elliptical area elements described above on the projection plane at aspect angle ϕ , where

$A_{1j}(\phi, x_j)$ = area element relating to the circular ring element centered about x_j on the shield wall.

$A_{2k}(\phi, r_k)$ = area element relating to the annular ring centered about radius r_k on the source disk.

$A_{3l}(\phi, \gamma_l)$ = area element relating to the spherical ring centered about the polar angle γ_l on the spherical innerbody.

The W terms are the corresponding apparent emittance values. The sum involving either the source disk or the innerbody disappears when either is completely obscured from view. The analysis establishing the three ΔA terms as a function of angle ϕ is a straightforward application of

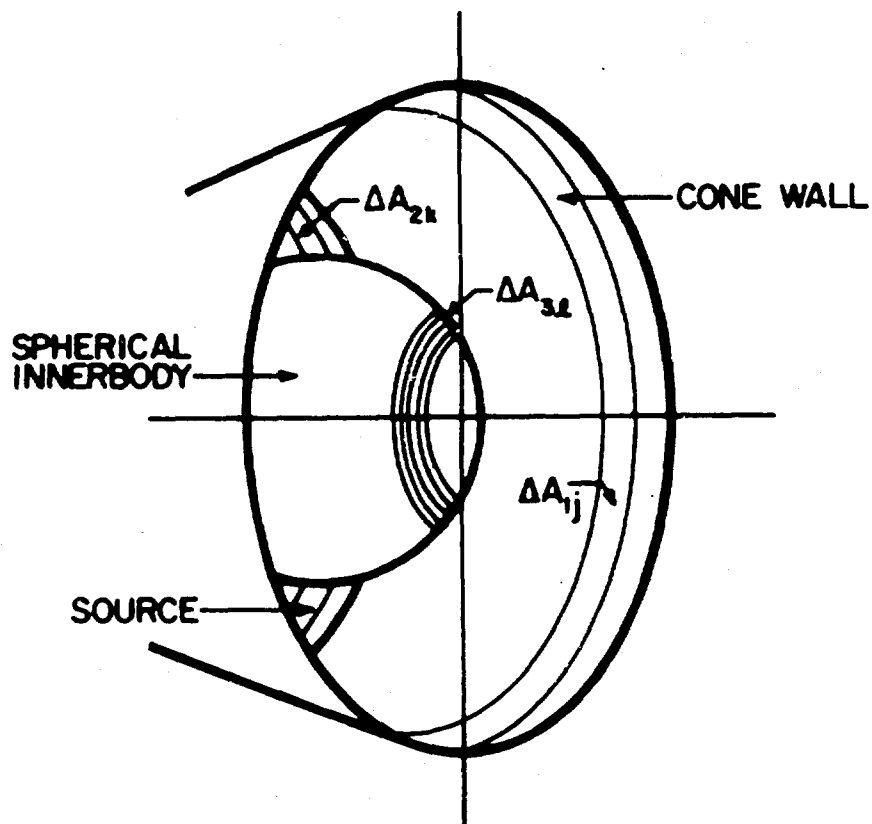


Figure 2. Interior Surface Elements of Conical Enclosure with Spherical Innerbody.

analytic geometry; these derivations are omitted from the report. Equation (13) was programmed in the functional forms of the ΔA terms for machine computation of $J(\phi)$.

As previously mentioned, a second prediction method can be formulated for the diffuse shield-source enclosure when the apparent emittance distribution functions are known in closed form. Such is the case for the cylinder. The approximate analytical solution obtained by Moon (Reference 12) for the diffuse cylinder is of the following form:

$$W_1(x) = B \cosh kx + C \sinh kx \quad (14)$$

$$W_2(r') = \text{constant}$$

For the experimental conditions considered herein, Moon's solution reduces to a single exponential term given by

$$W_1(x) = B e^{-kx} \quad (15)$$

$$W_2(r') = \text{constant}$$

The details of deriving the prediction formulas making use of Eq. (15) are given in Appendix C. As shown there, two prediction formulas are required, depending on whether the source disk is, or is not, seen at a given aspect angle. These two formulas are given by Eqs. (51) and (52), Appendix C.

Formulation for Specular Shield

Because of the mirror-like surface elements, many aspects of the specular shield are brought within the realm of geometrical optics. The prediction formulation becomes essentially a ray-tracing problem of varying difficulty, depending on the geometry of the shield. The prediction formulation for specular shields will be limited herein to the cylinder closed at one end by a diffuse disk source. In principle, this formulation can be extended to the cone and other geometries.

It is necessary first to determine the kernels for transfer of specular radiation. The kernel for specular interchange between elementary rings on the cylinder is given by Eq. (8) of Reference 13. The kernel for specular interchange from an elementary annulus to an elementary ring element on the cylinder can be derived by the method of Reference 13, and the result

is given in Appendix B. Each of these specular kernels contains a convergent infinite series which represents the infinite number of reflections possible between two area elements. Next, the two simultaneous integral equations follow from Eq. (8) by eliminating consideration of the innerbody. Introducing the specular kernels and initial trial solution into the integral equations and applying the iteration process yields ultimately the composite energy/unit area leaving from each ring element into all directions.

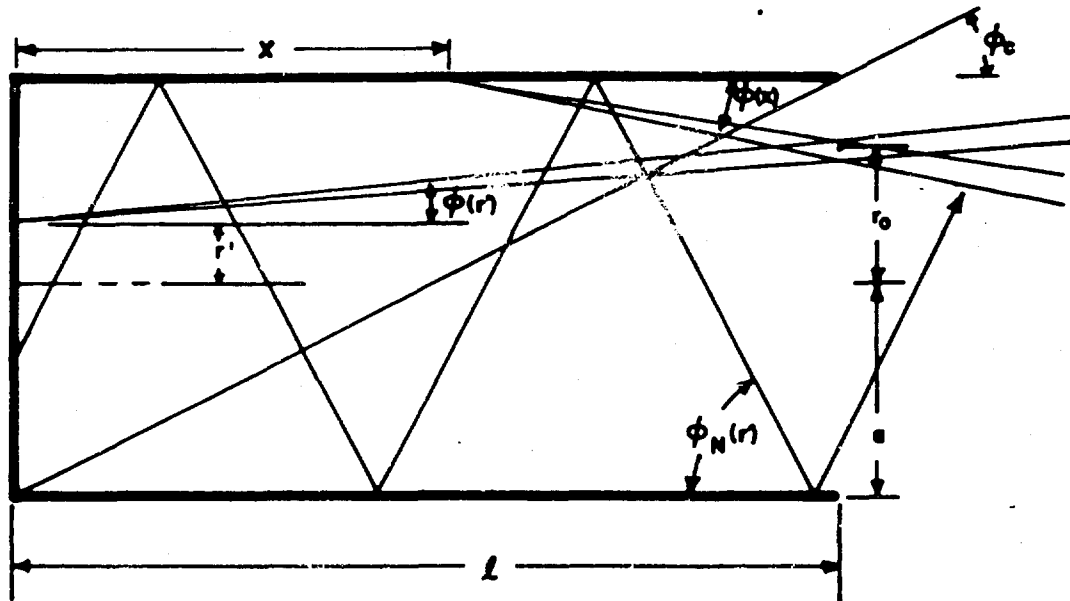


Figure 29. Geometry of Specular Cylinder.

It is now possible to develop a prediction technique by considering the radiative transfer from each ring element to the open end of the cylinder. As an example, consider a ring at x on the cylinder in Figure 29. Radiant energy from the ring can pass through the open end either directly or indirectly by reflection. The open end can be regarded as a disk which is itself divided into annular zones or rings. Each annular zone in turn can be thought of as defining a small solid angle into which the entire cylindrical ring transfers directly a fraction of its total energy. From Figure 29, the direction $\phi(x)$ of this small solid angle with respect to the axis of the cylinder is given by

$$\phi(x) = \arctan\left(\frac{a - r_0}{l - x}\right),$$

whereas that for the annular ring on the source disk is given by

$$\phi(r) = \arctan\left(\frac{|r_0 - r'|}{l}\right).$$

All that remains to determine the directly transmitted radiation is to specify the fraction of the total energy at each band transferred through each zone of the open end. It turns out that the kernels for ring-to-ring interchange multiplied by the width of the appropriate annulus or ring are the required fractional values, or exchange factors.

It is possible to derive an exchange factor for radiation reaching the open end via n reflections (Reference 13). The angle of incidence at the first reflection, and also its complement ϕ_n , is preserved at all n reflections because of the cylindrical symmetry; the angle ϕ_n is the aspect angle of the n -times reflected ray with respect to the axis of the cylinder.

From the ring element at x , for example, both the energy transferred through the open end and the aspect angle ϕ_n can be computed for once-reflected rays, for twice-reflected rays, for N th and so on up to M th-reflected rays. The number M is specified by the criterion that the $(M + 1)$ th-reflected ray transfers negligible energy through the open end. Similar calculations can be made for all ring elements at which the apparent emittance has been previously calculated; the aspect angles $\phi_n(x)$ and $\phi_n(r')$ and the corresponding emergent radiant intensities are computed and compiled for all ring elements. From the total collection of these computations, the angles $\phi_n(x)$ and $\phi_n(r')$ are sorted according to whether they fall within a neighborhood $\Delta\phi$ of a specified aspect angle ϕ . The radiant intensities corresponding to the emergent directions ϕ_n falling within $\phi \pm \Delta\phi$ are summed to give the radiant intensity of the reflected energy in the direction ϕ .

A similar sorting technique can be applied to the directly transmitted energy. The prediction formulation for the specular cylinder is completed by now adding the direct and the reflected components in the direction ϕ .

COMPARISON OF PREDICTED DIRECTIONAL INTENSITIES

The results of calculations based on the prediction formulations developed in the preceding section are now presented and compared. The computational results are presented in graphical form in Figures 30 - 43. Consideration of the basic shield configuration leads to four logical groupings which are keyed to tables in the text. The corresponding table specifies all the other shield parameters for each curve of the basic group, while the parameter being varied is listed on the graph. Curves not in these groups are specified within the figure. A direct comparison with laboratory measurement is possible for a set of parameters for each basic shield configuration.

Description of the experimental work is given in the interim report relating to this study (Reference 18). The emittance of the unshielded source based on the experimental work is .30 watts/cm²; this value was assigned to the parameter W_{02} in all calculations. The source reflectivity ρ_2 was not varied either, being fixed at .30. Since the shield models were maintained at room temperature, a direct measurement of the wall emittance W_{01} was not possible with the experimental arrangement described in Reference 18. Therefore, an extrapolated value of 10^{-4} watts/cm² was taken as the experimental value of W_{01} for all configurations. The reflectivity of the experimental diffuse shield models was .02. The parameters W_{01} and ρ_1 , for given values, were assumed to be uniform over the shield surface. Attention is now turned to comparison of directional intensity patterns and the effects of shield parameters.

EFFECTS OF SHIELD PARAMETERS

Diffuse Cylinder

Consider first the diffuse cylinder. Directional radiant intensity $J(\theta)$ patterns are plotted for different combination of parameters in Figures 30, 31 and 32. Figure 30 shows the dependence of $J(\theta)$ on the reflectivity of the cylinder, while Figure 31 shows the dependence on the emittance of the cylinder. Figure 32 gives the directional patterns for variation in the cylinder length, and also compares the experimental curve with the predicted pattern for the laboratory conditions. The differences between these two particular curves will be discussed below along the similar curves for the other configurations. It is noted from Figure 30 that the pattern increases with increasing reflectivity, especially for the larger values of θ . Since the wall emittance is held fixed, this effect must be due entirely to interreflected radiation when the source is not visible, which occurs for this particular cylinder when θ is greater than 27.11° . A distinct bend in curves 2 and 3 starts approximately at this angle, indicating clearly the increase due to interreflection over the

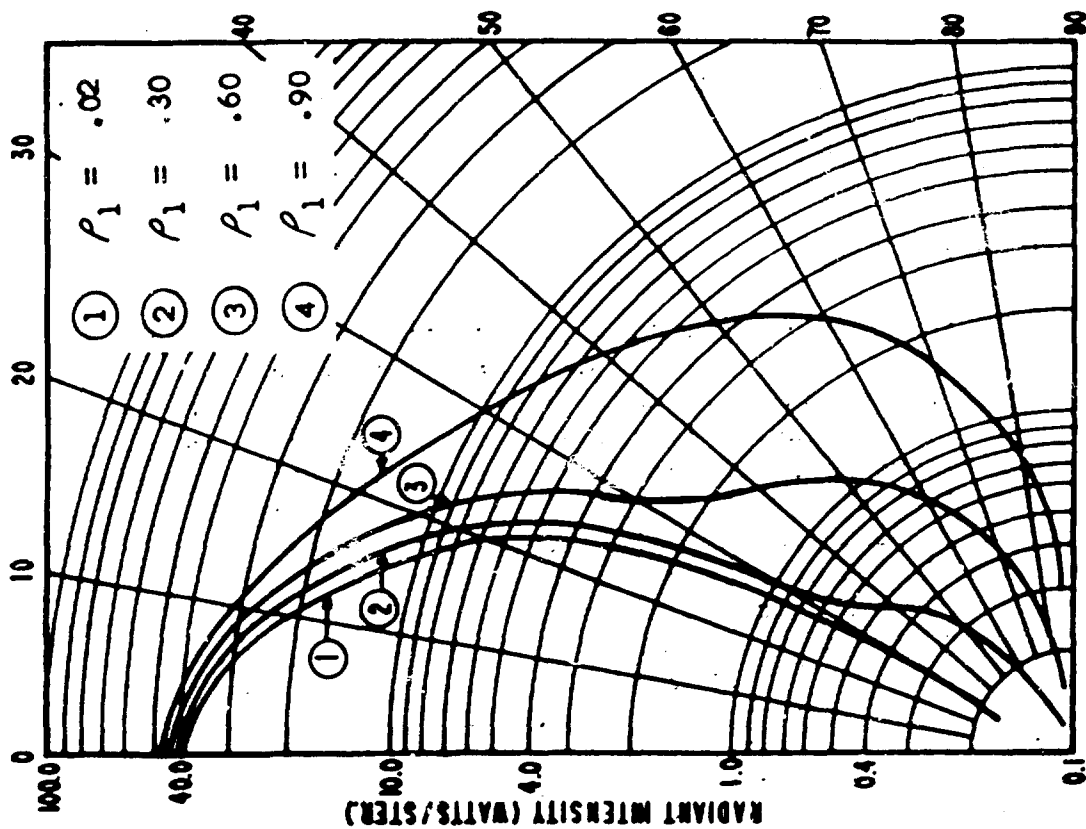


Figure 30. Directional Intensity of Diffuse Cylinders (See Table 5).

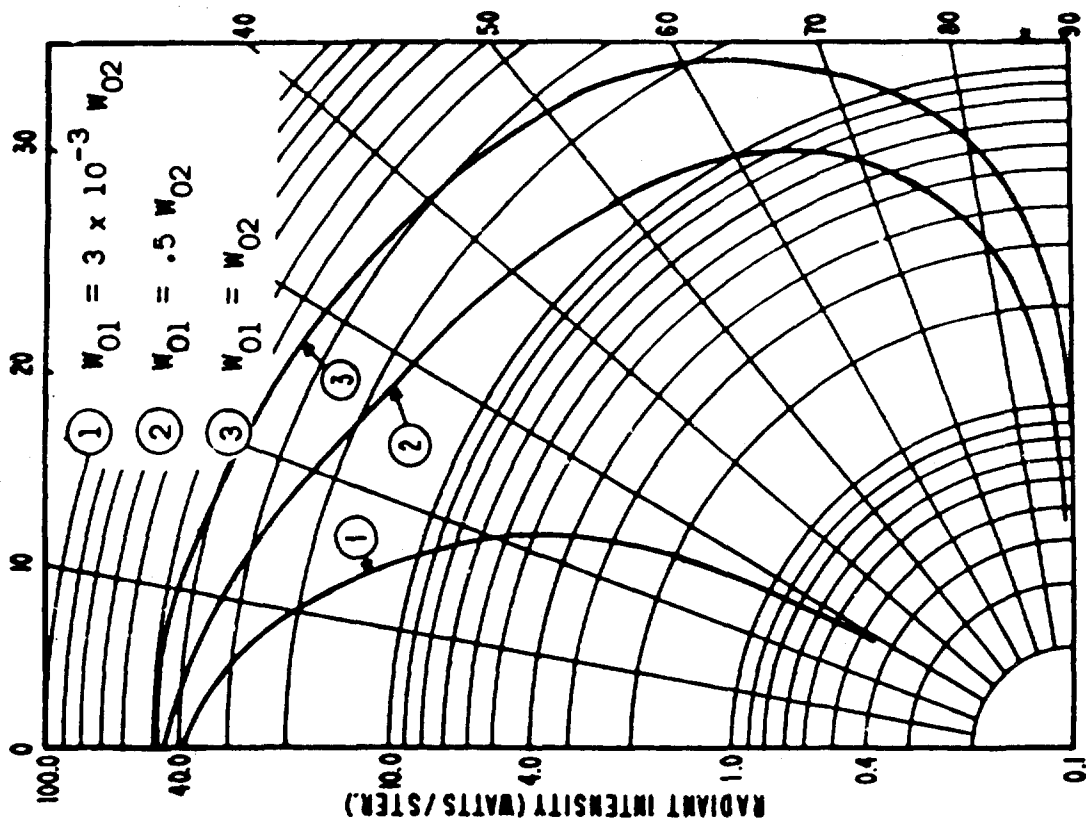


Figure 31. Directional Intensity of Diffuse Cylinders (See Table 5).

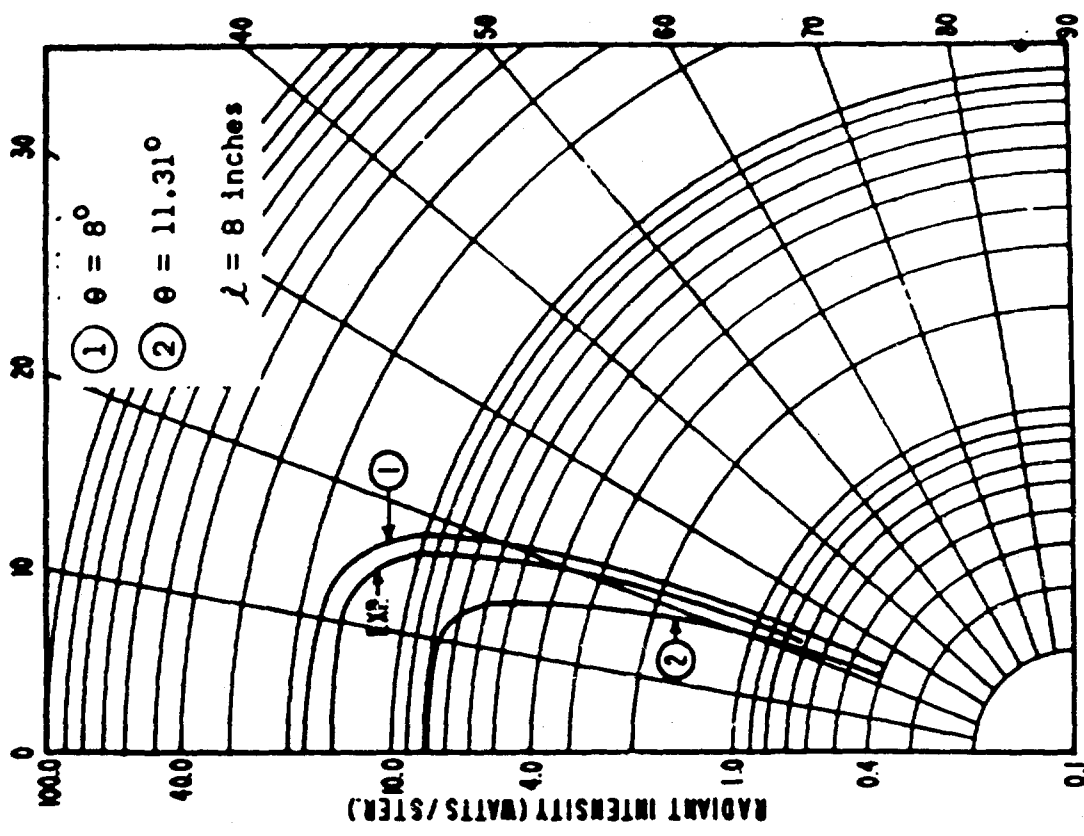


Figure 32. Directional Intensity of Diffuse Cylinders (See Table 5).

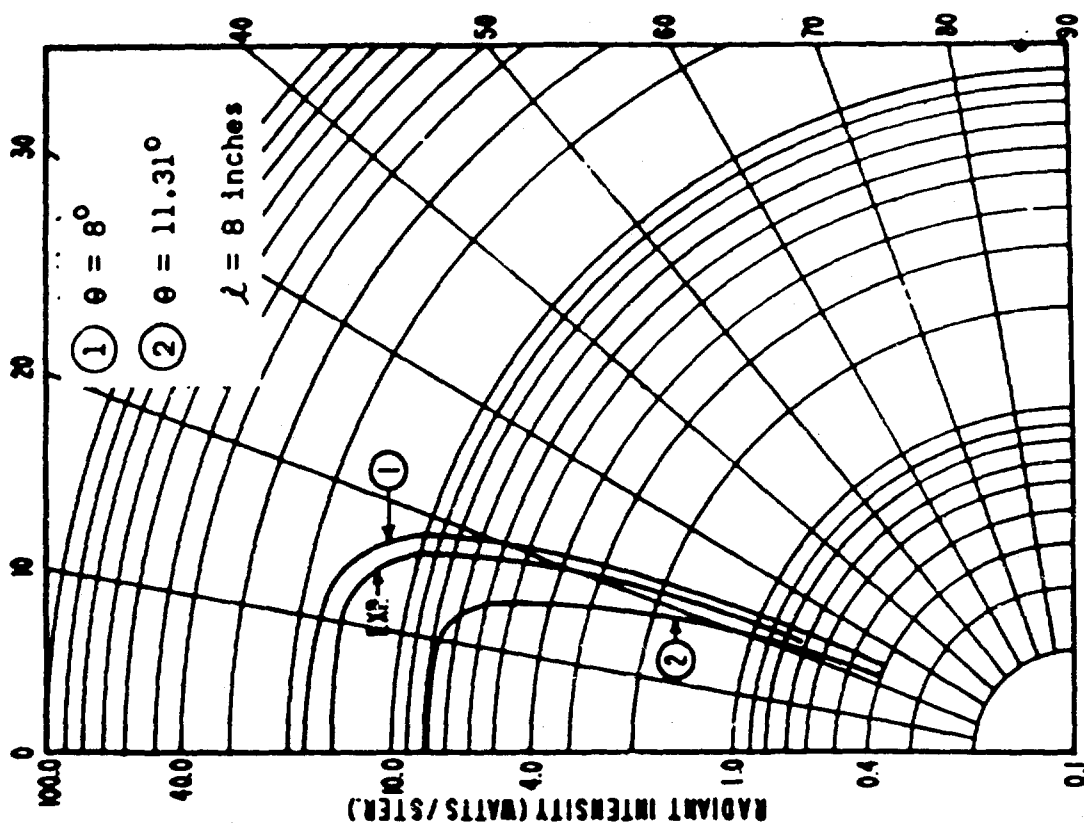


Figure 33. Directional Intensity of Diffuse Small Cones (See Table 6).

directly emitted energy. This increase can be taken approximately as the difference from curve 1, which in the normal direction is about a 35% increase for curve 4. The curves of Figure 31 show the expected result that as the cylindrical cavity approaches the isothermal condition the directional intensity pattern tends toward a cosine distribution. Figure 32 clearly shows that decreasing the cylinder length decreases its shielding effect.

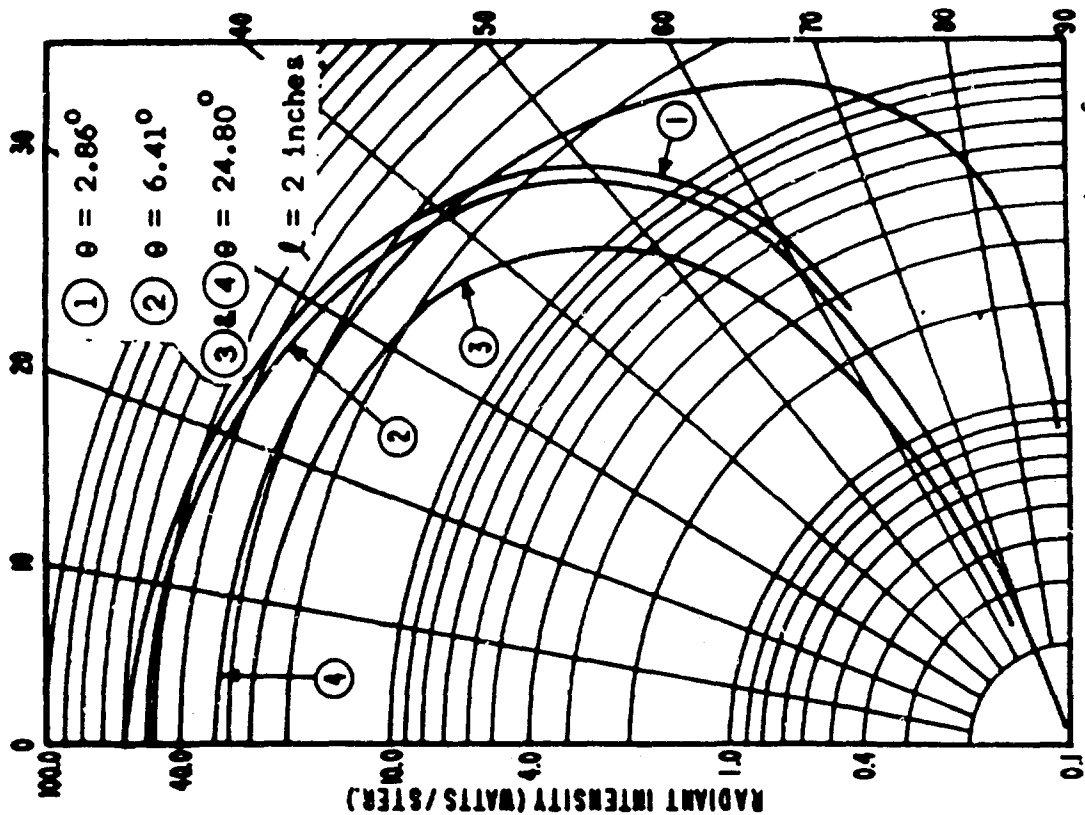
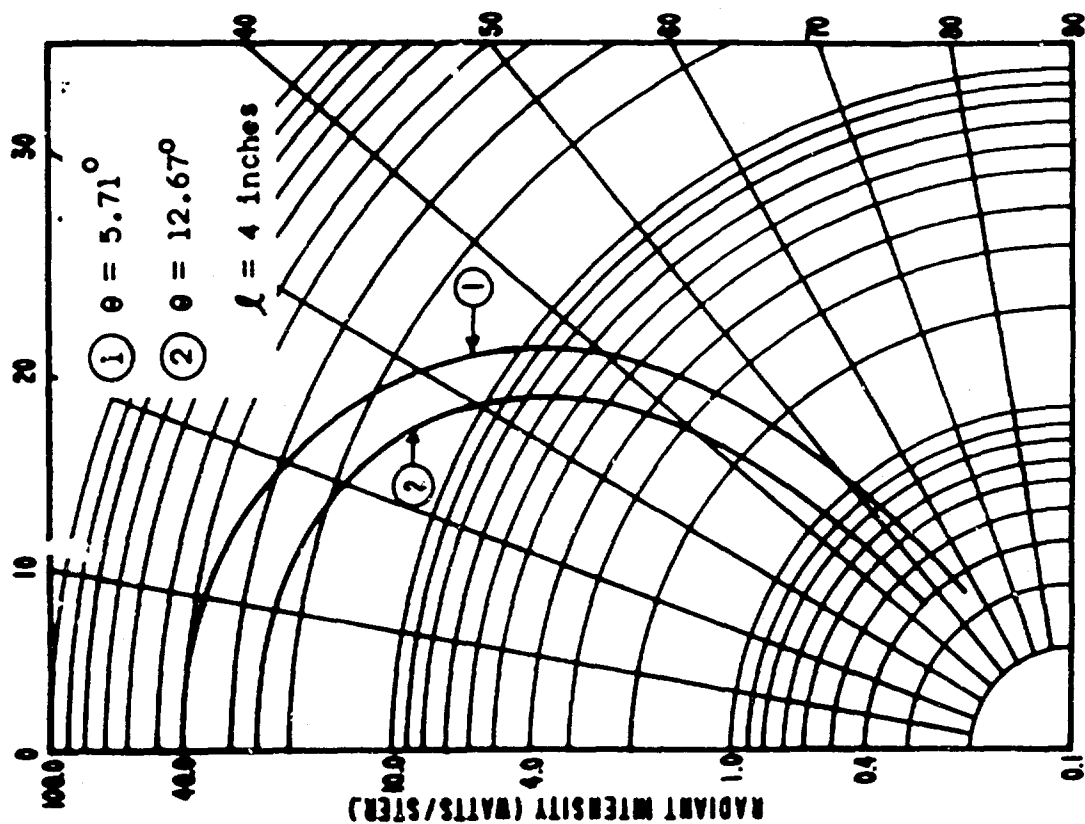
TABLE 5
DIFFUSE CYLINDER PARAMETERS

| Fig. No. | Curve No. | Length (in.) | Radius (in.) | Cyl. Refl. ρ_1 | W_{01} Watts/cm ² |
|----------|-----------|--------------|--------------|---------------------|--------------------------------|
| 30 | 1 | 7.8125 | 2 | .02 | .1 x 10 ⁻³ |
| - | 2 | 7.8125 | 2 | .30 | .1 x 10 ⁻³ |
| - | 3 | 7.8125 | 2 | .60 | .1 x 10 ⁻³ |
| - | 4 | 7.8125 | 2 | .90 | .1 x 10 ⁻³ |
| 31 | 1 | 7.8125 | 2 | .02 | .1 x 10 ⁻³ |
| - | 2 | 7.8125 | 2 | .02 | .15 |
| - | 3 | 7.8125 | 2 | .02 | .30 |
| 32 | 1 | 8.0 | 2 | .02 | .1 x 10 ⁻³ |
| - | 2 | 4.0 | 2 | .02 | .1 x 10 ⁻³ |
| - | 3 | 2.0 | 2 | .02 | .1 x 10 ⁻³ |
| - | exp.* | 7.8125 | 2 | .02 | .1 x 10 ⁻³ |

* Represents experimentally determined curve.

Diffuse Small Cone

By the term "small cone" is meant the truncated cone with its wider base forming the source area. The curves pertaining to this configuration are presented by Figures 33, 34, and 35. The experimental curve for the laboratory small cone is compared with the corresponding predicted pattern in Figure 33. A comparison between curves 1 and 2 of Figure 33 shows the effect of changing the cone angle for the same axial length. The directional patterns here demonstrate rather abrupt decreases in radiant intensity. This sharp change is noted for the experimental curve also. These curves follow very closely the cosine law just short of the decrease. Considering curve 2, Figure 34 ($\theta = 12.67^\circ$) and curve 2, Figure 33 ($\theta = 11.31^\circ$) shows for approximately the same cone angle but



half the axial length that the cutoff is not nearly as sharp. This is to be expected since the open radius of the small cone increases by decreasing the axial length for a given cone angle. This effect is amplified in Figure 35, which compares several cone angles for an axial length of two inches. The isothermal case, represented by curve 4, Figure 35, results in very nearly a cosine distribution, indicating little shielding effect.

TABLE 6
DIFFUSE SMALL CONE PARAMETERS

| Fig. No. | Curve No. | Axial Length (in.) | Base Rad. (in.) | Open Rad. (in.) | Cone Ang. (deg.) | Cone Refl. ρ_1 | W_{01} (watts/cm. ²) |
|----------|-----------|--------------------|-----------------|-----------------|------------------|---------------------|------------------------------------|
| 33 | 1 | 8 | 2.5 | 1.375 | .8° | .02 | .1 x 10 ⁻³ |
| - | exp.* | 8 | 2.5 | 1.375 | .8° | .02 | .1 x 10 ⁻³ |
| - | 2 | 8 | 2.5 | .90 | 11.31° | .02 | .1 x 10 ⁻³ |
| 34 | 1 | 4 | 2.5 | 2.10 | 5.71° | .02 | .1 x 10 ⁻³ |
| - | 2 | 4 | 2.5 | 1.60 | 12.67° | .02 | .1 x 10 ⁻³ |
| 35 | 1 | 2 | 2.5 | 2.40 | 2.86° | .02 | .1 x 10 ⁻³ |
| - | 2 | 2 | 2.5 | 2.28 | 6.41° | .02 | .1 x 10 ⁻³ |
| - | 3 | 2 | 2.5 | 1.58 | 24.8 ° | .30 | .3 x 10 ⁻³ |

* Represents experimentally determined curve.

Diffuse Large Cone

The term "large cone" means the truncated cone with the smaller end at the source, as shown by Figure 44. The effects of varying the shield parameters of this configuration are represented by Figures 36 through 40. In Figure 36 are plotted the directional intensities as a function of reflectivity for a cone angle of 39.29°. These curves exhibit a sharp cutoff similar to the small cone, though occurring at larger aspect angles. The distribution up to the cutoff angle remains almost a cosine distribution, as was observed experimentally. Here, as in the cylinder, the effects of interreflected radiation show up markedly past the cutoff at which the source is no longer visible. Figure 37 shows two curves applying to the same cone angle of 68°, approximately, but for lengths of two and four inches. The curves coincide almost over the entire quadrant and fall in the proximity of the cosine distribution. Figure 38 demonstrates the

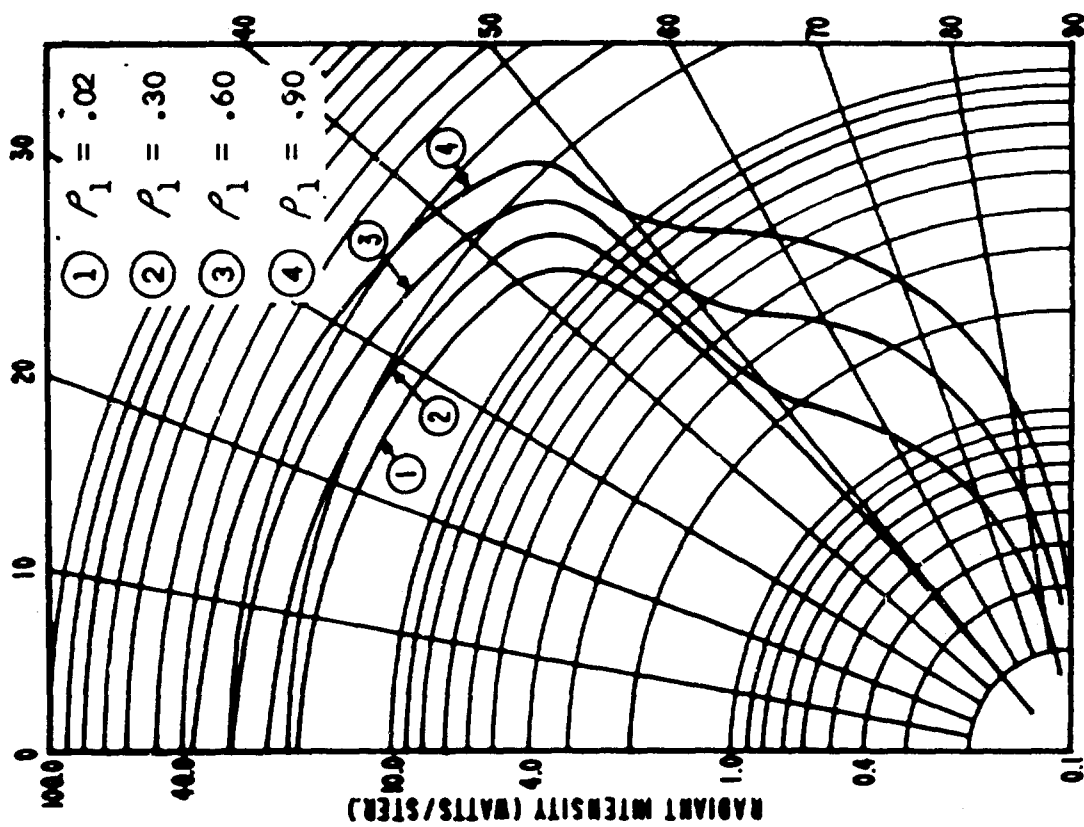


Figure 36. Directional Intensities of Diffuse Large Cones (See Table 7).

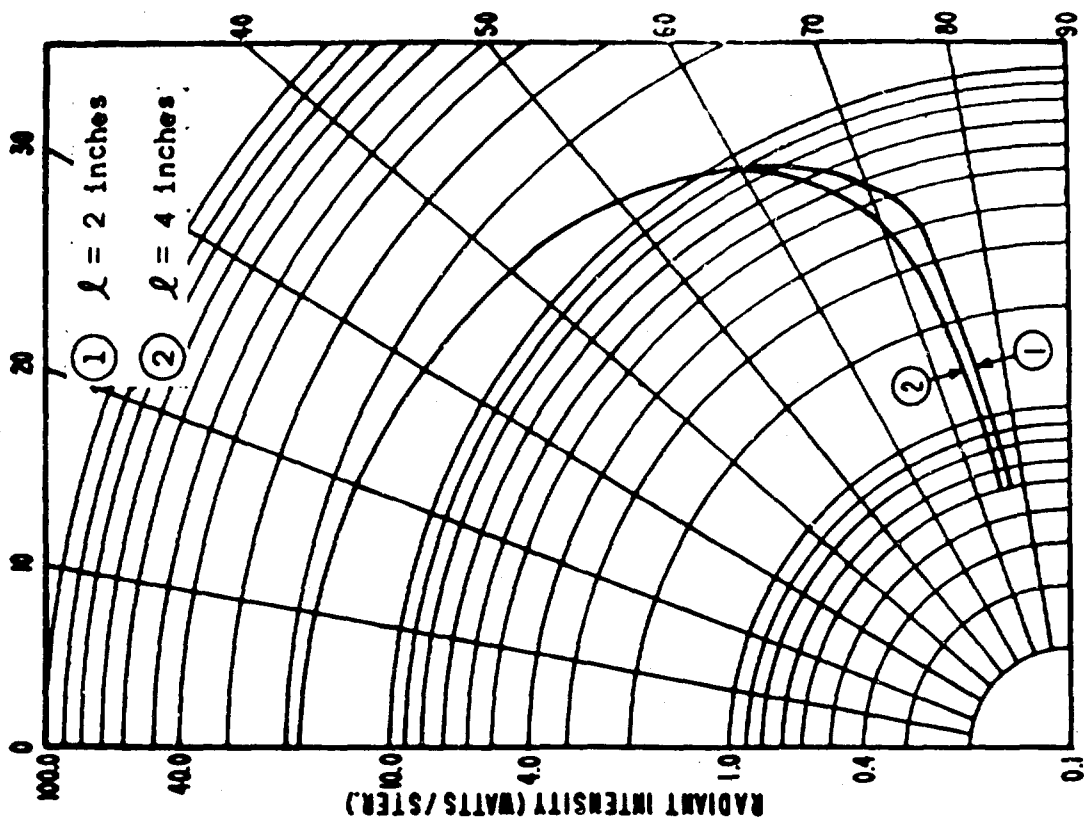


Figure 37. Directional Intensities of Diffuse Large Cones (See Table 7).

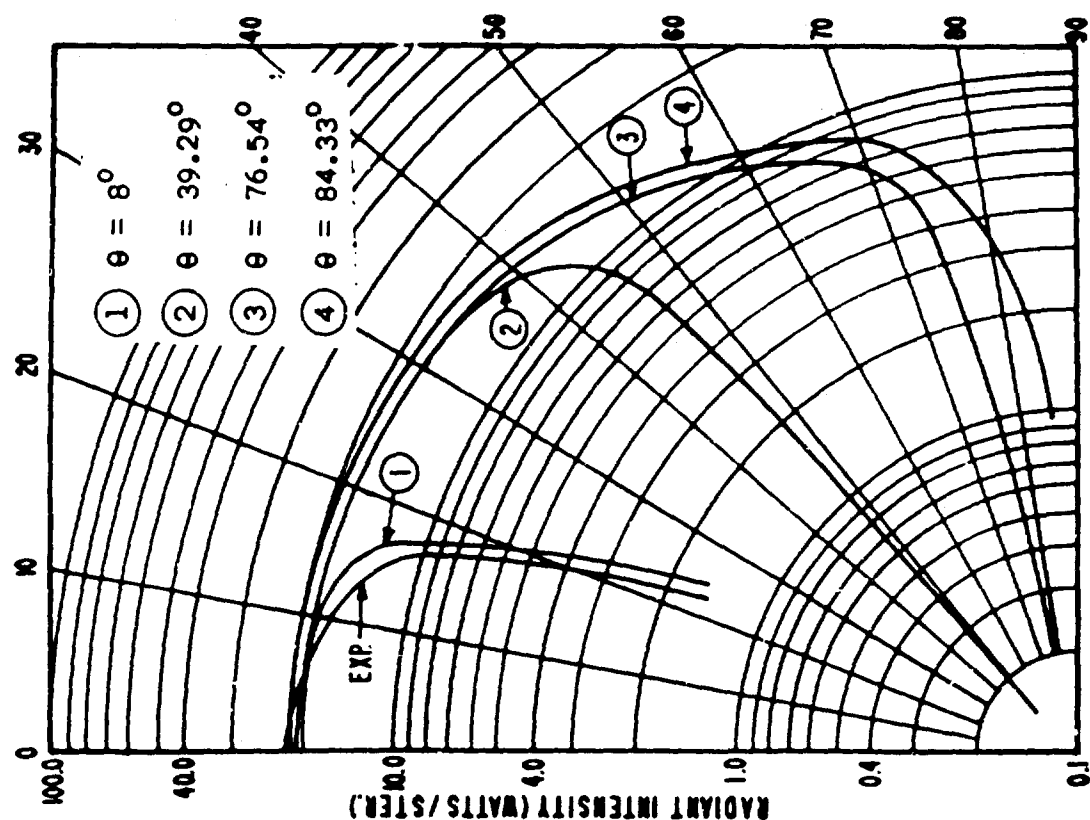


Figure 38. Directional Intensities of Diffuse Large Cones (See Table 7).

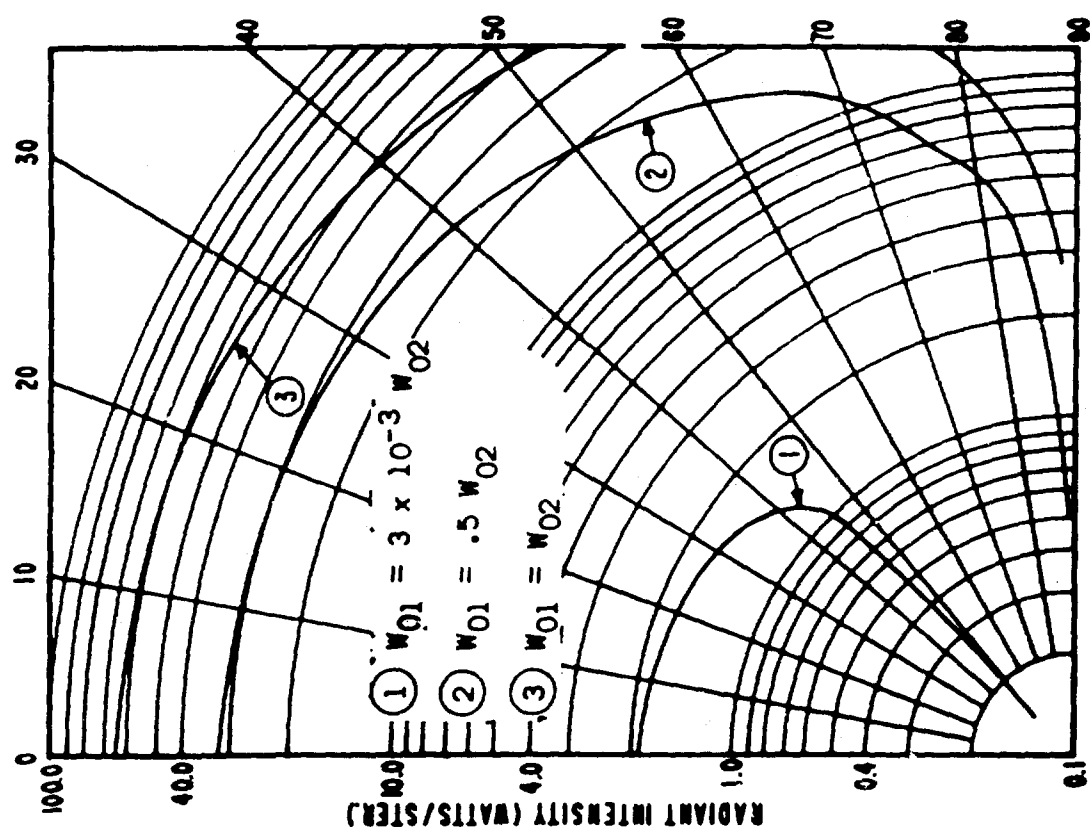


Table 39. Directional Intensities of Diffuse Large Cones (See Table 7).

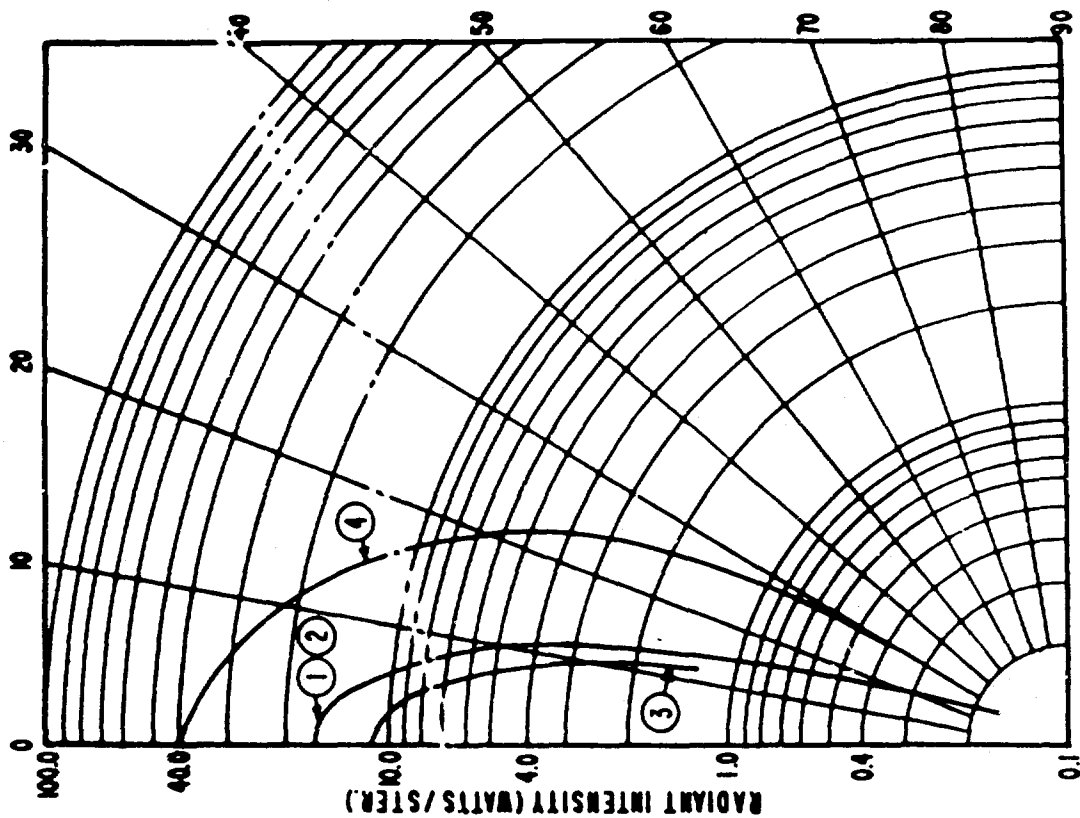


Figure 41. Directional Intensity of Diffuse Cylinder with Innerbody. (See Table 8).

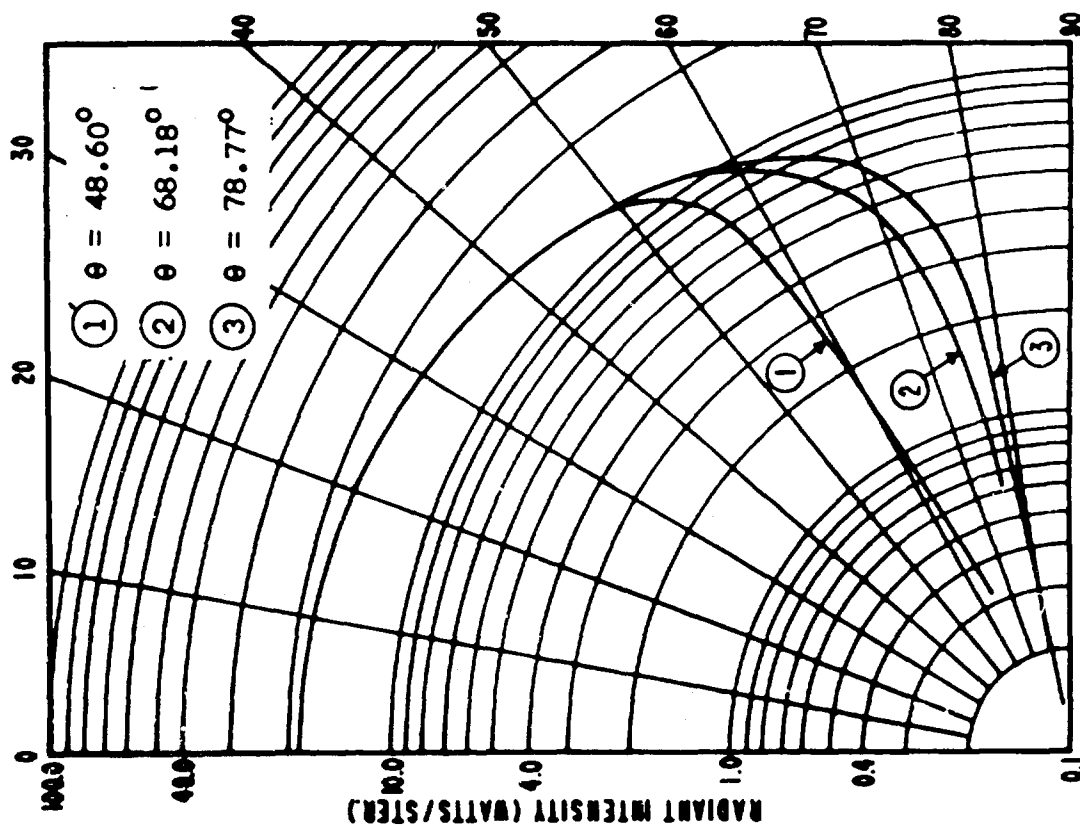


Figure 40. Directional Intensities of Diffuse Large Cones (See Table 8).

variation caused by changing the cone emittance W_{01} . Figure 39 shows the effect of changing the cone angle. It seems from these curves that the most effective shield is obtained with small cone angles, approaching the cylinder. The predicted curve shows the same general shape as the experimental curve. Figure 40 shows the dependence of the directional intensity also on the cone angle but for half the axial length used in Figure 39. For this length, four inches, the patterns coincide until the cutoff for the smallest cone angle is reached. Up to that point, the shielding effect for all three cones is practically the same, being at the same time almost negligible.

TABLE 7
DIFFUSE LARGE CONE PARAMETERS

| Fig. No. | Curve No. | Axial Length (in.) | Base Rad. (in.) | Open Rad. (in.) | Cone Ang. (deg.) | Cone Refl. ρ_1 | W_{01} (watts/cm. ²) |
|----------|-----------|--------------------|-----------------|-----------------|------------------|---------------------|------------------------------------|
| 36 | 1 | 8 | 1.375 | 7.919 | 39.29° | .02 | .1 x 10 ⁻³ |
| - | 2 | 8 | 1.375 | 7.919 | 39.29° | .30 | .1 x 10 ⁻³ |
| - | 3 | 8 | 1.375 | 7.919 | 39.29° | .60 | .1 x 10 ⁻³ |
| - | 4 | 8 | 1.375 | 7.919 | 39.29° | .90 | .1 x 10 ⁻³ |
| 37 | 1 | 2 | 1.375 | 11.367 | 68.35° | .02 | .1 x 10 ⁻³ |
| - | 2 | 4 | 1.375 | 9.992 | 68.18° | .02 | .1 x 10 ⁻³ |
| 38 | 1 | 8 | 1.375 | 7.919 | 39.29° | .02 | .1 x 10 ⁻³ |
| - | 2 | 8 | 1.375 | 7.919 | 39.29° | .02 | .15 |
| - | 3 | 8 | 1.375 | 7.919 | 39.29° | .02 | .30 |
| 39 | exp.* | 8 | 1.375 | 2.5 | 8° | .02 | .1 x 10 ⁻³ |
| - | 1 | 8 | 1.375 | 2.5 | 8° | .02 | .1 x 10 ⁻³ |
| - | 2 | 8 | 1.375 | 7.919 | 39.29° | .02 | .1 x 10 ⁻³ |
| - | 3 | 8 | 1.375 | 34.8 | 76.54° | .02 | .1 x 10 ⁻³ |
| - | 4 | 8 | 1.375 | 81.9 | 84.33° | .02 | .1 x 10 ⁻³ |
| 40 | 1 | 4 | 1.375 | 5.919 | 48.66° | .02 | .1 x 10 ⁻³ |
| - | 2 | 4 | 1.375 | 9.992 | 68.18° | .02 | .1 x 10 ⁻³ |
| - | 3 | 4 | 1.375 | 21.52 | 78.77° | .02 | .1 x 10 ⁻³ |

* Represents experimentally determined curves.

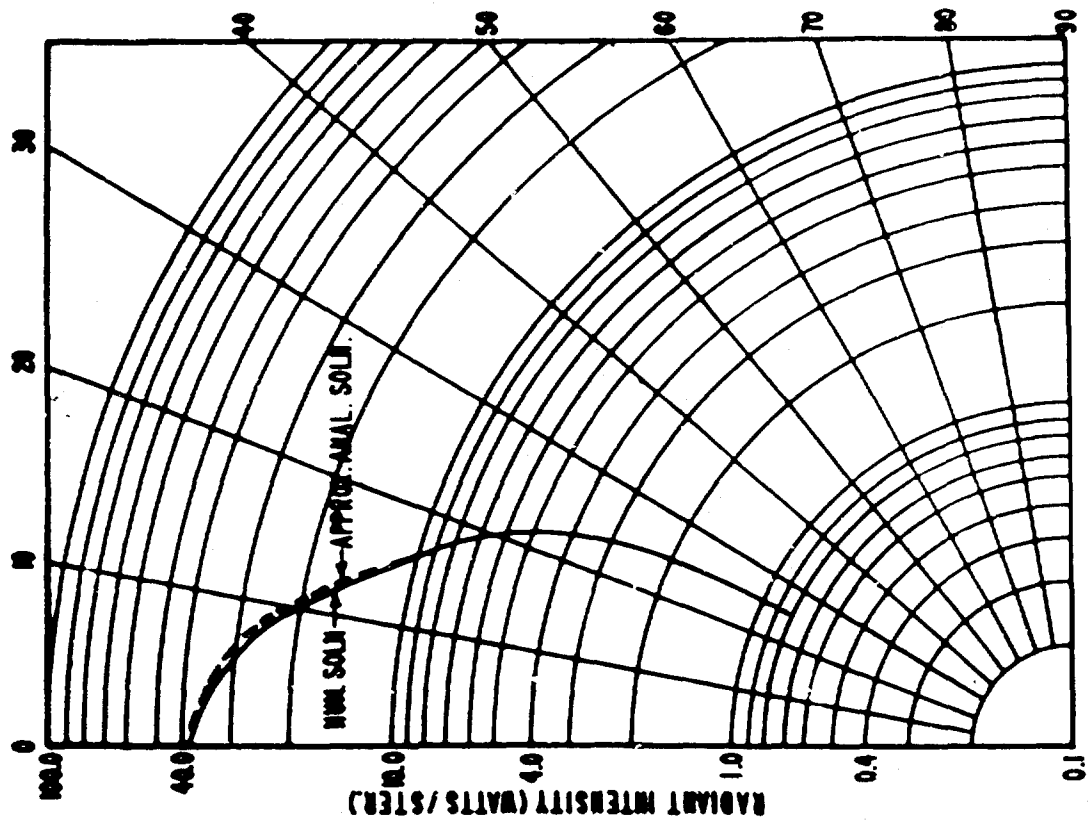


Figure 42. Directional Intensity of Diffuse Double Cone.

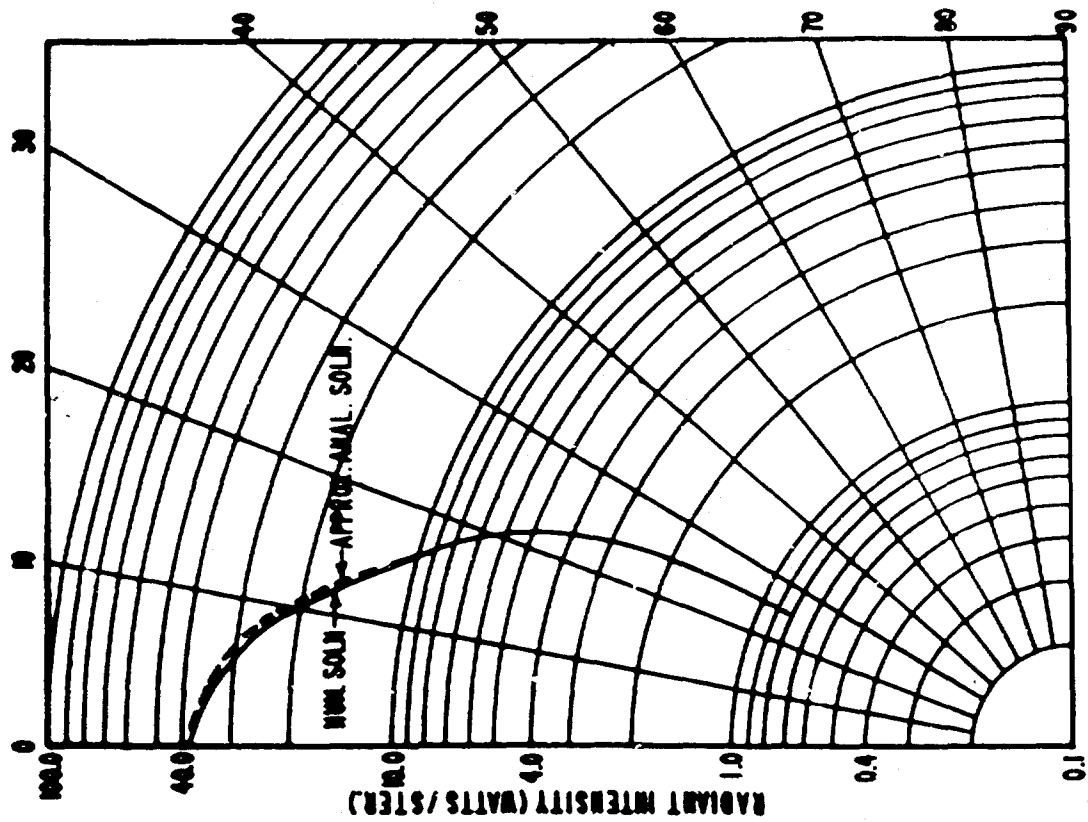


Figure 43. Comparison of Approximate Analytic and Numerical Prediction for Diffuse Cylinder.

TABLE 8
DIFFUSE CYLINDER WITH DIFFUSE SPHERICAL
INNERBODY (FIGURE 41)

| Curve No. | Cyl. Length (in.) | Cyl. Rad. (in.) | Sph. Rad. R (in.) | Cyl. Refl. ρ_c | Sph. Refl. ρ_s | Pos. of Ib | W(Cyl. & Sph.) Watts/cm. ² |
|-----------|-------------------|-----------------|-------------------|---------------------|---------------------|------------|---------------------------------------|
| 1 | 7.8125 | 2 | 1.5 | .02 | .02 | $l/2$ | $.1 \times 10^{-3}$ |
| 2 | 7.8125 | 2 | 1.5 | .02 | .02 | $l-R$ | $.1 \times 10^{-3}$ |
| exp.* | 7.8125 | 2 | 1.5 | .02 | .02 | $l-R$ | $.1 \times 10^{-3}$ |
| 3** | 7.8125 | 2 | - | .02 | - | - | $.1 \times 10^{-3}$ |

* Denotes experimental curve
** No innerbody

Diffuse Cylinder with Diffuse Spherical Innerbody

The last family of related curves is shown by Figure 41. Curves 1 and 2 here depict the same cylinder and sphere but with different positions of the innerbody. For the particular values of reflectivities used here for the spherical and cylindrical surfaces, both being .02, the axial location of the innerbody has no apparent effect on the shape of the pattern since they coincide.

Both axial positions give the same shielding effect when compared with the same cylinder without an innerbody. The effectiveness of the innerbody is readily apparent in Figure 41.

An isolated case is the diffuse double cone, whose experimental and predicted patterns are shown in Figure 42.

EXPERIMENTAL VS. PREDICTED RESULTS

The discrepancies between the experimental and predicted patterns seem to accrue to the experimental curves. This can be checked at $\theta = 0$ by calculating the normal radiant intensity for a given shield aperture. Unaccounted-for atmospheric attenuation effects probably contribute the major portion of the differences. Curves which support the prediction formulation for diffuse shields are shown in Figure 43. The patterns predicted by the numerical integral equation formulation agree well with the approximate analytic closed form developed in Appendix C.

On the basis of the curves discussed above, the cylindrical shield offers the optimum shielding effect for a wider range of aspect angles and for higher values of reflectivity.

BIBLIOGRAPHY

1. Moon, P., The Scientific Basis of Illuminating Engineering, Dover Publications, Inc., New York, N. Y., 1961.
2. Sparrow, E. M., Usiskin, C. M., Hubbard, H. A., "Radiation Heat Transfer in a Spherical Enclosure Containing a Participating, Heat-Generating Gas", Journal of Heat Transfer, Trans., ASME, Ser. C., Vol. 83, May 1961, pp. 199, 206.
3. Hamilton, D. C., Morgan, W. R., "Radiant-Interchange Configuration Factors", NACA TN 2836, 1952.
4. Blanton, R. W., Jr., and Picha, K. G., "Thermal Radiation Exchange Factors from Non-Lambertian Surfaces", Journal of Heat Transfer, Trans. ASME, Ser. C, Vol. 89, May 1962, pp. 271, 272.
5. Jakob, M., Heat Transfer, Vol. II, John Wiley & Sons, Inc., New York, N. Y., 1957.
6. Sparrow, E. M., "A New and Simpler Formulation for Radiative Angle Factors", Journal of Heat Transfer, Trans. ASME, Ser. C, Vol. 85, May 1963, pp. 81, 88.
7. Sparrow, E. M., Albers, L. U., Eckert, E. R. G., "Thermal Radiation Characteristics of Cylindrical Enclosures", Journal of Heat Transfer, Trans. ASME, Ser. C, Vol. 84, 1962, pp. 73, 81.
8. Sparrow, E. M., Jonsson, V. K., "Radiant Emission Characteristics of Diffuse Conical Cavities", Journal of Opt. Soc. Am., Vol. 53, July 1963, pp. 816, 821.
9. Moon, P., "On Interreflections", Journal Opt. Soc. Am., Vol. 30, 1940, pp. 195, 205.
10. Lovitt, L. V., Linear Integral Equations, First Edition, Dover Publications, Inc., New York, N. Y., 1950.
11. Buckley, H., "On the Radiation From the Inside of a Circular Cylinder," Phil. Mag., Vol. 17, 1934, p. 576.
12. Moon, P., "Interreflections in Finite Cylinders, " Vol.#31, Journal Opt. Soc. Am., 1941, pp. 223, 233.
13. Perlmutter, M., Siegel, R., "Effect of Specularly Reflecting Gray Surface on Thermal Radiation Through a Tube and From its Heated Wall," Journal of Heat Transfer, Trans. ASME, Ser. C, Vol. 85, Feb. 1963, pp. 55, 62.

14. Sparrow, E. M., Eckert, E. R. G., Jonsson, V. K., "An Enclosure Theory for Radiative Exchange Between Specularly and Diffusely Reflecting Surfaces," Journal of Heat Transfer, Trans. ASME, Ser. C, Vol. 84, Nov. 1962, pp. 294, 300.
15. Gouffe, A., "Corrections d'Ouverture des Corp-Noirs Artificiels Compte Tenu des Diffusions Multiples Internes", Rev. Opt., Vol. 24, Jan. 1945, p. 1.
16. Vollmer, J., "Study of the Effective Emittance of Cylindrical Cavities", J. Opt. Soc. Am., Vol. 47, 1957, pp. 926, 932.
17. Maxwell, E. A., Coordinate Geometry with Vectors and Tensors, Oxford University Press, London, 1958, Chap. V.
18. Hayes International Corporation, Eng. Report No. 649, "A Study of the Radiative Characteristics of Shielded Infrared Sources, Interim Report", Contract DA 44-177-TC-805, TRECOM Technical Report 63-45, Oct. 1963.

APPENDIX A

OBSCURATION WITHIN A CONICAL SHIELD

WITH SPHERICAL INNERBODY

Figure 44 shows the type of shield configuration under consideration, namely, a truncated right circular cone with a spherical innerbody located on the axis. For explicitness, a viewing point is taken on the cone at point x , and the obscuration from this point is shown by the shaded portions of the enclosure. Attention will be directed to the partially obscured ring elements on each surface. The coordinates used to specify these elementary ring areas are also shown in Figure 44. (The dimensions of the shield are shown in Figure 46). Because of the axial symmetry, the viewing points are chosen to lie in the x - z plane, allowing the extent of obscuration for each ring to be expressed by a single parameter. This parameter is the z -coordinate of the point of intersection between the ring element and boundary of the obscured zone. Such points will be symbolized by z_{ij} , denoting the obscuration of the j th surface as seen from the i th.

The use of the z_{ij} points will be illustrated by an example. Consider the partially obscured conical ring at ξ in Figure 45, which shows the cross section through the cone at ξ parallel to the y - z plane. It is seen from Figure 45 that the azimuthal angle β_{11} is given by

$$\beta_{11}(x, \xi) = \pi - \arccos[z_{11}(x, \xi) / \delta(\xi)] , \quad z_{11}(x, \xi) < 0 \quad (16)$$

$$= \arccos[z_{11}(x, \xi) / \delta(\xi)] , \quad z_{11}(x, \xi) > 0.$$

For the conical ring at ξ , the ratio of the unobscured periphery to the total is given by

$$\tau(x, \xi) = \beta_{11}(x, \xi) / \pi . \quad (17)$$

The function $\tau(x, \xi)$ very easily serves the ultimate purpose of this analysis, since multiplying the kernel for the unobscured ring by $\tau(x, \xi)$ gives the kernel when the ring is partially obscured. A similar function, $\tau(x, \rho)$, serves the same purpose for the partially obscured annular ring on the end disk.

However, a slightly different approach is used when the sphere is viewed or when the viewing point is on the sphere. It is necessary, in these

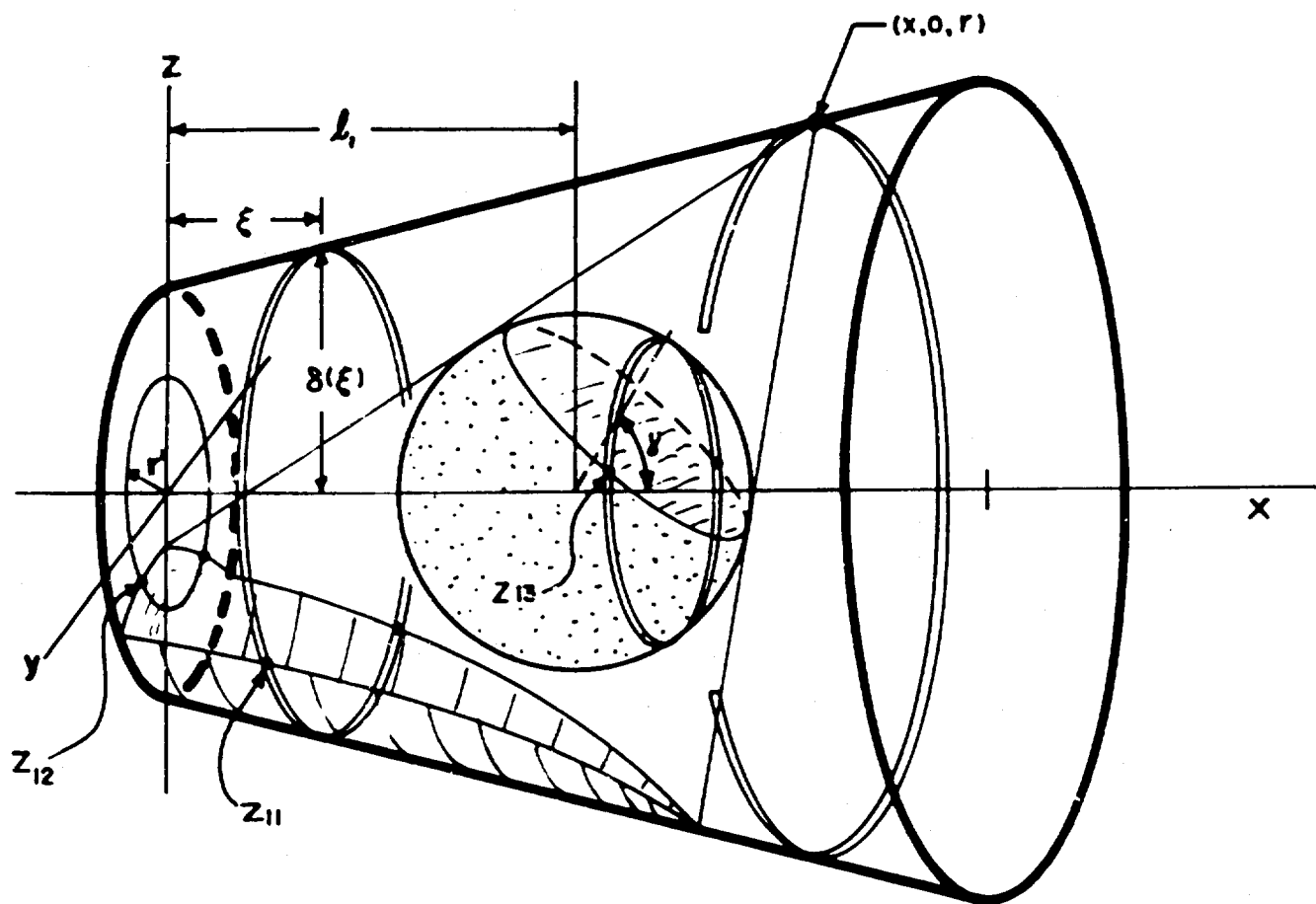


Figure 44. Conical Shield With Spherical Innerbody

cases, to put Eq. (16) to the form

$$\begin{aligned}\beta_{ij} &= \pi - \arccos(z_{ij}/r_j), \quad z_{ij} < 0 \\ &= \arccos(z_{ij}/r_j), \quad z_{ij} > 0\end{aligned}\tag{18}$$

where r_j represents the appropriate radius of the elementary ring being viewed.

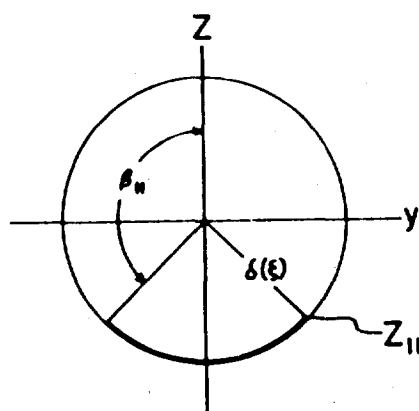


Figure 45. Obscuration of Conical Ring.

For example, when viewing the sphere from the conical ring at x , the values of $z_{13}(x, r)$ and $r_3 = R \sin \gamma$ are substituted into Eq. (18) to specify an azimuthal angle β_{13} . The angle β_{13} is in turn applied directly in the kernel equation for radiant interchange between the partially obscured spherical ring and the viewing point. (See Appendix B.) A similar approach is followed when the sphere is viewed from the source disk.

Thus the crux of the obscuration problem is to derive analytic expressions for the points z_{ij} as seen from viewing points on each surface. Strictly within the framework of analytic geometry, the analysis is straightforward but lengthy; only the main features of the approach and the results will be given below.

Viewing Point on Cone

(1) View of Cone - For partially obscured conical rings, the analysis centers around the imaginary cone which has its apex at the viewing point at x and is tangent to the spherical innerbody of radius R . Because this tangent cone is thus circular, it is possible to obtain z_1 in terms of the intersection of the familiar conic sections and the circle of radius δ . According to Reference 17, the equation of the tangent cone from the point $(x, 0, r)$ (see Figure 44) is given by

$$\left[(x - l_1)^2 + r^2 - R^2 \right] \left[(x - l_1)^2 + y^2 + z^2 \right] = \left[(x - l_1)(\xi - l_1) + rz - R^2 \right]^2 \quad (19)$$

Equation (19) can be manipulated to yield the conic section which is obtained when a plane parallel to the y - z plane is passed through any point in the obscured region of the cone. The result is given in the standard form for the conic section; i.e.,

$$\frac{y^2}{b^2} + \frac{(z - h)^2}{a^2} = 1 \quad (20)$$

where

$$a = \frac{R|x - \xi| \left[(x - l_1)^2 + r^2 - R^2 \right]^{\frac{1}{2}}}{(x - l_1)^2 - R^2}$$

$$b^2 = \frac{R^2 (x - \xi)^2}{(x - l_1)^2 - R^2}$$

$$h = \frac{r[x\xi - l_1(x + \xi) + l_1^2 - R^2]}{(x - l_1)^2 - R^2}.$$

If the equation for the circle is written as

$$y^2 + z^2 = \delta^2, \quad (21)$$

then substituting Eq. (21) into (20) and solving for z gives the required locus of intersection,

$$z_{11}(x,) = \frac{hb^2 - |a| [b^2 (b^2 + h^2 - a^2 - \delta^2) + a^2 \delta^2]^{\frac{1}{2}}}{b^2 - a^2} \quad (22)$$

(2) View of End Disk - When obscuration of the end disk occurs, the preceding discussion for the conical ring holds intact here, except that is set equal to zero and $()$ is replaced by $()$, the radius of a partially obscured plane annulus of the end disk. The points of intersection are thus given by $z_{12}(x,)$, where now

$$a = \frac{R x (x - \ell_1)^2 + r^2 - R^2}{(x - \ell_1)^2 - R^2}$$

$$b^2 = \frac{(R x)^2}{(x - \ell_1)^2 - R^2} \quad (23)$$

$$h = \frac{r[\ell_1^2 - \ell_1 x - R^2]}{(x - \ell_1)^2 - R^2}$$

(3) View of Sphere - The obscuration of the sphere as seen from point $(x, 0, r)$ on the cone is depicted in Figure 46. The plane marking the boundary of the visible segment forms a circular base for the tangent cone, and it appears as a chord (line C) in Figure 46.

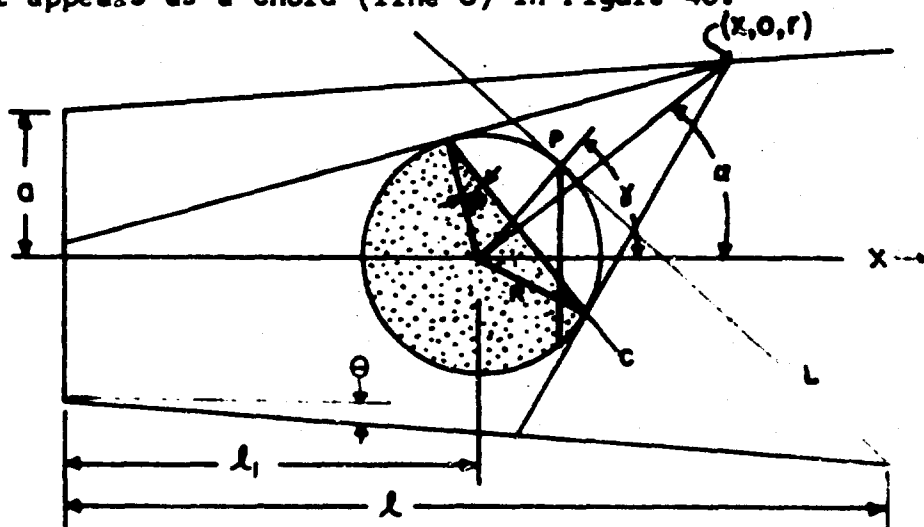


Figure 46. Obscuration of Spherical Innerbody.

The equation of line C is

$$z = R \sin(\alpha - \phi) - \frac{(x - l_1)}{r} \left[\xi - l_1 - R \cos(\alpha - \phi) \right] , \quad (24)$$

where

$$\alpha = \arctan \left(\frac{r}{x - l_1} \right)$$

$$\phi = \arctan \left(\left[(x - l_1)^2 + r^2 - R^2 \right]^{1/2} / R \right)$$

$$r = a + x \tan \theta .$$

The parameter ξ denotes the x-coordinate of any point on the line C. The desired points of intersection z_{13} are found by substituting $\xi = l_1 + R \cos \gamma$ into Eq. (24); i.e.,

$$z_{13}(x, \gamma) = (R/r) \left[R + (l_1 - x) \cos \gamma \right] . \quad (25)$$

The unobscured spherical segment lies within angular limits

$$\alpha_1 = \alpha - \phi$$

$$\alpha_2 = \alpha + \phi ,$$

where α and ϕ are defined above.

Viewing Point on End Disk

View of Cone - When the viewing point is the point $(0, 0, \rho)$ on the end disk, the roles of ρ and r are merely interchanged in Eq. (23); and setting $x = 0$ makes that equation applicable for $z_{21}(\rho, x)$.

View of Sphere - The equation for line C in this case follows from Eq. (24) by putting $x = 0$ and replacing r by ρ . Consequently, the points of intersection are given by

$$z_{23}(\rho, \gamma) = (R/\rho) [R + l_1 \cos \gamma] . \quad (26)$$

The angular limits of the unobscured segment are likewise modified.

Viewing Point on Sphere

View of Cone - When the viewing point is on the sphere, the visible portion of the enclosure lies above the plane tangent to that point. The viewing point is specified by angle γ when it lies in the x - z plane, as shown in Figure 46. There the tangent plane at point p is represented by line L, whose equation is

$$z_{31}(\gamma, x) = \frac{(l_1 - x) \cos \gamma + R}{\sin \gamma} . \quad (27)$$

Equation (27) is clearly the locus of the required intersection points.

View of End Disk - The points $z_{32}(\gamma, \rho)$ of intersection between partially obscured annuli of the end disk follow Eq. (27) by setting $x = 0$.

The foregoing analysis can be applied for the reversed cone, i.e., when the wide end is at the origin, simply by reversing the sign on the cone angle θ and for the cylinder by setting θ equal to zero.

APPENDIX B

KERNELS FOR CONICAL SHIELD CONFIGURATIONS

WITH SPHERICAL INNERBODY

Diffuse Shields - Except for the double cone, all the kernels for the diffuse shields considered in this report follow from those for the truncated cone, wide end open, with spherical innerbody. See Figures 44 and 46 for the parameters of this configuration. Therefore, in Eqs. (28) through (34), the kernels for the truncated cone, small end open, and the cylinder are obtained by replacing the cone angle θ by $-\theta$ and zero, respectively. For radiant interchange involving the sphere, the kernels were derived by integrating the fundamental equations [Eqs. (11a) or (11b)] with $D_1(\alpha_1) = D_2(\alpha_2)$. The remaining kernels were derived by algebraic techniques (angle factor algebra). These techniques are described and applied in References 3, 5, 6, 7 and 8. Hence, little is gained by including the lengthy details of the derivations here.

Accordingly, the kernels are listed for radiant energy transfer between the following elementary ring elements:

(1) Spherical Ring to Conical Ring

$$K_{31}(\gamma, x) = 2R^2 \sin \gamma \left[\frac{2(a_1 b_2 - a_2 b_1) - a_1^2 \sin \gamma}{2\pi(a_1^2 - b_1^2) \sin^2 \gamma} \left(\frac{\sin \beta_{13}}{a_1 + b_1 \sin \gamma \cos \beta_{13}} \right) - \right. \\ \left. \frac{\beta_{13}}{4\pi R \delta} + \frac{2F}{\pi} \tan^{-1} \left\{ \left[\frac{a_1 - b_1 \sin \gamma}{a_1 + b_1 \sin \gamma} \right]^{\frac{1}{2}} \tan \left(\frac{\beta_{13}}{2} \right) \right\} \right] \quad (28)$$

where

$$\delta = a + x \tan \theta$$

$$F = \frac{4R\delta(a_1 a_2 - b_1 b_2 \sin \gamma) + a_1^3 - 2a_1 b_1^2 \sin^2 \gamma}{4R(a_1^2 - b_1^2 \sin^2 \gamma)^{3/2}}$$

$$b_1 = 2R\delta$$

$$a_1 = (l_1 - x)(l_1 - x + 2R \cos \gamma) + \delta^2 + R^2$$

$$b_2 = \sin \gamma [R^2 + R \delta \sin \theta \cos \gamma + \delta^2 + (l_1 - x)(R \cos \gamma + \delta \sin \theta)]$$

$$a_2 = -\{(l_1 - x)^2 \cos \gamma \sin \theta + (l_1 - x)[R \sin \theta (1 + \cos^2 \gamma) + \delta \cos \gamma] + R(\delta + R \cos \gamma \cdot \sin \theta)\}$$

(2) Conical Ring to Spherical Ring

According to the reciprocity relation for diffuse surfaces,

$$K_{13} = \frac{\delta}{R^2 \sin \gamma} \cdot K_{31}. \quad (29)$$

(3) Spherical Ring to Annular Ring

$$K_{32}(\gamma, \rho) = \frac{2R^2 \sin \gamma}{\pi} \left[\frac{(a_3 b_4 - a_4 b_3) \sin \beta_{32}}{(a_4^2 - b_4^2)(a_4 + b_4 \cos \beta_{32})} + \frac{2(b_4 b_3 - a_4 a_3)}{(a_4^2 - b_4^2)^{3/2}} \cdot \tan^{-1} \left\{ \left[\frac{a_4 - b_4}{a_4 + b_4} \right]^{\frac{1}{2}} \tan \frac{\beta_{32}}{2} \right\} \right], \quad (30)$$

where

$$a_3 = (l_1 + R \cos \gamma)(R + l_1 \cos \gamma)$$

$$b_3 = - (l_1 + R \cos \gamma) \rho \sin \gamma$$

$$a_4 = (l_1 + R \cos \gamma)^2 + \rho^2 + R^2 \sin^2 \gamma$$

$$b_4 = -2\rho R \sin \gamma$$

(4) Annular Ring to Spherical Ring

By the reciprocity theorem,

$$K_{23} = \frac{\rho}{R^2 \sin \gamma} \cdot K_{32} \quad (31)$$

(5) Conical Ring to Conical Ring

$$K_{11}(x, \xi) = \frac{1}{2\delta} \left[1 - \frac{|x-\xi| \sec \theta \{ (x-\xi)^2 \sec^2 \theta + 6a^2 + x\xi \tan^2 \theta + a(x+\xi) \tan \theta \}}{\{ (x-\xi)^2 \sec^2 \theta + 4[a^2 + x\xi \tan^2 \theta + a(x+\xi) \tan \theta] \}^{3/2}} \right] \quad (32)$$

(6) Conical Ring to Annular Ring

$$K_{12}(x, \rho) = 2\delta \left[\frac{x\delta(x^2 + \delta^2 - \rho^2) - x^2 \tan \theta (x^2 + \delta^2 + \rho^2)}{\{ x^2(x^2 + 2\delta^2 + 2\rho^2) + (\delta^2 - \rho^2)^2 \}^{3/2}} \right] \quad (33)$$

(7) Annular Ring to Conical Ring

By reciprocity theorem,

$$K_{21} = \frac{\rho}{\delta} \cdot K_{12} \quad (34)$$

(8) Conical Ring in First Section of Double Cone to Conical Ring in Second Section - See Figure 47 for parameters of double cone. The remaining kernels for the double cone follow from the above kernels.

$$K_{11}(x_1, \xi_2) = \frac{1}{2\delta_1} \left[1 + \frac{N}{(\xi_2 - x_1)^4 + 2(\xi_2 - x_1)^2(\delta_1^2 + \delta_2^2) + (\delta_1^2 - \delta_2^2)^2} \right] \quad (35)$$

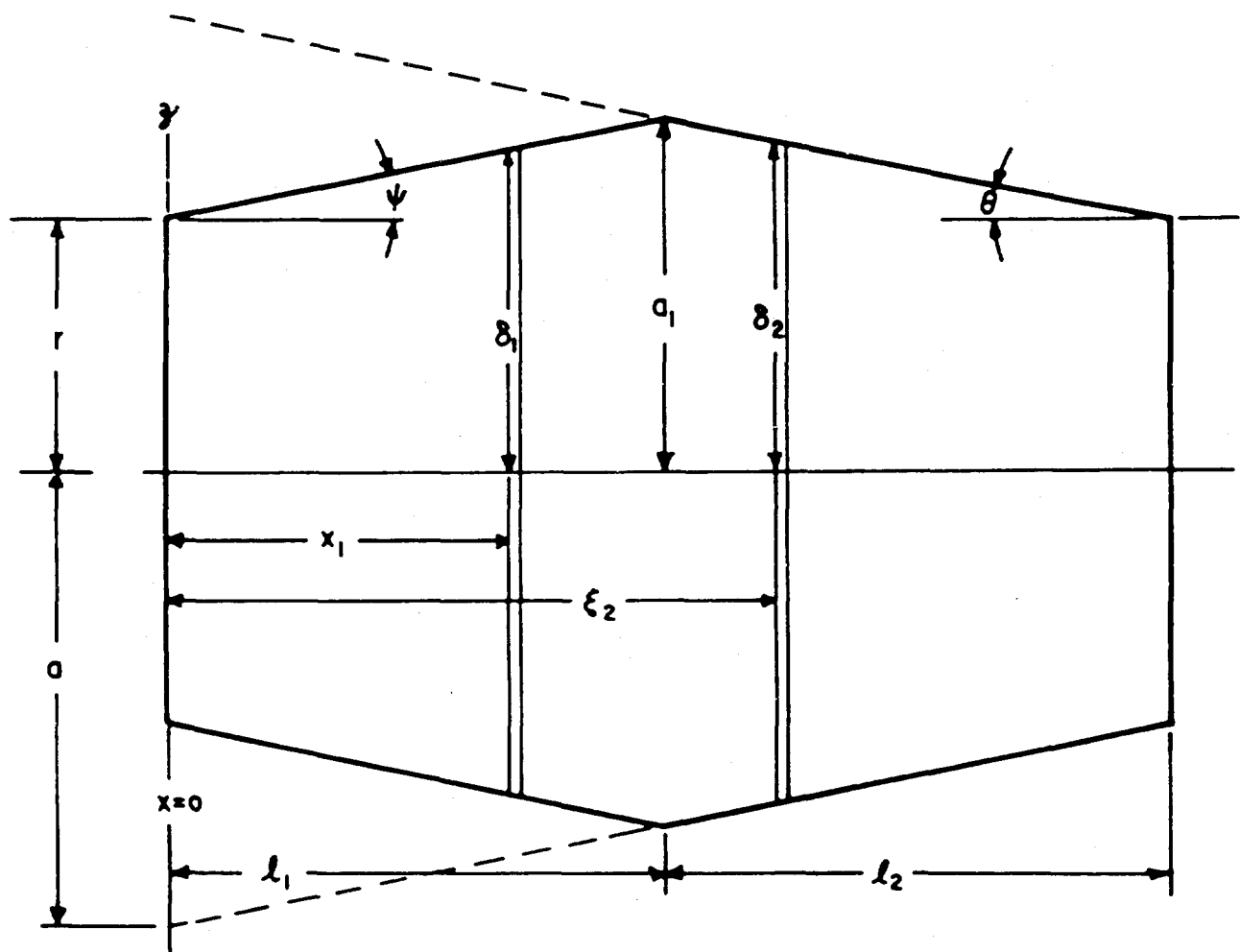


Figure 47. Geometry of Double Cone.

where

$$N = 4\delta_1\delta_2\left\{\delta_1\delta_2(\delta_1^2+\delta_2^2)+(\xi_2-x_1)\left[(\delta_1^2+\delta_2^2)(r\tan\theta+\tan\psi) - \right. \right. \\ \left. \left. 2\delta_1\delta_2(\delta_1\tan\psi+\delta_2\tan\theta)\right]+(\xi_2-x_1)^2\left[3\delta_1\delta_2 + \right. \right. \\ \left. \left. (\xi_2-x_1)(r\tan\theta+\tan\psi)\right]\right\} - [(\xi_2-x_1)^2+\delta_1^2+\delta_2^2]^3.$$

$$\delta_1 = r + x_1 \tan$$

$$\delta_2 = a - \xi_2 \tan\theta$$

(9) Conical Ring in Second Section of Double Cone to Conical Ring in First Section - By the reciprocity theorem and by replacing ξ_2 with x_2 and x_1 with ξ_1 ,

$$K_{11}(x_2, \xi_1) = \frac{\delta_1'}{\delta_2'} K_{11}(\xi_1, x_2), \quad (36)$$

where

$$\delta_1' = r + \xi_1 \tan\psi$$

$$\delta_2' = a - x_2 \tan\theta.$$

Specular Cylinder

Annular Diffuse Ring of End Disk to Specular Cylindrical Ring

$$K(r', x) = \sum_{n=0}^{\infty} \frac{\rho_1^n}{\Delta_n} K(r', x_n) \quad (37)$$

where

$$\Delta_n = \frac{(2n-1)a+r'}{a+r'} \cdot \Delta$$

$$x_n = \frac{(2n-1)a+r'}{(2n+1)a+r'} \cdot x \cdot$$

The symbol Δ represents the width of a small but finite ring element of the cylinder.

APPENDIX C

APPROXIMATE ANALYTIC FORMULATION

FOR DIRECTIONAL RADIANT INTENSITY OF A DIFFUSE CYLINDER

The approximate analytic solution given by Moon for the diffuse circular cylinder is of the form

$$\begin{aligned} W_1(x) &= B \cosh kx + C \sinh kx + D \\ W_2(r') &= \text{const.}, \end{aligned} \tag{38}$$

where $W_1(x)$ is the apparent emittance distribution as a function of length x along the cylinder wall; B , C , and D , are constant and depend on the shield parameters - length, radius reflectivity, and initial emittance W_{01} ; and $W_2(r')$ is the final emittance, including interreflections, which is assumed constant over the source disk. (The mathematical equations for B , C , D , and W_2 are somewhat lengthy, and their reproduction here would add nothing essential; see Reference 12, Eqs. (21 through (24).)

The coordinate system of the cylindrical shield is shown in Figure 29. It is easily seen from Figure 29 that source disk is not visible for aspect angles greater than $\phi_c = \arctan(2a/l)$. Figure 48 shows the interior of the cylindrical enclosure projected onto a plane perpendicular to the line of sight at angle ϕ . The rectangular coordinate system s, t lies in this plane.

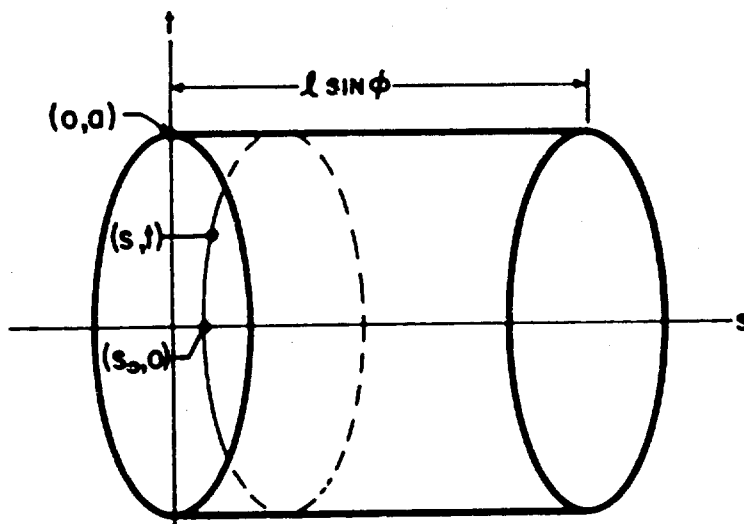


Figure 48. Projection Plane Coordinates.

Consider first the case $\phi > \phi_c$. The essence of the problem is to relate the emittance function $W_1(x)$ in the shield coordinate system to a function $L(s,t)$ in projection plane coordinates and then to integrate the function $L(s,t)$ over projected area A_p of the cylinder. In short, the radiant intensity at angle ϕ will take the form

$$J(\phi) = \iint_{A_p(\phi)} L(s,t) dA . \quad (39)$$

The function $L(s,t)$ is determined by the following argument: on the cylinder the emittance is constant around each elementary ring, which shows up as an arc of an ellipse on the projected area. Therefore, the point (s,t) can be considered to lie on an elliptical arc, the equation of the ellipse being

$$\frac{(s-h)^2}{(a \cos \phi)^2} + \frac{t^2}{a^2} = 1. \quad (40)$$

From Eq. (40) the distance h is given by

$$h(s,t) = s - a \cos \phi \left[1 - \frac{t^2}{a^2} \right]^{\frac{1}{2}} . \quad (41)$$

Since the emittance is constant along the parent circular ring, it is also constant along the corresponding elliptical arc. Hence, it is possible to relate the function $L(s,t)$ to its value at the point $(s_0, 0)$, where s_0 is the point of intersection of the elliptical arc and the s -axis. By symmetry, this point is in the horizontal diametral plane of the cylinder. From Figure 48, s_0 is equal to $h - a \cos \phi$ and, with Eq. (40), gives

$$s_0 = s - a \cos \phi \left[1 - (1 - t^2/a^2)^{\frac{1}{2}} \right]. \quad (42)$$

By defining

$$g(t) = a \cos \phi \left[1 - (1 - t^2/a^2)^{\frac{1}{2}} \right], \quad (43)$$

it is possible to set up the following functional relationship:

$$L(s,t) \Rightarrow L(s_0,0) \Rightarrow L\{s - g(t)\} . \quad (44)$$

Before Eq. (44) can be useful, a functional relationship must be established between the coordinates of the (s,t) system and the x-axis of the cylinder. From Figure 48, it is easy to establish the following correspondence.

$$L(0,0) \Rightarrow W_1 \left(l - \frac{a}{\tan \phi} \right) \quad (45a)$$

$$L(s,0) \Rightarrow W_1 \left(- \frac{s}{\sin \phi} + l - \frac{a}{\tan \phi} \right) \quad (45b)$$

$$L(s,t) \Rightarrow W_1 \left\{ - \frac{s-g(t)}{\sin \phi} + l - \frac{a}{\tan \phi} \right\} \quad (45c)$$

Through Eqs. (45c) and (43), it is possible to transform the emittance function along the x-axis of the cylinder to a distribution function along the x-axis of the projected area, and ultimately to the entire projected area.

But it is necessary yet to transform the cylindrical surface element dA into a corresponding differential projected area element $d\sigma$. In terms of the cylindrical coordinates of Figure 29, dA is given by $ad\theta dx$. From Figure 48, it is found that $dx = ds/\sin \phi$ and $ad\theta = dt/\cos \theta$; hence,

$$dA = adxd\theta = \frac{-ds dt}{\sin \phi \cos \theta} = \frac{-d\sigma}{\sin \phi \cos \theta} . \quad (46)$$

At this point it is pertinent to consider the angle α made by the line of sight and the normal to any element of area on the inner cylinder wall. For the diffuse cylinder, the radiant intensity from each differential area element in the direction of observation is given by

$$dJ(\alpha) = dJ_n(x) \cos \alpha = \frac{L(s,t)}{\pi} \frac{\cos \alpha d\sigma}{\sin \phi \cos \theta} \quad (47)$$

where $dJ_n(x)$ represents the intensity along the normal to each differential element. It was possible in the laboratory experiments to consider the lines of sight to lie in planes parallel to the diametral plane of the cylinder. Under this condition, the direction cosines of the line of sight are

$$(l_1 = \sin\phi, l_2 = 0, l_3 = -\cos\phi),$$

whereas those of the normals to the inner cylinder wall are

$$(m_1 = \cos\theta, m_2 = -\sin\theta, m_3 = 0);$$

hence, the cosine of the angle between the line of sight and the normals is

$$\cos\alpha = m_1 l_1 + m_2 l_2 + m_3 l_3 = \sin\phi \cos\theta. \quad (48)$$

Equation (48) leads to an interesting result; for when $\cos\alpha$ as expressed by Eq. (48) is substituted into Eq. (47), it is seen that the angular dependence of the radiant intensity from the entire projected area is due only to the aspect angle ϕ . With the results of Eqs. (45c), (46), (47) and (48), Eq. (39) is transformed into the following prediction formula:

$$J(\phi) = \iint_{A_p(\phi)} w_1 \left\{ -\frac{s-g(t)}{\sin\phi} + 1 - \frac{r}{\tan\phi} \right\} ds \, dt, \quad (49)$$

where it is understood that the variable x of Eq. (38) is to be replaced by the argument within the braces of Eq. (49) and that the integration is then to be taken over the projected area.

The problem generated by substituting Eq. (38) into the prediction formula is somewhat complicated; but when the cylinder is maintained at a substantially lower temperature than the source, Eq. (38) reduces to a simple exponential, i. e.,

$$w_{1(\text{lab})}(x) = Be^{-kx}. \quad (50)$$

In the form required for Eq. (49), Eq. (50) is given by

$$W_1(\text{lab})(s,t) = B \exp \left\{ -k \left[1 - (a^2 - t^2)^{\frac{1}{2}} \sec \phi - s \csc \phi \right] \right\}. \quad (51)$$

The double integration of $W_1(\text{lab})(s,t)$ is tedious but straightforward, and the details are omitted. The final result is given by the following:

$$J(\phi) = \frac{2Be^{-k\ell} \sin \phi}{k} \left[\int_0^a \exp \frac{2k(a^2 - t^2)^{\frac{1}{2}}}{\tan \phi} dt - a \right], \quad (52)$$

$$\phi > \phi_c.$$

There is no essential difference in the derivation when part of the source disk is visible; i.e., the final prediction formula for this case is

$$J(\phi) = \frac{2Be^{-k\ell} \sin \phi}{k} \left[a(pe^{k\ell} - 1) + \int_{ap}^a \exp \frac{2k(a^2 - t^2)^{\frac{1}{2}}}{\tan \phi} dt \right] + W_2 A_2(\phi), \quad (53)$$

where

$$p = \left(1 - \frac{\tan^2 \phi}{\tan^2 \phi_c} \right)^{\frac{1}{2}} \quad \text{and} \quad \phi < \phi_c.$$

DISTRIBUTION

| | |
|---|----|
| U. S. Army Materiel Command | 9 |
| U. S. Army Mobility Command | 5 |
| U. S. Army Aviation Materiel Command | 2 |
| Chief of R&D, D/A | 1 |
| U. S. Army Transportation Research Command | 39 |
| U. S. Army Research and Development Group (Europe) | 1 |
| U. S. Army Engineer Research and Development Laboratories | 3 |
| U. S. Army Limited War Laboratory | 1 |
| Army Research Office-Durham | 2 |
| U. S. Army Test and Evaluation Command | 3 |
| U. S. Army Combat Developments Command Aviation Agency | 1 |
| U. S. Army Combat Developments Command Armor Agency | 1 |
| U. S. Army Combat Developments Command Transportation Agency | 1 |
| U. S. Army War College | 1 |
| U. S. Army Command and General Staff College | 1 |
| U. S. Army Transportation School | 3 |
| U. S. Army Aviation School | 1 |
| U. S. Army Armor Board | 1 |
| U. S. Army Aviation Test Board | 1 |
| U. S. Army Airborne, Electronics and Special Warfare Board | 1 |
| U. S. Army Aviation Test Activity | 1 |
| Air Force Systems Command, Wright-Patterson AFB | 4 |
| Air University Library, Maxwell AFB | 1 |
| Bureau of Naval Weapons | 8 |
| Naval Air Test Center | 1 |
| Ames Research Center, NASA | 1 |
| NASA-LRC, Langley Station | 2 |
| Lewis Research Center, NASA | 1 |
| NASA Representative, Scientific and Technical Information Facility | 2 |
| Research Analysis Corporation | 1 |
| Defense Documentation Center | 10 |
| U. S. Patent Office | 1 |

| | |
|--|---|
| U. S. Army Standardization Group, Canada | 1 |
| Canadian Liaison Officer, | |
| U. S. Army Transportation School | 1 |
| British Army Staff, British Embassy | 1 |
| U. S. Army Standardization Group, U.K. | 1 |

Hayes International Corp., Birmingham, Ala., A STUDY OF THE RADIATIVE CHARACTERISTICS OF SHIELDED INFRARED SOURCES - C. M. Askey, N. D. Gilliam, J. L. Reid, Engineering Report No. 649, May 1964, (Contract DA 44-177-TC-805), USATRECOM Task 1D121401A14802, TRECOM Technical Report 64-25, 93 pp.

Unclassified Report
(over)

Hayes International Corp., Birmingham, Ala., A STUDY OF THE RADIATIVE CHARACTERISTICS OF SHIELDED INFRARED SOURCES - C. M. Askey, N. D. Gilliam, J. L. Reid, Engineering Report No. 649, May 1964, (Contract DA 44-177-TC-805), USATRECOM Task 1D12401A14802, TRECOM Technical Report 64-25, 93 pp.

Unclassified Report
(over)

1. Infrared Physics
2. Contract DA 44-177-TC-805

Hayes International Corp., Birmingham, Ala., A STUDY OF THE RADIATIVE CHARACTERISTICS OF SHIELDED INFRARED SOURCES - C. M. Askey, N. D. Gilliam, J. L. Reid, Engineering Report No. 649, May 1964, (Contract DA 44-177-TC-805), USATRECOM Task 1D121401A14802, TRECOM Technical Report 64-25, 93 pp.

Unclassified Report
(over)

1. Infrared Physics
2. Contract DA 44-177-TC-805

Hayes International Corp., Birmingham, Ala., A STUDY OF THE RADIATIVE CHARACTERISTICS OF SHIELDED INFRARED SOURCES - C. M. Askey, N. D. Gilliam, J. L. Reid, Engineering Report No. 649, May 1964, (Contract DA 44-177-TC-805), USATRECOM Task 1D121401A14802, TRECOM Technical Report 64-25, 93 pp.

Unclassified Report
(over)

1. Infrared Physics
2. Contract DA 44-177-TC-805

1. Infrared Physics
2. Contract DA 44-177-TC-805

This final report gives an account of work performed since the interim report. The report is divided into two parts.

Part I covers the consolidation, refinement, and increased versatility of empirical computer programs over initial efforts in the field of prediction of radiation patterns from shielded infrared sources.

Part II presents the development of an analytical approach for the evaluation of shield configurations for infrared sources. This approach employs a set of complex integral equations relating shield geometry and radiative characteristics of the source to angular distribution of radiative energy.

This final report gives an account of work performed since the interim report. The report is divided into two parts.

Part I covers the consolidation, refinement, and increased versatility of empirical computer programs over initial efforts in the field of prediction of radiation patterns from shielded infrared sources.

Part II presents the development of an analytical approach for the evaluation of shield configurations for infrared sources. This approach employs a set of complex integral equations relating shield geometry and radiative characteristics of the source to angular distribution of radiative energy.

This final report gives an account of work performed since the interim report. The report is divided into two parts.

Part I covers the consolidation, refinement, and increased versatility of empirical computer programs over initial efforts in the field of prediction of radiation patterns from shielded infrared sources.

Part II presents the development of an analytical approach for the evaluation of shield configurations for infrared sources. This approach employs a set of complex integral equations relating shield geometry and radiative characteristics of the source to angular distribution of radiative energy.

This final report gives an account of work performed since the interim report. The report is divided into two parts.

Part I covers the consolidation, refinement, and increased versatility of empirical computer programs over initial efforts in the field of prediction of radiation patterns from shielded infrared sources.

Part II presents the development of an analytical approach for the evaluation of shield configurations for infrared sources. This approach employs a set of complex integral equations relating shield geometry and radiative characteristics of the source to angular distribution of radiative energy.